Enhancing Wake Mixing in Wind Farms by Multi-Sine Signals in the Helix Approach

L.J. Huang

Master of Science Thesis

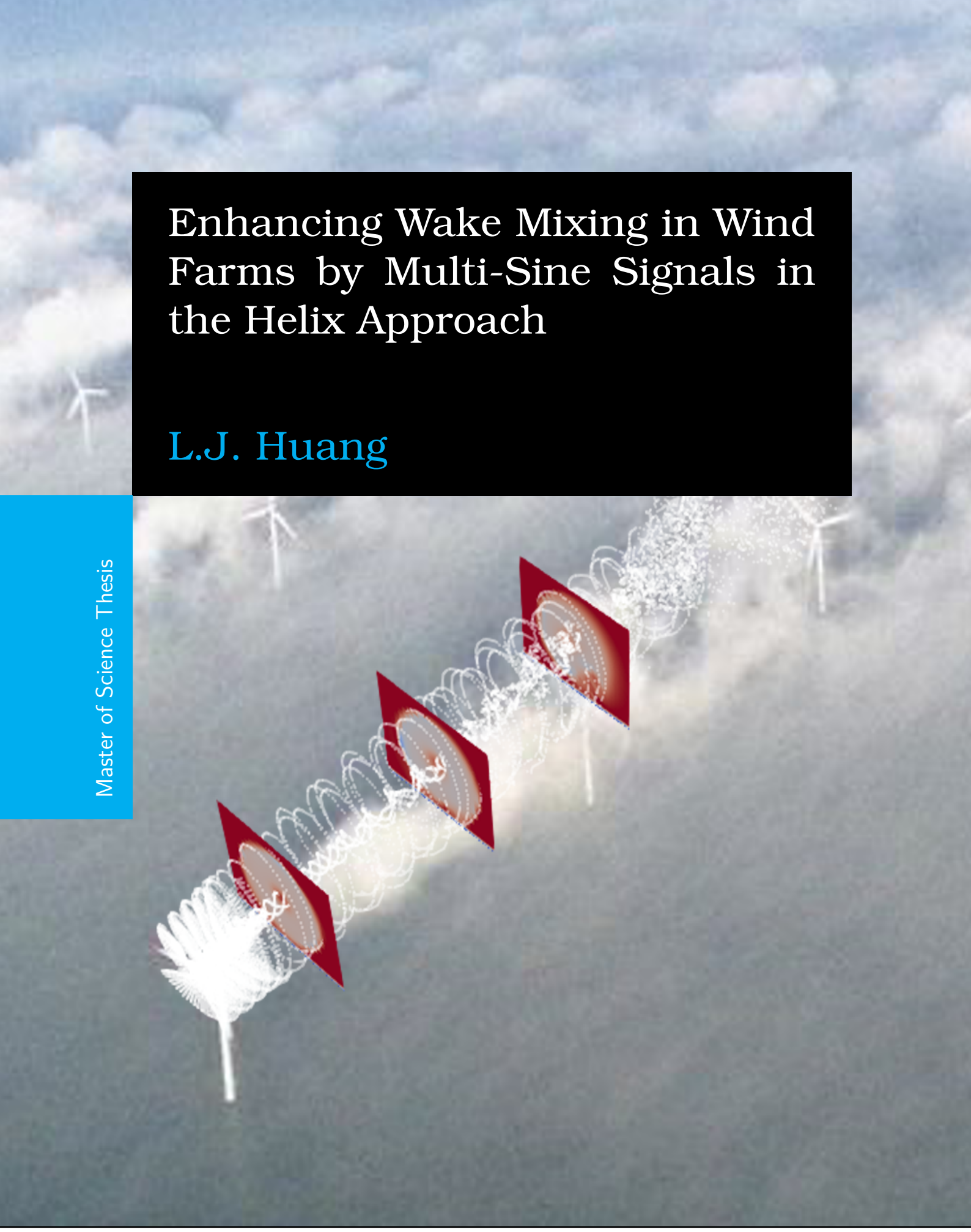

TU Delft Delft University of Technology

Delft Center for Systems and Control

Enhancing Wake Mixing in Wind Farms by Multi-Sine Signals in the Helix Approach

Master of Science Thesis

For the degree of Master of Science in Sustainable Energy Technology
at Delft University of Technology

L.J. Huang

June 24, 2022

Faculty of Mechanical, Maritime and Materials Engineering (3mE) · Delft University of Technology

Abstract

The development of offshore wind technology has progressed rapidly since the first offshore wind farm came to birth in 1991. During the last three decades, offshore wind has become an economically attractive option of renewable energy source for many countries to fulfill their commitment to combat the climate crisis. However, an open challenge remains in offshore wind, namely the aerodynamic interactions between multiple turbines, referred to as wake effects. When the upstream turbines extract energy from wind, they generate the wake with low velocity and high turbulence level on the downstream turbines, which substantially reduces the overall wind farm performance. The annual power production loss due to wake effects is generally 10 - 40%, which limits the reduction of the levelized cost of electricity for offshore wind energy.

Therefore, developing effective wind farm control strategies which could mitigate the wake effect has become an emerging research area in the past decade. Recently, a novel wind farm control strategy called the Helix approach is proposed. The Helix approach adopts the individual pitch control technique to dynamically deform the wake into the helical shape, which induces wake instability and thereby stimulates wake recovery. This control strategy has demonstrated promising potential to mitigate the wake effect and to enhance the wind farm performance. To date, the Helix approach employs single-harmonic pitch signals. However, more complex and higher-harmonic signals to potentially improve the effectiveness of the Helix approach have never been explored. Therefore, the purpose of this master thesis is to explore the potential of using multi-sine pitch profiles to further enhance the wake mixing.

The high-fidelity aeroelastic simulator OpenFAST with its recent free vortex wake code is adopted to simulate the dynamic wake evolution. A Fourrier stability analysis is used to quantitatively identify the wake breakdown position. According to the simulation results for the multi-sine pitch profiles, the wake breaks down at 1.75 D, which is earlier than the one at 2.50 D for the original single-sine Helix strategy. The earlier wake breakdown indicates the potential of faster wake recovery, which is required to be validated by the higher-fidelity model in the future studies.

Table of Contents

Acknowledgements

Foremost, I would like to express my deepest gratitude to my leading supervisor Prof. dr. ir. Jan-Willem van Wingerden. Thank you for your guidance and your generous encouragement throughout every meeting. Your high standards inspire me to always perform my best and to expand my own boundaries. When looking back to our very first meeting, I realize that I have grown so much professionally and personally. It is also of great honor and pleasure to work in your team where everyone is so talented and helpful.

Secondly, I'm also extremely grateful to the chair of committee from aerospace engineering, Dr. ir. Wim Bierbooms and Dr. ir. Axelle Viré. Thank you so much for your time on scrutinizing my work and providing your expertise on the subject.

Dr. ir. Sebastiaan Mulders, my daily supervisor, I could not have undertaken this journey without your comprehensive support from day one. You showed up in every weekly meeting giving me constructive feedbacks, you helped me with the setup of OpenFAST and OLAF, you scheduled the meeting with NREL for me, you organized the lecture room for my presentations, and you gave me specific advices on the report. You were always there whenever I got lost. For me, you are an excellent daily supervisor, no doubt. Thank you for being here the entire time in this journey.

Special thanks should absolutely go to Emanuel Taschner. Thank you for joining the weekly meetings and providing feedbacks continuously. I always made improvement in the study based on your advices. It was a great time to have discussions with you on the Fourier analysis and the large-eddy simulation. Wishing you all the best in your PhD journey.

Lastly, many thanks to my family, friends and my girlfriend, Lillian, who all mentally supported me during this two-year abroad journey. Each of you is one of the puzzles during this whole process.

Delft, University of Technology — L.J. Huang
June 24, 2022

Chapter 1

Introduction

1-1 A missing puzzle in offshore wind industry

Wind turbine technology has a long history, but deploying turbines in wind farms at offshore locations is a very recent practice. In 1991, the first offshore wind farm, Vindeby, became operational near the coast of a Danish island [1]. The wind farm consisted out of 11 turbines with a total capacity of 5MW stood still on the seabed, not only powering 2,000 Danish households, but also igniting the hope for people to combat the climate crisis. Thirty years have passed since then, and offshore wind has developed from a niche market to a mature industry, where the global installed capacity has exploded during the past three decades, from 0.03 GW in 2000, 3 GW in 2010, to 35 GW in 2020 [2].

Behind this tremendous growth, here are two strong economic factors driving the whole offshore wind industry. Firstly, more wind energy is available on the sea. Sea is a smooth area where there are less surface obstacles like those on the land, so the stronger wind allows turbines to be designed at higher rated power in an economical manner. Secondly, there is the economy of scale. Wide and empty area allows turbines to be placed together, which significantly reduces the costs of transmission as well as the costs of operations and maintenance (O&M). With these two key drivers, offshore wind has become one of the cheapest sources of electricity generation, where its levelized cost of electricity (LCoE) has dropped below the ones of coal and natural gas [1].

The current largest offshore wind farm in operation, Hornsea in the UK, is made up of 174 turbines with total capacity of 1.2 GW, which is more than 200 times larger than the first one seen thirty years ago. However, when hundreds of enormous turbines are placed together, the so-called wake effect becomes prominent, and to date remains an open challenge for making wind farms even more cost effective. After upstream turbines extract energy from wind, a wake is formed downstream with lower kinetic energy and higher turbulence level (see Figure 1-1). This low-speed wind reduces the power-production potential of downstream turbines. The overall energy loss by the wake effect depends on the site conditions and the wind

farm layout, and it is normally about 10-40% for modern wind farms [3], [4], [5]. Moreover, the high-turbulence wind induces additional fatigue loads on waked turbines, which leads to premature damages on turbine components [6], reducing the turbine lifetime and increasing LCoE. The wake effect becomes even more severe in offshore wind farms than onshore wind farms because the atmospheric turbulence is much lower on the sea than on the land, which makes the wake persist for a longer downstream distance [7].

Therefore, developing strategies to eliminate the impacts of the wake effect becomes an essential issue for the offshore wind industry. Driven by this urgent need, the research area of wind farm control has sparked the interest of academia and industry in the past decade. Wind farm control is the research domain which studies the interaction between wind turbines on a farm level and designs the strategies to ensure these turbines to work synergistically. Wind farm control is one of the grand challenges that need to be addressed to unlock the full potential in wind energy science [8]. Investigating an effective wind farm control strategy to enhance wind farm performance is the driver of this study.

Figure 1-1: The flow patterns formed by the wake effect in Horns Rev 2 offshore wind farm in Denmark. A wake with lower kinetic energy and higher turbulence level is formed behind a turbine, and overlap with a downstream turbine. The picture was captured by Henrik Krogh.

1-2 Wind farm flow control

Wind farm control can be distinguished into two main categories by its objective: electrical control and flow control. The former focuses on the control of reactive power, voltage and frequency in milliseconds or faster timescales to provide sufficient grid service, while the latter focuses on the control of flow in seconds or slower timescales to eliminate the wake effect and optimize the wind farm performance. In this study, wind farm flow control is of interest.

To the best of the author's knowledge, the concept of the wind farm flow control has been studied as early as the period when the first offshore wind farm was built. An early study by [9] already demonstrated the effectiveness of using a simple flow control strategy to enhance the wind farm performance through simulation. However, in the first two decades of the offshore wind industry, the idea of the wind farm flow control did not gain much commercial interest. Instead, most of the commercial wind farms still adopted so-called "greedy control". In the case of greedy control, the control strategy optimizes power extraction at an individual turbine level. However, downstream turbines always experience lower wind speed and higher turbulence level due to the wake effects lead by upstream turbines. Therefore, the whole wind farm does not reach its optimal performance in terms of power production and load distribution. It was not until the last decade when the size of wind farms increased tremendously and the research of the wind farm flow control aroused again. Three main control strategies have been extensively studied since then, and they are summarized/discussed in the subsequent sections: static induction control (Section 1-2-1), static wake redirection control (Section 1-2-2) and dynamic induction & wake direction control (Section 1-2-3).

1-2-1 Static induction control

The objective of induction control is to enhance the overall power production of a wind farm by purposely derating upstream turbines. This strategy is effectuated by either pitching or reducing generator torque, such that the wind deficit becomes lower in the wake since less energy is extracted. By doing so, the downstream turbines experience higher wind velocity, which results in higher power production. In other words, the upstream turbines sacrifice their performance in return for better wind resources for downstream turbines. The extent of the derating of each turbine is optimized in the way that the wind farm as a whole reaches its maximum power production.

Initial favorable simulation results of induction control were presented in the studies [10], [11], [12]. However, later studies [13], [14], [15], [16] with high-fidelity simulation and experimental results indicated that the effectiveness of induction control on power gain of the wind farm is limited to non-existing. Therefore, the research quickly shifted to another strategy: wake steering control.

1-2-2 Static wake steering control

The objective of the wake steering control is also to yield net power gain in a wind farm by deflecting the wake away from the downstream turbines. This is accomplished by inten-

tionally imposing a yaw misalignment/offset with respect to the dominant wind direction. By doing so, the downstream turbines experience higher wind speed and lower turbulence level. In a similar manner of induction control, the upstream turbines have slightly smaller power production due to the deviation from the optimal set point/condition, but downstream turbines have better performance, in which the overall power output of a wind farm increases.

The wake steering control was firstly investigated in the study [17], which suggested the possibility of using active yaw control to improve the wind farm performance. High-fidelity simulation of yaw control was later presented in the study [18], and the wind tunnel as well as full-scale experiments were also conducted, in the studies [14] [19], respectively. The promising results of these studies indicated that the static wake steering control strategy through yaw misalignment is effective in enhancing energy production in wind farm. The research in this area is still of great interest and under continuous development. A study [20] also demonstrated the possibility of using induction control combined with wake steering control. Recently, the commercial product based on wake steering control strategy has also been introduced into the market [21].

However, the aforementioned two control strategies only apply the static control settings, where the pitch and yaw angle are set at fixed values when the static optimum is reached. These control schemes overlooked the potential benefits of using time-varying control inputs. Moreover, even static wake steering control appears to have promising potential to improve wind farm performance, the spacing between turbines is still fundamentally constrained by the wake length, which limits the design of wind farm layout. Therefore, another research direction aroused: dynamic control strategies.

1-2-3 Dynamic induction & wake steering control

Wake persists for a distance until it breaks down due to its tip-vortex instability and the later interaction between the ambient air. A detailed wake-breakdown process is well explained in the studies [22], [23], as can be seen in Figure 1-2. The dynamic control strategy plays the role in fostering the wake-breakdown process and accelerating the wake recovery so that the downstream turbines can experience less wake effect.

The idea of dynamic control strategy was firstly introduced in an industrial patent (adopted from [24]). This patent described the method of dynamic control including dynamic induction and dynamic wake steering control strategies, indicating the wake recovery could be enhanced. However, there had not been simulation and experimental support for this dynamic control strategy in this patent. The first simulation work of induction dynamic control was done in the study [25]. It proposed a control algorithm to determine dynamic induction signals of turbines in a wind farm. The simulation results showed that using dynamic induction control substantially enhanced the overall wind farm power production. However, the computational time of the control algorithm was too long for a real wind farm to implement, and the heavily fluctuating induction signals could also lead to unfavorably higher fatigue loads on the excited turbines, diminishing the benefits of its energy gain. To address the issues mentioned above, a study [26] proposed to restrain the dynamic induction signal to sinusoidal shape.

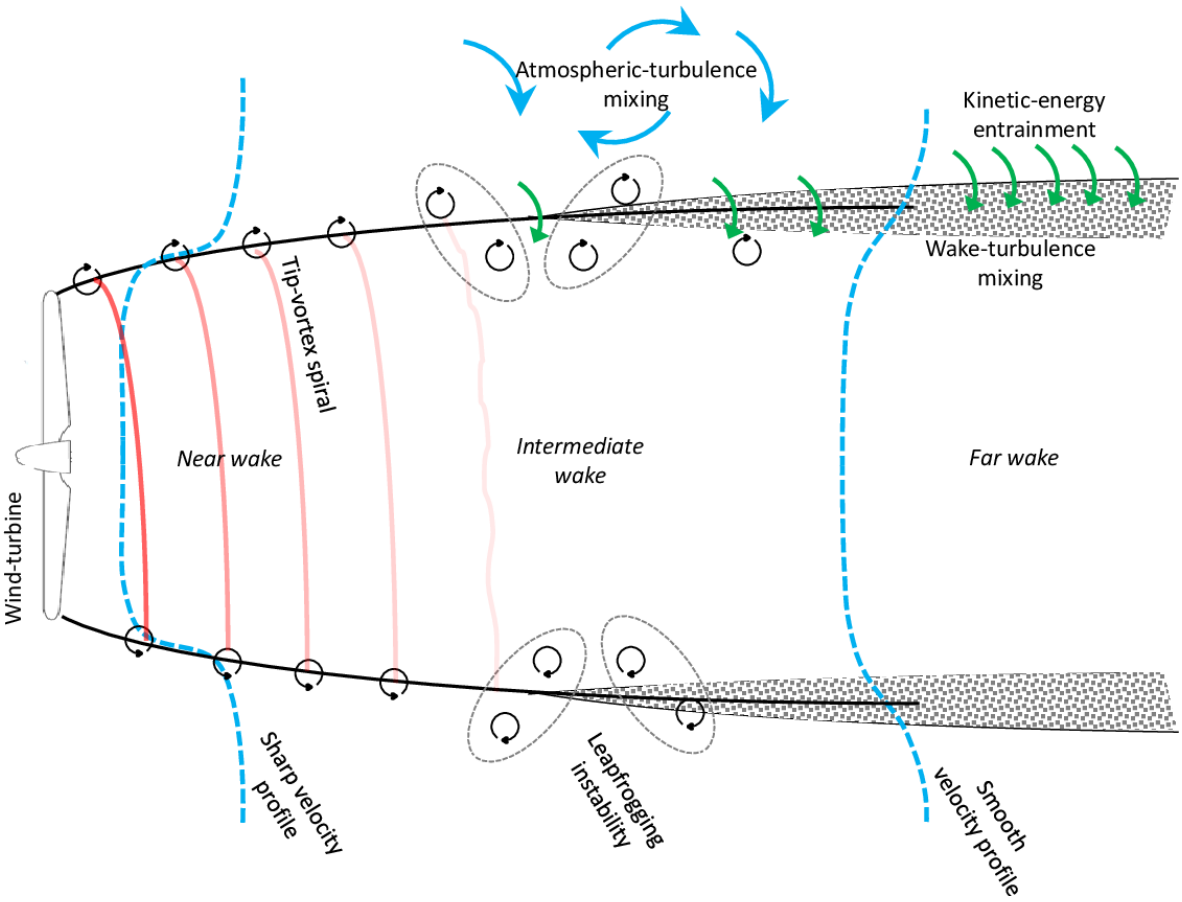

Figure 1-2: Schematic of wake-breakdown process [23]. On the boundary of the blades, vortices are formed and shedded into the wake. These vortices quickly rolled up and are concentrated into tip and root vortices, forming the rotating helical structure in the near wake region. This periodic helical structure prohibits the turbulent mixing and kinetic-energy transport across the shear layer. Due to the mutual induction between these vortices, they starts pairing and being re-oriented in the intermediate wake region. This tip-vortex pairwise instability is also called leapfrogging instability, which is the triggering event for the onset of wake breakdown. When the tip-vortex structure vanishes, the wake enters the far wake region, where the re-energizing process starts. In this region, the wake recovers its kinetic energy by turbulent mixing with the ambient air. The wake-breakdown process is affected by the inflow wind conditions, the extent of the ambient turbulence, the operating conditions of the rotor, and the dynamic behavior of the blades.

With this approach, the determination of control signals became easier and the smoother pitch inputs resulted in relatively lower fatigue loads, while the power gain compared with the unrestrained one is slightly reduced on the other hand. This method is also called periodic dynamic induction control, PDIC, since the periodic sinusoidal signal is implemented. Later, the wind-tunnel experiment of PDIC was conducted for the first time in the study [27] to validate the effectiveness of this approach. The experimental results indicated that the enhancement in power production by PDIC is better than by static induction control and is as good as by wake steering control, providing confidence in this novel approach to increase wind farm performance. In the meantime, the dynamic wake steering control was also in great research interest, which could be found in the studies [28] [29]. The simulation results of both studies showed promising enhancement in wake recovery through the implementation of dynamic wake steering control.

Compared with static control schemes, dynamic induction and dynamic wake steering control strategies tapped into the potential of using dynamic control settings to excite faster wake recovery behind rotors. These wake-mixing strategies fundamentally shorten the wake length, resulting in shorter turbine spacing, which also benefits the design of wind farm layout. Therefore, the dynamic control strategies have recently gained increasing interests both from the academia and the industry.

1-3 Research gaps

The above-mentioned dynamic control strategies have a common downside: high variation of power and loads on the excited upstream turbines. When dynamic control strategies are implemented, either through induction or wake steering, the upstream excited turbine experiences periodic deviation from its optimal operating condition. Therefore, both power and load vary periodically, leading to instability in the grid [30] and additional fatigue damage on turbine components. According to the recent simulation results [27], the equivalent damage loads on excited turbines can be more than 10% increase in the tower base, compared with the case without implementing a control strategy. Moreover, the increase of fatigue damages on turbine components can possibly diminish the benefits from the net power gain of a wind farm in the long run.

To address the mentioned setbacks seen in the conventional dynamic control strategies, a novel control strategy, the Helix approach, was lately proposed [31]. This new dynamic control strategy utilizes the individual pitch control (IPC) technique to deflect the wake dynamically in a way that the wake mixing is stimulated. The distinctive advantage of this method is that power and load variation of excited upstream turbines are substantially reduced compared with using the conventional dynamic control strategies.

The Helix approach was only conceptually proposed in the current phase. Therefore, further research is required to validate this new approach before the business case can be truly defined. Four main research gaps of the Helix approach are proposed in the following:

• Exploration of pitch input signals
The current version of the Helix approach implements the pitch input signals as a sinusoidal shape at a fixed amplitude and frequency (more details are described in Chapter 2). However, the potential of using higher harmonic signals in faster wake mixing is still unknown.

• Conduction of detailed load analysis
In the current research, only the thrust variation is simulated, which is an overall force acting on the whole rotor. The magnitude of the thrust force appears to be almost constant, but additional moments are induced since the thrust is not on the center of the rotor. However, the impacts of using the Helix approach on the fatigue loads for different turbine components, both excited upstream turbines and waked downstream turbines, are unknown and require detailed load analysis.

• High-fidelity simulation on a wind farm level
The current research demonstrated promising net power gain for a two-turbine system through a high-fidelity simulation. However, the high-fidelity simulation for multiple-turbine system has not been conducted yet, which could further demonstrate the full potential of using the Helix approach on the wind farm level. In this case, a closed-loop algorithm that determines the control policies of individual turbine to achieve a certain objective, such as power maximization and load minimization, is also unknown and requires further investigation.

• Conduction of experiments, field tests, and full-scale tests
In the current development of the Helix approach, only simulation work has been performed. The real data for validation of the simulation results is not yet available. Laboratory experiments, field tests as well as full-scale tests are required to obtain data both in well-controlled and realistic wind conditions.

1-4 Thesis goal and approach

The purpose of this master's thesis is to fill the first research gap mentioned in Section 1-3, which is the exploration of pitch input signals. Therefore, the thesis goal is the following:

Thesis goal: Explore the potential of using multiple sinusoidal pitch input signals in the Helix approach to further stimulate wake mixing to achieve faster wake recovery.

To achieve the goal, the following questions are structured to be addressed:

Question 1: How is the existing IPC and Helix control framework used to effectuate a framework for the synthesis of a multi-sine Helix control strategy?

The thrust force is the overall force the rotor exerting on the wind flow, which is the driving force of forming the wake. Therefore, the dynamic behavior of the thrust force induces the dynamic formation of the wake, which leads to the instability and the earlier breakdown of the wake. For example, in the PDIC, the magnitude of the thrust force is dynamically manipulated, which induces the "pulse" shape of the wake. In the Helix approach, the position of the thrust force is manipulated, which induces the helical shape of the wake. However, in the current study of the Helix approach, the concept of thrust-position manipulation is unclear. To effectively design the non-single-sine pitch input signals, it is essential to understand how the position of the thrust force is manipulated by implementing these signals, which is presented in Chapter 2.

Question 2: How to simulate the wake development at a preferable computational cost?

The dynamic thrust force induces the instability in the wake development, which fosters the wake-breakdown process. To investigate the impact of different dynamic-thrust-force profiles on the wake breakdown, a simulation package capable of simulating the complex physics in the wake development is required. Moreover, the combinations of non-single-sine pitch input signals are in large range, theoretically infinite range, so a wide investigation is expected to be done at the first place. Therefore, the simulation package which is at a reasonable computational cost is preferred, which is presented in Chapter 3.

Question 3: How to compare the effectiveness of the Helix approach under different pitch input signals?

For distinct pitch input signals, the effectiveness of the Helix approach is expected to be different. When comparing these cases, fairness should be maintained. For example, higher amplitudes of pitch input signals are expected to have better wake mixing performance than the ones with lower amplitudes. However, the ones with higher amplitudes also increase the actuator duty cycle, which in turn reduces the lifetime of pitch bearings. Therefore, the criteria of comparing different cases should be considered. Moreover, based on the simulation package that is used, the method of analyzing the output data that could demonstrate the extent of the wake breakdown is expected to be figured out, which is presented in Chapter 4.

1-5 Report structure

This section briefly summarizes the remainder of this report for each of the chapters:

Chapter 2 introduces the framework of implementing the Helix approach. In this chapter, the correlation between the pitch profiles and the thrust force manipulation is explained.

Chapter 3 introduces the wake models from the low to the high fidelity. The free vortex wake model is adopted in this study, in which its theory, advantages and limitations are also elaborated in this chapter.

Chapter 4 presents the environment where the simulation is performed, including the specification of the wind turbine model, the controller model, and the wind inflow conditions. Moreover, the implementation of the Fourier stability analysis is explained. At the end of the chapter, the simulation cases are clarified.

Chapter 5 demonstrates the simulation results in the orders of the blade actuation activities, the thrust force manipulation and the wake development. At the end of this chapter, discussions about the results are given.

Chapter 6 presents the conclusions of the thesis, which are followed by the recommendations for the improvement of the current study and the potential topics for the future studies.

Chapter 2

The Helix Approach

As mentioned in Section 1-3, the Helix approach was proposed as an alternative wake-mixing strategy. Instead of varying the magnitude of the thrust force as in PDIC, the Helix approach utilizes the turbine's ability to pitch its blades individually to distinct angles to manipulate the position of the thrust force on the rotor plane such that faster wake mixing is stimulated. This way of pitching turbine blades is called the individual pitch control (IPC) technique, which was already exploited for the blade fatigue load reductions. The multi-blade coordinate (MBC) transformation is adopted in the IPC technique as a link for signals between the rotating and the fixed frame. The Helix approach also takes advantage of the MBC transformation to achieve the effective way of designing the individual pitch signals for each blade.

In this chapter, the implementation of the Helix approach is presented in more details, which is structured as follows. Section 2-1 introduces the conventional application of the IPC technique. Section 2-2 presents the theory of the MBC transformation. Finally, Section 2-3 explains the implementation details of the Helix approach.

2-1 Individual pitch control

A modern wind turbine is designed with an extremely large rotor diameter which is normally more than hundred meters to capture more wind energy [32]. Due to the wind shear, the tower shadow effect and the increased flexibility of the blades, the aerodynamic loads across the rotor plane becomes more asymmetric, leading to the periodic loads on the turbine components when the rotor is rotating.

The Individual pitch control (IPC) is a technique where the pitch of the blade is individually controlled in a desired way such that these periodic loads can be alleviated. The initial research of the IPC is given in the study [33], which employed a simple control algorithm with a PI-controller to achieve desired individual pitching. The simulation results indicated significant reduction in the periodic loads by using IPC. This method was later validated in

the studies [34], [35] through experiments, in which both results showed that the load reduction predicted by simulation could possibly be achieved in practice. Moreover, the study [36] further improved this IPC algorithm to realize even better load reduction. However, the main downside of the aforementioned IPC, or so-called conventional individual pitch control (CIPC), was the substantially increased pitch actuator duty cycle (ADC), which would cause undesirably high wear on the pitch bearings of the blades.

Therefore, a novel IPC technique was proposed and simulated in the study [37] to address the aforementioned issues by using the data-driven approach. This methodology is called subspace predictive repetitive control (SPRC), which uses the measurements of the bending moments on the blades to determine optimal IPC control inputs. Since the control inputs are generated to only alleviate specified deterministic loads, the ADC is substantially reduced. This novel approach was latter validated through the wind tunnel experiments both in a uniform flow condition in the study [38] and in a more realistic turbulent flow condition in the study [39], in which both results showed promising potential of using SPRC in practice.

To summarize, the IPC technique has been applied in the wind turbine operation to alleviate the periodic loads on the turbine components. The Helix approach is developed based on the well-developed IPC technique described in this section, and the application is extended to the area of the wake-mixing control strategy for the first time. To effectuate the IPC technique, the MBC transformation is adopted.

2-2 Multi-blade coordinate transformation

In a multi-bladed rotor system, blade dynamics is often expressed in the rotating frames. In other words, quantities of each rotating blade are described on its own coordinates attached to them. However, it is of great interest to also understand the coupled effects of these quantities, which are expressed in the fixed frame. For example, the rotor and the tower-nacelle subsystem always see and response to the effects of the blades as a whole instead of individually. Therefore, the multi-blade coordinate (MBC) transformation, which is also referred as the Fourier coordinate transformation or the Coleman transformation in the literature, is introduced as a mathematical tool to project the rotating frames on the single fixed frame. Figure 2-1 shows that the MBC and the inverse MBC transformation are the links between the rotating frames and the fixed frame. The MBC transformation was firstly used in the field of the helicopter where the rotor dynamics is of interest, and it was later on widely applied in the field of wind turbine [40]. In the remainder of this section, the MBC and the inverse MBC transformation are presented, which is according to Johnson's work [41].

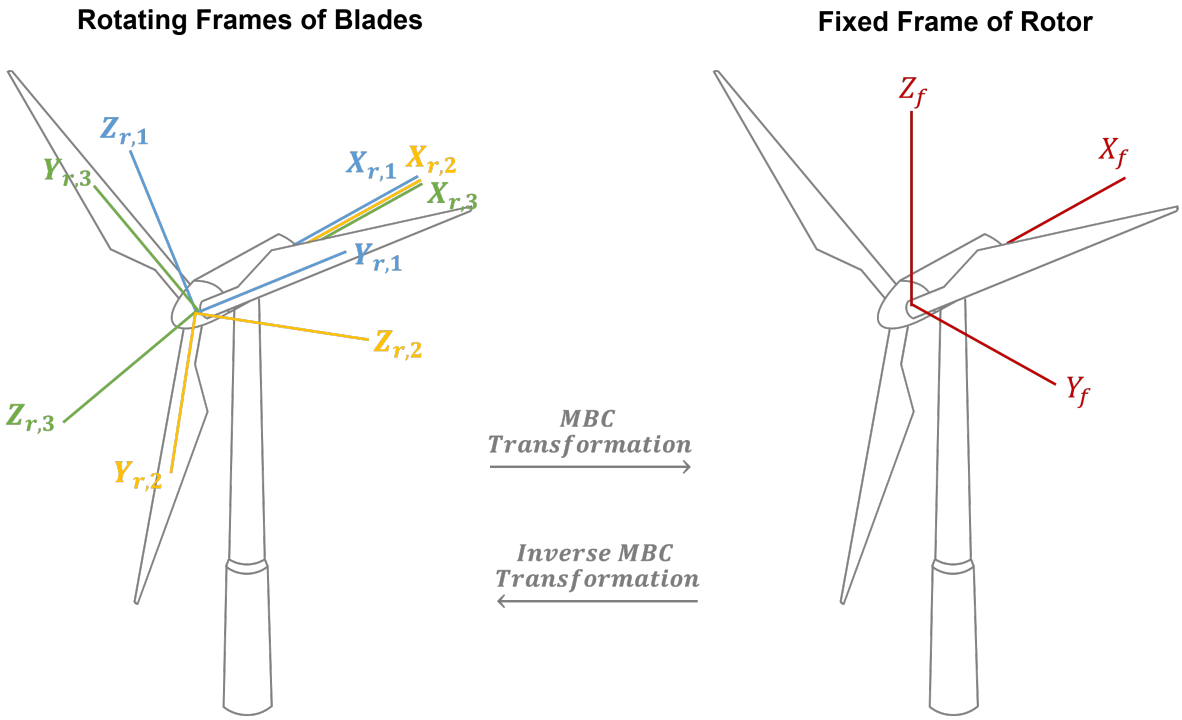

Figure 2-1: The coordinates of the rotating frames of blades (left) and the coordinates of the fixed frame of rotor (right) for a three-bladed turbine. Index r and f represents the term of *rotating* and *fixed*, respectively. The MBC transformation is implemented to combine the individual rotating frames (expressed in the color blue, yellow and green) into the fixed frame (expressed in the color red). The inverse MBC transformation works in the opposite way.

Consider a rotor of N blades equidistantly located. The azimuth location of b^{th} blade, Ψ_b, is expressed by Eq. (2-1), where Ψ is the azimuth position of the first blade. It is assumed that Ψ is zero when the first blade is vertically pointing up and it increases in the clockwise direction, where $\{\Psi \in \mathcal{R} : 0 \leq \Psi < 2\pi\}$.

$$\Psi_b = \Psi + (b-1)\,\frac{2\pi}{N} \tag{2-1}$$

Let q_b be a certain quantity on the b^{th} rotating blade, which is a function of the azimuth position of that blade, Ψ_b . For each blade at different Ψ_b, q_b has a different effect on the overall rotor plane. To combine these individual effects into an overall effect, the MBC transformation expressed by Eq. (2-2), Eq. (2-3) and Eq. (2-4) are introduced, where n is the harmonic index, q_0, q_{nc} and q_{ns} are the combined quantity expressed in the direction of collective, n-cosine-cyclic and n-sine-cyclic of the fixed frame, respectively, which corresponds to X_f, Y_f and Z_f in Figure 2-1.

$$q_0 = \frac{1}{N}\sum_{b=1}^{N} q_b \tag{2-2}$$

$$q_{nc} = \frac{2}{N}\sum_{b=1}^{N} q_b \cos\left(n\Psi_b\right) \tag{2-3}$$

$$q_{nc} = \frac{2}{N} \sum_{b=1}^{N} q_b \sin(n\Psi_b) \tag{2-4}$$

Combining Eqs. (2-2)-(2-4), a matrix form of the MBC transformation is obtained in Eq. (2-5).

$$\begin{bmatrix} q_0 \\ q_{nc} \\ q_{ns} \end{bmatrix} = \frac{2}{N} \begin{bmatrix} 1/2 & 1/2 & ... & 1/2 \\ \cos(n\Psi_1) & \cos(n\Psi_2) & ... & \cos(n\Psi_N) \\ \sin(n\Psi_1) & \sin(n\Psi_2) & ... & \sin(n\Psi_N) \end{bmatrix} \begin{bmatrix} q_1 \\ q_2 \\ . \\ . \\ . \\ q_N \end{bmatrix} \tag{2-5}$$

The fixed frame is transformed back to the rotating frames by using the inverse MBC transformation, which is expressed in the matrix form by Eq. (2-6).

$$\begin{bmatrix} q_1 \\ q_2 \\ . \\ . \\ . \\ q_N \end{bmatrix} = \begin{bmatrix} 1 & \cos(n\Psi_1) & \sin(n\Psi_1) \\ 1 & \cos(n\Psi_2) & \sin(n\Psi_2) \\ . & . & . \\ . & . & . \\ . & . & . \\ 1 & \cos(n\Psi_N) & \sin(n\Psi_N) \end{bmatrix} \begin{bmatrix} q_0 \\ q_{nc} \\ q_{ns} \end{bmatrix} \tag{2-6}$$

2-3 Implementation of the Helix approach

The Helix approach exploits the IPC technique (Section 2-1) to manipulate the wake, and it is realized by the implementation of the MBC transformation (Section 2-2). The framework of the Helix approach is shown in Figure 2-2, and details of each part of the figure are elaborated in the subsequent sections.

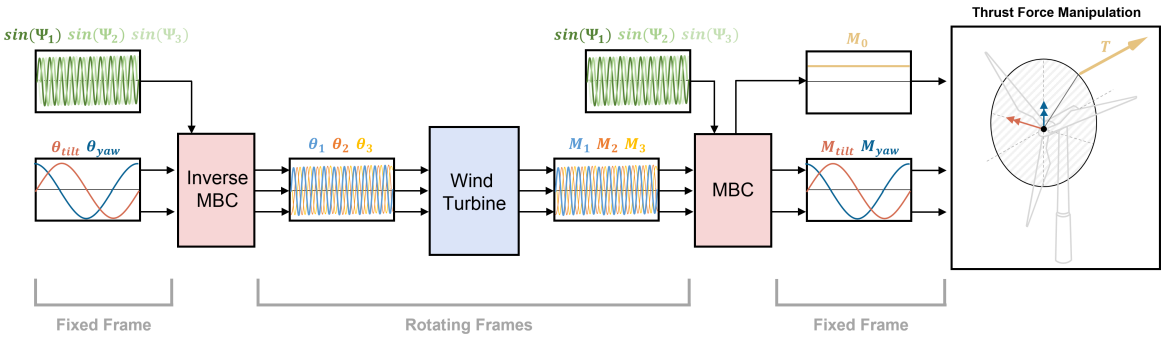

Figure 2-2: The framework of the Helix approach. The Helix approach is based on the individual blade pitching. Suppose the blade-pitch signals, θ_1, θ_2 and θ_3, are implemented on the individual blades, then they would result in the corresponding blade-root-moment signals, M_1, M_2 and M_3, where these six signals are expressed on the rotating frames (middle part). The MBC transformation is implemented on the blade-root-moment signals to obtain the combined effects of these moment signals on the fixed frame, which are expressed in the tilt and the yaw direction, M_{tilt} and M_{yaw} (right-half part). In the similar manner, the blade-pitch-signals are obtained through the implementation of the inverse MBC transformation on the tilt and the yaw pitch input signals on the fixed frame, θ_{tilt} and θ_{yaw} (left-half part). The relationship between the pitch input signals and the moment signals on the fixed frame are therefore obtained. The occurrence of the tilt and the yaw moment signals implies that the thrust force is not acting on the rotor center. In other words, the position of the thrust force can be manipulated by implementing the pitch input signals, which is seen as an effective way to dynamically deflect the wake.

2-3-1 Rotating-frame signals

As discussed in Section 2-2, the dynamics of a multi-bladed rotor system is generally described in the rotating frames of the individual blades. Therefore, in the case of a three-bladed turbine, there are three blade-pitch signals describing the pitch motions of the individual blades, which are expressed in θ_1, θ_2 and θ_3. As the rotor is rotating, the out-of-plane moments are induced on the blade roots by the aerodynamic force acting on the blades, and these blade-root-moment signals are expressed in M_1, M_2 and M_3.

In the Helix approach, the blades are individually pitched. In doing so, the aerodynamic force acting on each of the blades alters, which creates the corresponding response in the blade-root moment. It is assumed that the wind turbine is a linear system, so the pitch perturbations would result in a amplitude-scaled and phase-shifted response in the blade-root moment signals with the same frequency content. Therefore, similar profiles of the blade-pitch and the

blade-root-moment signals can be observed, which is shown in the middle part of Figure 2-2.

2-3-2 Fixed-frame signals

It is essential to gain the insights of how these individual pitch motions eventually affect the wake development in order to effectively design the IPC profiles. Therefore, the MBC transformation is utilized to help understand the combined effects of the individual signals from the blades.

The MBC transformation is firstly implemented on the blade-root-moment signals, as shown in the right-half part of Figure 2-2. Using Eq. (2-5) with the harmonic index of $n = 1$ in the three-bladed system of $N = 3$, the matrix of the MBC transformation on the blade-root-moments can be expressed by Eq. (2-7) and Eq. (2-8), where M_0, M_{tilt} and M_{yaw} are collective, tilt and yaw root moments on the rotor fixed frame, respectively, $T(\Psi)$ is the MBC transfer function, and Ψ_1, Ψ_2 and Ψ_3 are the the azimuth position of the blades.

$$\begin{bmatrix} M_0 \\ M_{\text{tilt}} \\ M_{\text{yaw}} \end{bmatrix} = T(\Psi) \begin{bmatrix} M_1 \\ M_2 \\ M_3 \end{bmatrix} \tag{2-7}$$

$$T(\Psi) = \frac{2}{3} \begin{bmatrix} 1/2 & 1/2 & 1/2 \\ \cos(\Psi_1) & \cos(\Psi_2) & \cos(\Psi_3) \\ \sin(\Psi_1) & \sin(\Psi_2) & \sin(\Psi_3) \end{bmatrix} \tag{2-8}$$

By using the MBC transformation, the individual blade-root-moments on the rotating frames are combined and re-expressed by the tilt and the yaw moments on the fixed frame. In the meantime, the collective moment is also calculated by averaging these three blade-root-moments, which represents the overall magnitude of the moment relative to the center of the rotor.

It is noted that the frequencies of the tilt and the yaw moment signals are different from the blade-root-moment signals since the rotating frequency of the rotor is decoupled after implementing the MBC transformation. The frequencies of the tilt and the yaw moment signals are purely induced by the corresponding tilt and yaw pitch input signals, θ_{tilt} and θ_{yaw}. In order to link these pitch input signals to the individual blade-pitch signals, the inverse MBC transformation is used. Similarly to the derivation of the MBC transformation, the inverse MBC transformation is derived by adopting the harmonic index of $n = 1$ and the three-bladed system of $N = 3$ in Eq. (2-6), as expressed by Eq. (2-9) and Eq. (2-10), where $T^{-1}(\Psi)$ is the inverse MBC transfer function. It is shown in the left part of Figure 2-2.

$$\begin{bmatrix}\theta_1\\ \theta_2\\ \theta_3\end{bmatrix} = T^{-1}(\Psi)\begin{bmatrix}\theta_0\\ \theta_{\text{tilt}}\\ \theta_{\text{yaw}}\end{bmatrix} \tag{2-9}$$

$$T^{-1}(\Psi) = \begin{bmatrix}1 & \cos(\Psi_1) & \sin(\Psi_1)\\ 1 & \cos(\Psi_2) & \sin(\Psi_2)\\ 1 & \cos(\Psi_3) & \sin(\Psi_3)\end{bmatrix} \tag{2-10}$$

By doing so, the relationship between the pitch input signals and the root moment signals is eventually obtained. These signals are both expressed in the tilt and the yaw direction on the fixed frame, and the pitch input signals have the direct control over the moment signals. That is, if a single sinusoidal tilt pitch input signal is implemented, for example, a tilt moment signal with the same frequency is obtained. This also applies to the yaw signals, which means the fixed-frame moment on the rotor can be manipulated through the implementation of the tilt and the yaw pitch input signals.

2-3-3 Thrust force manipulation

The occurrence of the tilt and the yaw moment signals implies that the thrust force is not acting on the center of the rotor. Specifically speaking, when the blades are pitched individually, each blade may experience different aerodynamic-force distribution, and the imbalance force from three blades moves away the thrust force from the center of the rotor, creating the moment with respect to the rotor center. Since the thrust force is the overall force the rotor exerts on the wind flow, which forms the wake behind the rotor, the deflection of the wake can be induced by the dynamic manipulation of thrust-force position.

Figure 2-3 demonstrates the thrust-force manipulation, where T is the thrust force, y_{T} and z_{T} is the horizontal and the vertical coordinate distance between the thrust force and the rotor center, respectively. The calculation of y_{T} and z_{T} can be done through dividing the yaw and the tilt moment signals by the magnitude of the thrust force, expressed by Eq. (2-11) and Eq. (2-12). It is noted that the negative sign in Eq. (2-12) is for the purpose of being consistent with conventional expression of the moment.

$$y_{\text{T}} = \frac{M_{\text{yaw}}}{T} \tag{2-11}$$

$$z_{\text{T}} = -\frac{M_{\text{tilt}}}{T} \tag{2-12}$$

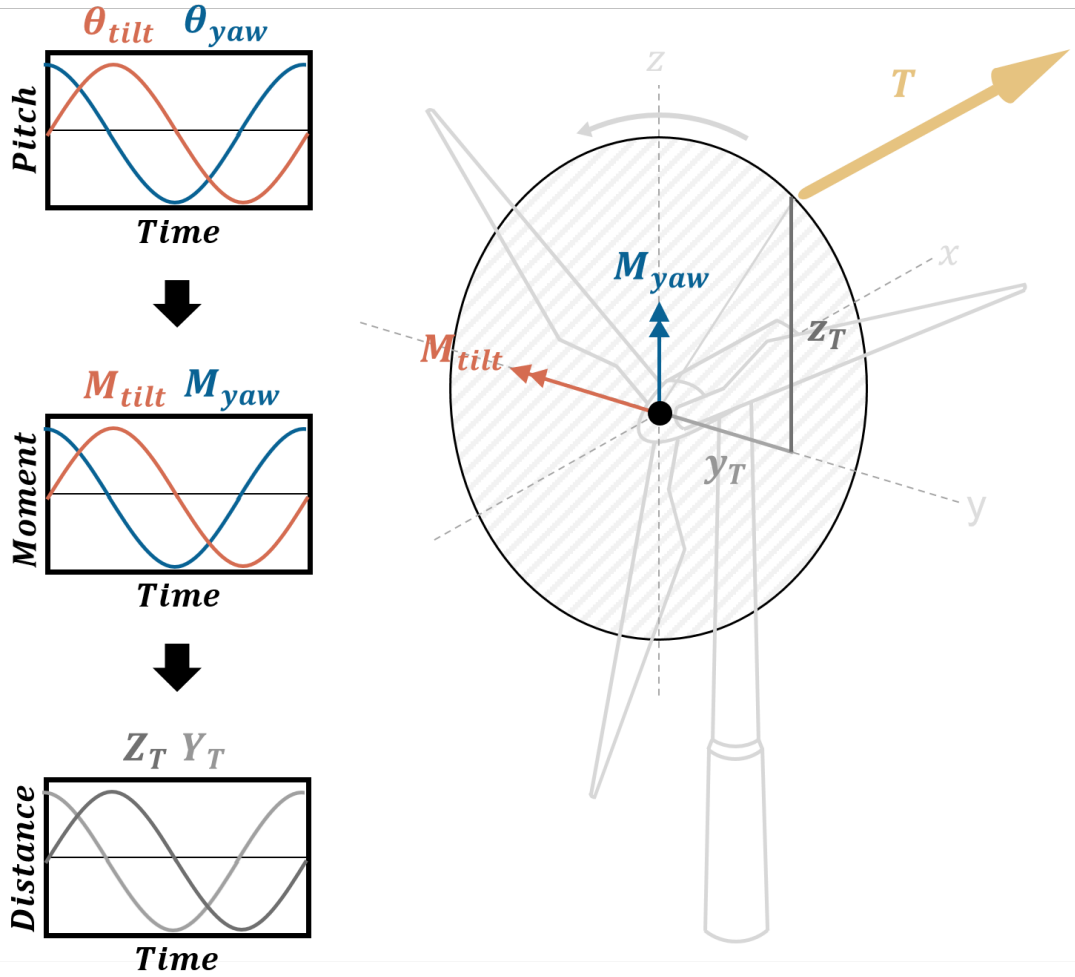

Figure 2-3: The illustration of the thrust manipulation. The tilt and the yaw pitch input signals are implemented into the blades (left-top), which induces the corresponding tilt and yaw moment signals on the rotor (left-middle). The occurrence of the moments implies that the thrust force is not acting on the rotor center, where the distance between the thrust force and the rotor center can be calculated through dividing the moments by the magnitude of the thrust force (left-bottom). By implementing different combinations of the tilt and the yaw pitch input signals, the dynamic position of the thrust force is determined, which can be used to manipulate the wake deflection. In the case of single-sine input signals where the tilt signal is $\pi/2$ ahead of the yaw signal, the thrust position rotates counterclockwise around the rotor center (right).

2-3-4 Design of pitch input signals

To summarize, the position of the thrust force on the rotor plane is manipulated by implementing the tilt and the yaw pitch input signals. Therefore, the combination of the tilt and the yaw pitch input signals directly determines the thrust-force trajectory, which eventually affects the wake development. In this section, three forms of designing the pitch input signals are demonstrated: single-sine signals, multi-sine signals and higher harmonic single-sine signals.

Single-sine signals
For the single-sine signals, both the tilt and the yaw signals are constrained in the sinusoidal shape, with their general forms expressed in Eq. (2-13) and Eq. (2-14), where θ^*_{tilt} and θ^*_{yaw} are the tilt and the yaw pitch amplitudes, $f_{e,\,\text{tilt}}$ and $f_{e,\,\text{yaw}}$ are the tilt and the yaw excitation frequencies, and Φ is the phase difference between the tilt and the yaw pitch input signals.

$$\theta_{\text{tilt}} = \theta^*_{\text{tilt}}\ \sin\left(f_{e,\,\text{tilt}}\, t\right) \tag{2-13}$$

$$\theta_{\text{yaw}} = \theta^*_{\text{yaw}}\ \sin\left(f_{e,\,\text{yaw}}\, t + \Phi\right) \tag{2-14}$$

For the typical Helix approach demonstrated in the study [31], the amplitudes as well as the frequencies of the tilt and the yaw signals are the same, and the tilt pitch input signal is $\pi/2$ ahead of the yaw pitch input signal. The combination of the aforementioned input signals results in the constant thrust force rotating counterclockwise around the rotor center (in the upfront view), as shown in Figure 2-3, in which the thrust force deflects the wake into the counterclockwise helical shape.

It is noted that each of the parameters in Eq. (2-13) and Eq. (2-14) affects the trajectory of the thrust force. For example, in the previous case if the tilt pitch input signal becomes $\pi/2$ lagged behind the yaw pitch input signal, the position of the thrust force would rotate in the clockwise direction.

Multi-sine signals
As mentioned in Section 1-4, the thesis goal is to explore the potential of using non-single-sine pitch input signals to achieve better wake mixing. Therefore, using the multi-sine as pitch input signals is explored in this study. The general forms of multi-sine signals are expressed by Eq. (2-15) and Eq. (2-16), where i is the index number of each component signal and N is the total number of the component signals.

$$\theta_{\text{tilt}} = \sum_{i=1}^{N} \theta^*_{\text{tilt},\,i}\ \sin\left(f_{e,\,\text{tilt},i}\, t\right) \tag{2-15}$$

$$\theta_{\text{yaw}} = \sum_{i=1}^{N} \theta^*_{\text{yaw},\,i}\ \sin\left(f_{e,\,\text{tilt},i}\, t + \Phi_i\right) \tag{2-16}$$

Generally, the implementation of the multi-sine signal is employed in the field of system identification, for example, as discussed in the studies [42] and [43]. The excitation signal is applied to the system, and the information of the system can be obtained by sampling and analyzing the response signal. Single-sine signal is normally used as the excitation signal, and the sampling frequency is required to be high enough to ensure the information of the system is retained from the leakage and the aliasing. However, for the nonlinear system, higher harmonics can be induced, which requires the higher sampling rate, and this leads to the increased cost of power for the hardware to perform the higher-frequency sampling [42]. One way to avoid the sampling errors such as leakage and aliasing is to implement the well-designed multi-sine excitation signal, which can be done by the the crest factor optimization [43]. By doing so, the higher harmonics induced by the system nonlinearity can be accommodated by the multi-sine signals, and the lower sampling rate can be achieved to reduce the sampling cost. It is noted that a multi-sine signal is composed of several single-sine signals containing multiple excitation frequencies, amplitudes and phases, and this provides the flexibility to design the pitch input signals in the Helix approach.

Higher harmonic single-sine signals

As mentioned in Section 2-2, the MBC transformation can also be implemented with higher harmonic indices. For example, in a recent study [44], the combined harmonic indices of one and two, which are expressed as 1P and 2P, are used in the IPC technique to further reduce higher harmonic loads. Therefore, in this study, the potential of utilizing higher harmonic single-sine signals is investigated.

The implementation of combined 1P and 2P harmonic signals is shown in Figure 2-4. It is noted that the tilt and the yaw pitch input signals are both in the form of single-sine, and 2P pitch input signals have the same amplitude and phase as the 1P pitch input signals but with the excitation frequency twice higher. The blade-pitch signals, θ_1, θ_2 and θ_3, is obtained by Eq. (2-17), Eq. (2-18) and Eq. (2-19).

$$\begin{bmatrix}\theta_1\\ \theta_2\\ \theta_3\end{bmatrix} = T^{-1}_{\text{1P}}(\Psi)\begin{bmatrix}\theta_{0,\,\text{1P}}\\ \theta_{\text{tilt},\,\text{1P}}\\ \theta_{\text{yaw},\,\text{1P}}\end{bmatrix} + T^{-1}_{\text{2P}}(\Psi)\begin{bmatrix}\theta_{0,\,\text{2P}}\\ \theta_{\text{tilt},\,\text{2P}}\\ \theta_{\text{yaw},\,\text{2P}}\end{bmatrix} \tag{2-17}$$

$$T^{-1}_{\text{1P}}(\Psi) = \begin{bmatrix}1 & \cos(\Psi_1) & \sin(2\Psi_1)\\ 1 & \cos(\Psi_2) & \sin(2\Psi_2)\\ 1 & \cos(\Psi_3) & \sin(2\Psi_3)\end{bmatrix} \tag{2-18}$$

$$T^{-1}_{\text{2P}}(\Psi) = \begin{bmatrix}1 & \cos(2\Psi_1) & \sin(2\Psi_1)\\ 1 & \cos(2\Psi_2) & \sin(2\Psi_2)\\ 1 & \cos(2\Psi_3) & \sin(2\Psi_3)\end{bmatrix} \tag{2-19}$$

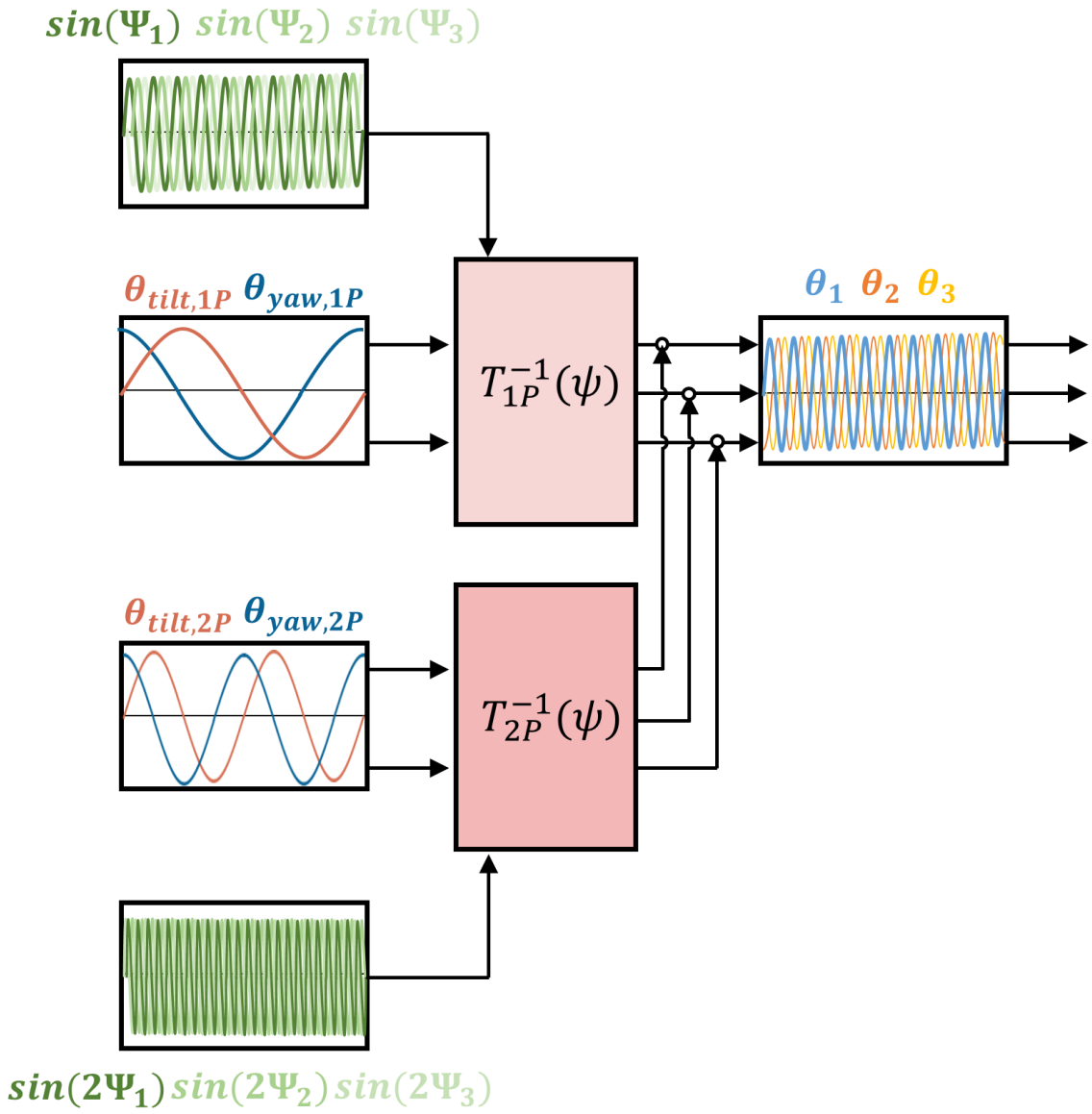

Figure 2-4: The implementation combined 1P and 2P harmonic signals. The 1P and 2P inverse MBC transformation is implemented on the 1P and 2P (tilt and yaw pitch) input signals, respectively. The outputs from the inverse MBC transformations are linearly combined to obtain the blade-pitch signals.

Chapter 3

Wake Modeling

The wake modeling focuses on simulation of the flow behind the rotor by these two main characteristics: (1) the velocity deficit, and (2) the increased level of turbulence. The former reduces kinetic energy of wind and the latter imposes unsteady loads on the downstream turbines. Hence, it is of great importance to develop a model that is able to simulate these characteristics of the wake. However, the wake is a complicated dynamic process as previously mentioned in Figure 1-2, and directly modeling the fluid dynamics of the wake requires extremely high computational cost which is impractical for engineering purposes. Generally, the less assumptions are made in the fluid dynamics solver, the more computational cost it takes. Therefore, there have been a great variety of wake models with varying fidelity developed for different purposes, which are well reviewed in the studies [45], [46] and [47]. In fact, these wake models are not viewed as competitors to each other. Instead, they are chosen depending on different scenarios. For example, a relatively simple and computationally efficient model is of greater interest to be used to predict the annual energy production of a wind farm in an early design phase, while a higher-fidelity model that is able to simulate the vortical structures and turbulence during the wake development becomes necessary when a wake-mixing control strategy is investigated.

In this chapter, wake models with different fidelity are introduced. Section 3-1 elaborates a simple and widely used wake model in the wind industry. Section 3-2 presents the turbulence models that are able to simulate more realistic behavior of the wake. Last, Section 3-3 introduces the theory of the free vortex wake model that is adopted in this thesis.

3-1 Kinetic model

3-1-1 Jensen's single wake model

The kinetic model is the model that is solely derived by the steady-state mass and momentum conservation of the wind flowing through the wind turbine. The most widely used kinetic

model is Jensen's wake model [48], later on modified by Katic et al [49], which is also known as the Modified Park model.

Consider the wind flows through the wind turbine, the wind is slowed down by the rotor and is transformed into the wake with lower wind speed and higher turbulence level behind the rotor. The wake recovers its kinetic energy by interacting with the ambient wind at the shear layer, and the wake region expands in the downstream direction. In the Jensen's wake model, assumptions are made that the wake expands linearly, and the velocity is uniformly distributed in every cross section of the wake, which results in the "hat-shaped" velocity profile depicted in Figure 3-1.

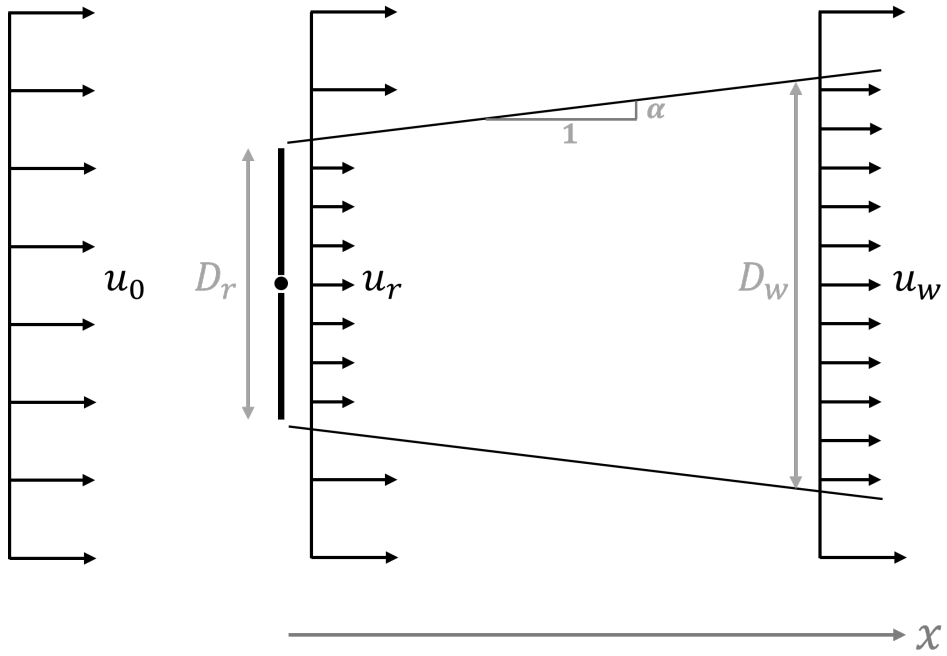

Figure 3-1: The control volume of the wind flowing through the wind turbine in the Jensen's wake model (adopted and modified from [50]), where u_0 is the free-stream wind speed, u_r is the wind speed at the rotor, u_w is the wind speed of the wake, D_r is the rotor diameter, D_w is the wake diameter, α is the wake decay coefficient, and x is the rotor-axis direction. The wake is assumed to expand linearly with the wake decay coefficient, α, which means the wake diameter can be expressed by $D_w = D_r + 2\alpha x$.

The mass balance is applied between the rotor plane and the downstream flow in the wake, which is described by Eq. (3-1). In the equation, the left side represents the volumetric flow rate at the rotor plane and the right side represents the volumetric flow rate at the downstream flow in the wake, where the mass density of the flow is assumed constant.

$$\frac{\pi D_r^2}{4}(u_r - u_0) = \frac{\pi D_w^2}{4}(u_w - u_0) \tag{3-1}$$

According to the Betz theory [51] which deploys the momentum and energy conservation of the flow, the relationship between the wind speed at the rotor plane, u_r, and the free-stream wind speed, u_0, is expressed by Eq. (3-2) and Eq. (3-3), where a is the axial induction factor, and C_T is the thrust coefficient.

$$u_r = u_0(1 - 2a) \tag{3-2}$$

$$a = \frac{1 - \sqrt{1 - C_T}}{2} \tag{3-3}$$

By substituting Eq. (3-2) and Eq. (3-3) into Eq. (3-1) and applying the correlation of the wake-diameter expansion, $D_w = D_r + 2\alpha x$, the wind-deficit profile, $\frac{u_w}{u_0}$, as the function of the downstream distance, x, is derived in Eq. (3-4).

$$\frac{u_w}{u_0} = 1 - \frac{1 - \sqrt{1 - C_T}}{(1 + 2\alpha x/D_r)^2} \tag{3-4}$$

It is noted that the wake decay coefficient, α, describes how quickly the wake expands with the distance, and this factor is dependent on the site conditions, which is determined from the data collected from the given wind farm [52]. It can be estimated by the analytical expression given by Eq. (3-5), where z is the hub height of the wind turbine, and z_0 is the surface roughness of the wind farm. Generally, the α on the onshore and the offshore surface is about 0.075 and 0.04, respectively. A typical velocity profile obtained by the Jensen's wake model is given in Figure 3-2

$$\alpha = \frac{0.5}{ln(\frac{z}{z_0})} \tag{3-5}$$

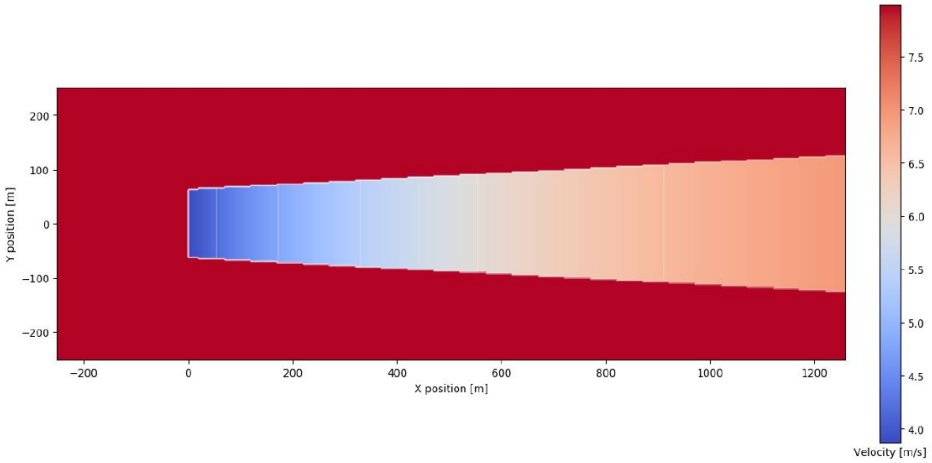

Figure 3-2: The velocity profile on the horizontal plane obtained by the Jensen's wake model (adopted from [47]). The wake is assumed to expand linearly, and the velocity is uniformly distributed at each cross section perpendicular to the rotor axis.

3-1-2 Jensen's multiple wake model

The Jensen's single wake model is introduced in the previous section, describing the velocity profile along the downstream distance. However, in the wind farm, a group of turbines are placed together, which makes these wakes overlapped with each other. For a given wind turbine, it is normally shadowed by multiple wakes from upstream wind turbines, and the performance of the given turbine is affected by the multiple wake effect [53], as demonstrated in Figure 3-3.

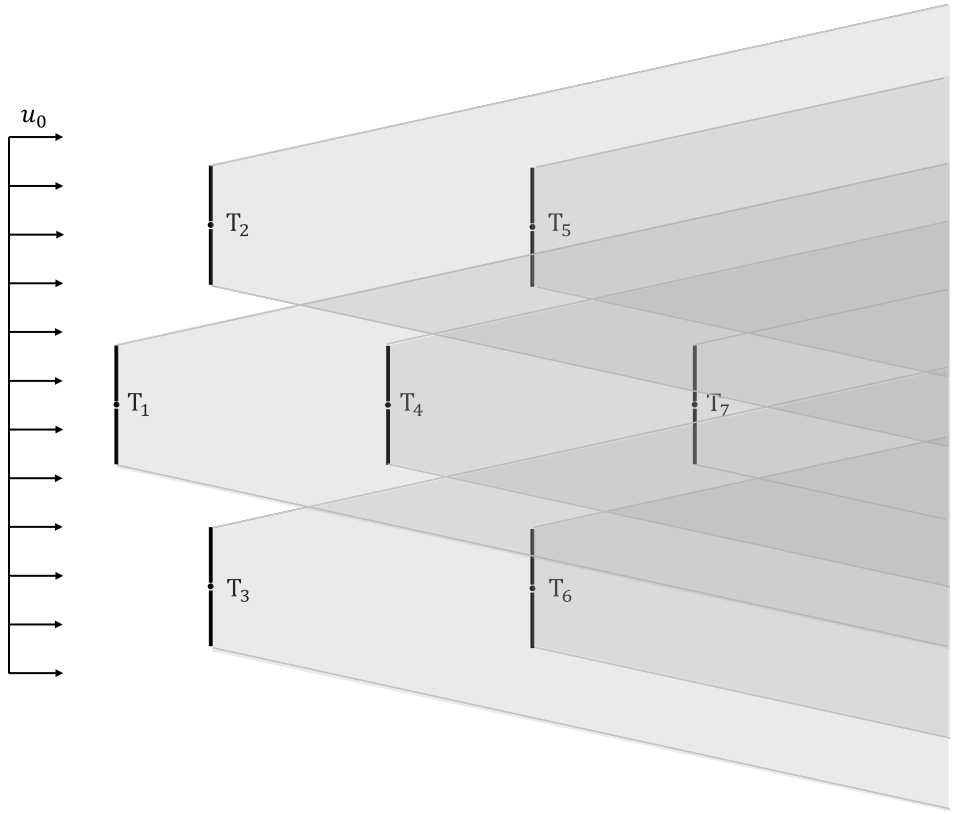

Figure 3-3: The illustration of the multiple wake effect. There are seven wind turbines ($T_1 - T_7$) with free-stream wind speed of u_0. Behind every turbine, the wake is formed and propagated to downstream turbines. These wakes overlapped with each other, and are expressed in darker colors. T_1, T_2, and T_3 are facing the free-stream wind, while T_4 is standing in the full wake of its upstream turbine T_1. For T_5 and T_7, they do not only experience the full wake of their upstream turbine but are also "shadowed" by the wake of T_1. For T_7, it is affected by the full wakes from two upstream turbines, T_1 and T_4, and the partial wakes of two neighbouring turbines, T_2 and T_3.

In order to combine the wake effects from all the upstream turbines into a single wake effect, the shadowed areas contributed by these wakes should be derived, with a detailed model illustrated in Figure 3-4. Consider the wind turbine, WT_j, is placed at the downstream from another wind turbine, WT_i, where the relative location of these turbines can be described by x_{ij} and d_{ij}. WT_j with the rotor diameter of R_0 is partially standing in the wake of WT_i with its diameter of r_i. The shadowed area, $A_{\mathrm{shadow},i}$ can be derived by adding two circular sectors of angle, θ_i and θ_j, and subtracting the diamond area of d_{ij} by Z_{ij}, which is illustrated in Eq. (3-6). The effective wind speed experienced by WT_j is denoted as $u_j(x_{ij})$, which can be calculated by weight-averaging the kinetic energy of wakes generated by n turbines, as illustrated in Eq. (3-7).

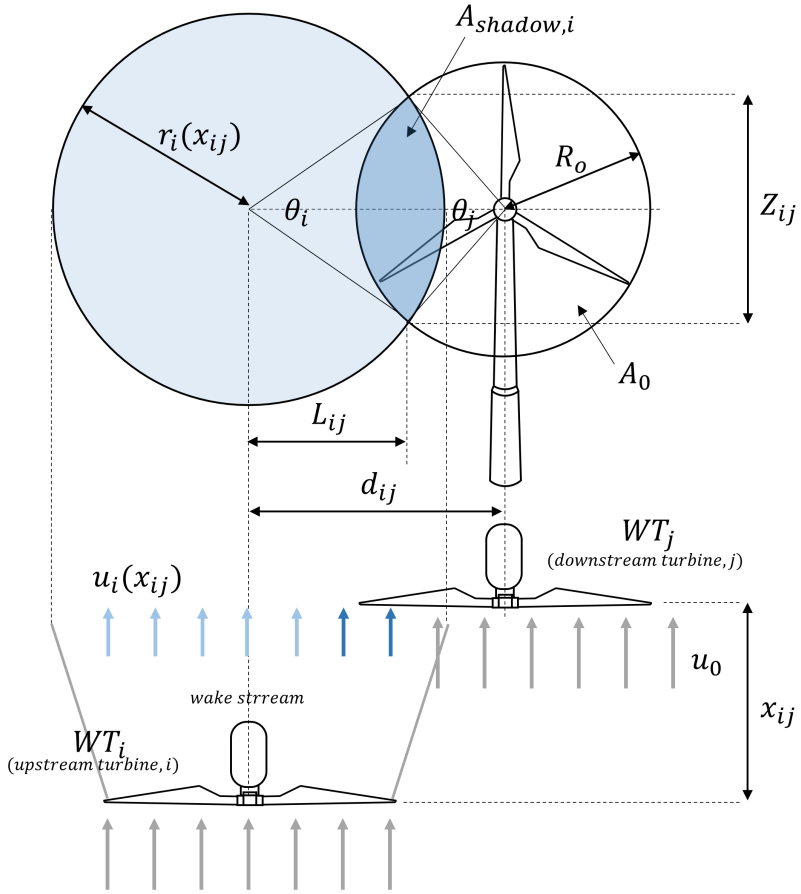

Figure 3-4: The model of the partial shadowing from a upstream turbine (adopted and modified from [50]).

$$A_{\mathrm{shadow},i} = [r_i(x_{ij})]^2 \, cos^{-1}\left(\frac{L_{ij}}{r_i(x_{ij})}\right) + R_0^2 \, cos^{-1}\left(\frac{d_{ij} - L_{ij}}{r_i(x_{ij})}\right) - d_{ij} z_{ij} \tag{3-6}$$

$$u_j(x_{ij}) = u_i \left[1 - \sum_{i=1}^{n} (1 - \sqrt{1 - C_T}) \left(\frac{r_0}{R_i(x_{ij})}\right)^2 \frac{A_{\mathrm{shadow},i}}{A_0}\right] \tag{3-7}$$

3-1-3 Remarks

The Jensen's wake model is simply derived from the mass and the momentum conservation of the flow, and is able to predict the wind deficit profile in the wake well without solving the fluid dynamics equations. Due to its simplicity and computational efficiency, it is widely adopted in commercial software, such as FLORIS [54], WAsP [55], WindFarmer [56], windPRO [57], to estimate the annual energy production of the wind farm during the early design phase. An example of a wind-farm-layout optimization conducted by Jensen's wake model is shown in Figure 3-5

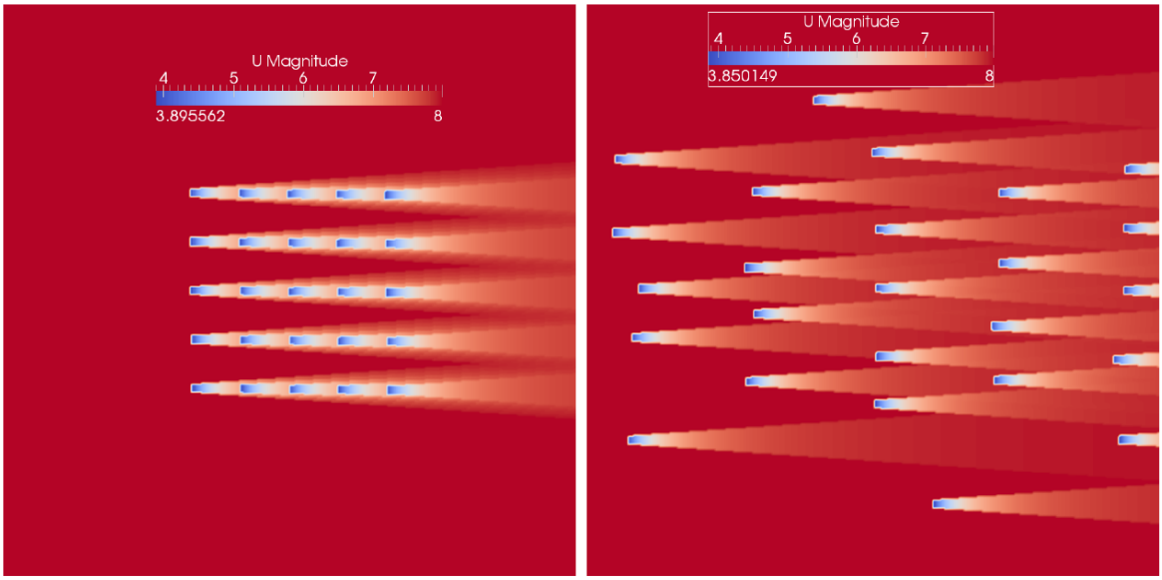

Figure 3-5: An example of wind-farm-layout optimization using the Jensen's wake model (adopted from [58]). After optimization (from left to right), the efficiency of the wind farm increases by 40%.

However, the Jensen's wake model is a steady-state model without considering the dynamics that significantly dominates in the wake. Therefore, the change of the turbulence level along the downstream distance can not be reflected by this model. Moreover, the model also ignores the vortex structures in the near wake region, which is previously shown to be an important wake characteristic in Figure 1-2, and this makes the velocity prediction in the near wake is not effective and is only applicable for the far wake, approximately 3-5 rotor diameter downstream (D) for onshore and 6-8 D for offshore [59]. In order to gain the insights on the wake dynamics for the purposes such as developing wake-mixing strategies, the turbulence models that solve the Navier-Stokes equations are required. These models are introduced in the next section, which can either be incorporated in the Jensen's wake model or be a stand-alone solver.

3-2 Turbulence model

The wake is a turbulent flow composed of vortical structures with different length scales as shown in Figure 3-6. The largest-scale structures, which contain most of the kinetic energy of the flow, break down into smaller-scale structures due to the vicious interaction between the structures, and their energy is also transferred and dissipated into smaller scales. These vortical structures are continuously moving and interacting with each other, which makes the motion of the turbulent flow unsteady, chaotic and difficult to predict. Universally, the phenomenon of turbulence is studied by solving the incompressible Navier-Stokes equations, a set of partial differential equations in the time and the space domain based on the mass, the momentum and the energy conservation. The equations expressed in index notation and in Cartesian coordinate are shown in Eq. (3-8) and Eq. (3-9), where u is the velocity, x is the space position, ρ is the mass density, P is the pressure, ν is the kinetic viscosity, i and j is are the directional components, S_{ij} is the strain rate tensor defined by $S_{ij} = 0.5(\partial u_i/\partial x_j + \partial u_j/\partial x_i)$, and F_i is the external body force.

$$\frac{\partial u_i}{\partial t} + u_j \frac{\partial u_i}{\partial x_j} = -\frac{1}{\rho}\frac{\partial P}{\partial x_i} + \frac{\partial}{\partial x_j}(2\nu S_{ij}) + \frac{F_i}{\rho} \tag{3-8}$$

$$\frac{du_j}{du_j} = 0 \tag{3-9}$$

Due to the nonlinear terms, $u_j \frac{\partial u_i}{x_j}$, there has not yet been any smooth and globally defined solution to the Navier-Stokes equations, which makes it one of the unsolved math problems in 21^{st} Century. Instead of being solved analytically, these equations have to be solved in a numerical way to obtain the approximate solutions by using the computational fluid dynamic (CFD) modeling approach. In the CFD modeling, the fluid dynamics equations are reformulated into the discrete form in a way that they can be solved iteratively by computers. Based on different modeling assumptions and simplifications made on the Navier-Stokes equations, the CFD modeling can be classified into the hierarchy with different computational costs as shown in Figure 3-7, which are elaborated in the subsequent sections.

3-2-1 DNS

The most accurate way of solving the Navier-Stokes equations from the aspect of CFD modeling is to solve them without any modeling assumptions. By doing so, all the relevant turbulent structures, from the largest to the smallest scales, are directly solved, and this approach is also called direct numerical simulation (DNS). The approach requires sufficiently fine mesh resolution and time steps to achieve accurate results, in which the size of mesh and time steps is approximately proportional to the cube of the Reynolds number (Re) [62]. Therefore, this makes the usage of DNS limited to studying the few cases of low Re and simple geometry, and DNS are exclusively used both in the academia and the industries. For example, to simulate the turbulent flow with Re in the scale of 10^3, it already requires approximately 10^{11} degrees of freedom [63] to be calculated. As for the wind flows in the atmospheric boundary layer

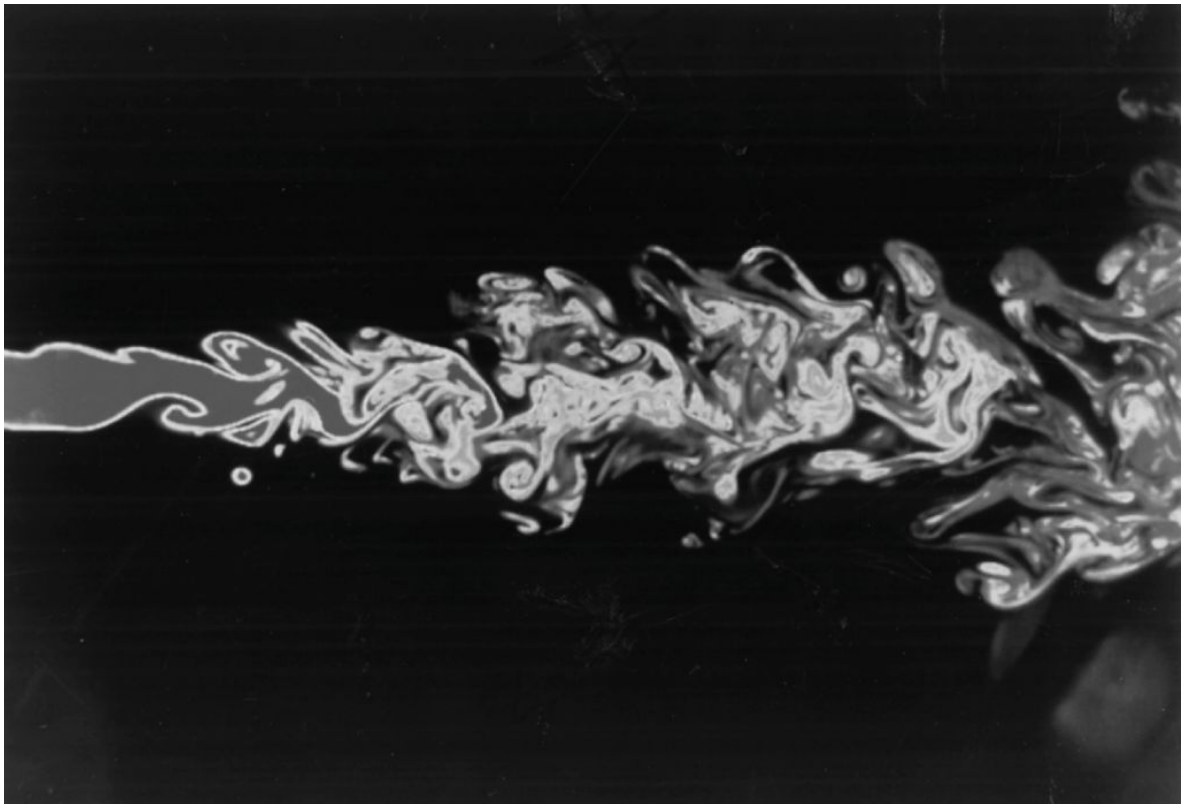

Figure 3-6: Two-dimensional image of a turbulent flow, obtained by the laser-induced fluorescence technique (adopted from [60]). Vortical structures with wide range of length scales exist in the turbulent flow.

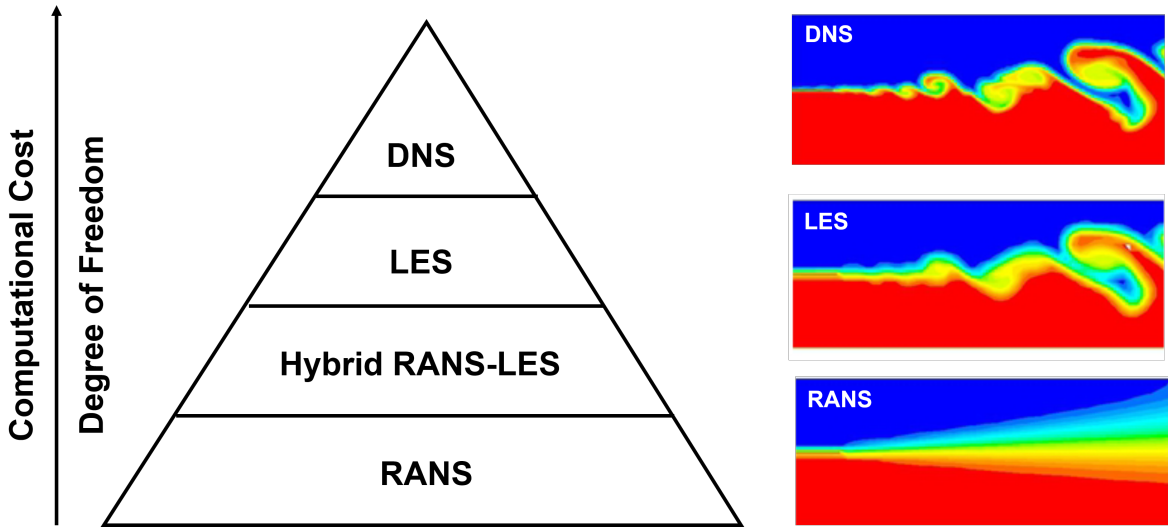

Figure 3-7: The hierarchy of the CFD modeling (left) and the examples of simulating a turbulent flow by DNS, LES and RANS (right) [61]. The higher the hierarchy, the more degree of freedom are calculated, which means smaller vortical structures are simulated, but also more computational cost is required. In the field of wake simulation, RANS and Hybrid RANS-LES are widely used in the full-scale wind farm level, LES is generally used in the smaller-scale wind farm or the turbine level, while DNS is hardly used for the studies of wind turbine wake due to its extremely high computational requirements.

(ABL), which is the environment the wind turbines are operating in, Re is in the scale of 10^8 [64], meaning that 10^{36} degrees of freedom are required to be calculated according to the cubic relationship as mentioned, and this computational cost makes DNS an impractical way in the wake simulation.

3-2-2 RANS

Instead of directly solving the instantaneous Navier-Stokes equations, Reynoalds-averaged Navier-Stokes equations (RANS) approach decomposes the equations into the steady-state terms plus the unsteady terms, in which the steady-state terms are solved numerically while the unsteady terms are modeled empirically. By doing so, the computational cost is substantially reduced. To achieve the RANS approach, the Reynolds decomposition is implemented , where the instantaneous velocity, u_i, is split into the average term, $\bar{u_i}$, and the fluctuating term, u_i', as expressed by Eq. (3-10). By substituting Eq. (3-10) into the Navier-Stokes equations and taking the time-weighted average on the equations, the RANS equations are re-expressed by Eq. (3-11), where $\bar{S_{ij}}$ is the average strain rate tensor defined by $S_{ij} = \frac{1}{2}(\frac{\partial \bar{u_i}}{\partial x_j} + \frac{\partial \bar{u_j}}{\partial x_i})$.

$$u_i = \bar{u_i} + u_i' \tag{3-10}$$

$$\frac{\partial \bar{u_i}}{\partial t} + \bar{u_j}\frac{\partial \bar{u_i}}{\partial x_j} = -\frac{1}{\rho}\frac{\partial \bar{P}}{\partial x_i} + \frac{\partial}{\partial x_j}(2\nu \bar{S_{ij}}) + \frac{\bar{F_i}}{\rho} - \frac{\partial(\overline{u_i' u_j'})}{\partial x_j} \tag{3-11}$$

The instantaneous Navier-Stokes equations are now decomposed into the linear terms plus the nonlinear terms, $-\frac{\partial(\overline{u_i' u_j'})}{\partial x_j}$, where the former can be solved analytically and the latter can be solved empirically. It is noted that the nonlinear terms correspond to the Reynolds stress, τ_{ij}', as defined by Eq. (3-12), which are the average momentum transfer caused by the turbulence. In other words, solving these Reynolds stress equations provides the insights on the turbulence.

$$\tau_{ij}' \equiv \rho(\overline{u_i' u_j'}) \tag{3-12}$$

However, the nonlinear terms representing turbulence are complicated, which require six additional unknown variables to be solved [45]. Therefore, in the RANS approach, there are branches of models using different assumptions and simplifications to relax these terms in order to closure the turbulence equations. These turbulence models based on the empirical observations are widely developed, which include adopting Prandtl's mixing length theory [65], eddy-viscosity closure [66], [67], $k-\epsilon$ closure [68], and dynamic wake meandering model [69], [70]. The RANS approach substantially reduces the computational cost, and it has been widely applied in the industrial CFD applications for the past decades [71]. However, by the RANS approach, only the averaged quantities of the flow are directly solved, while all the instantaneous turbulent motions are modeled empirically, which limits the knowledge on the transient behaviour of the flow when it is of interest.

3-2-3 LES

The large-eddy simulation (LES) is the high-fidelity CFD modeling directly solving the Navier-Stokes equations where the smaller scales of eddies are filtered out in advance. A low-pass spatial filter of a certain grid size, Δx, is applied to the velocity field, u, in the flow. By doing so, the eddies of scales smaller than Δx are filtered out, resulting in the filtered velocity field, $\tilde{u}$, as shown in Figure 3-8. The subgrid-scale velocity is described by the difference between the actual and the filtered velocity.

Applying the filtered velocity to the Navier-Stokes equations, Eq. (3-13) can eventually be derived, where $\tilde{S_{ij}}$ is the filtered scale strain rate tensor defined by $\tilde{S_{ij}} = 0.5(\partial\tilde{u_i}/\partial x_j + \partial\tilde{u_j}/\partial x_i)$, and T_{ij} is the stress tensor caused by the subgrid-scale turbulence defined by Eq. (3-14).

$$\frac{\partial\tilde{u_i}}{\partial t} + \frac{\partial}{\partial x_j}(\tilde{u_i}\tilde{u_j}) = -\frac{1}{\rho}\frac{\partial\tilde{P}}{\partial x_i} + \frac{\partial}{\partial x_j}(2\nu\tilde{S_{ij}}) + \frac{\tilde{F_i}}{\rho} + \frac{\partial T_{ij}}{\partial x_j} \tag{3-13}$$

$$T_{ij} = \tilde{u_i}\tilde{u_j} - \tilde{u_i u_j} \tag{3-14}$$

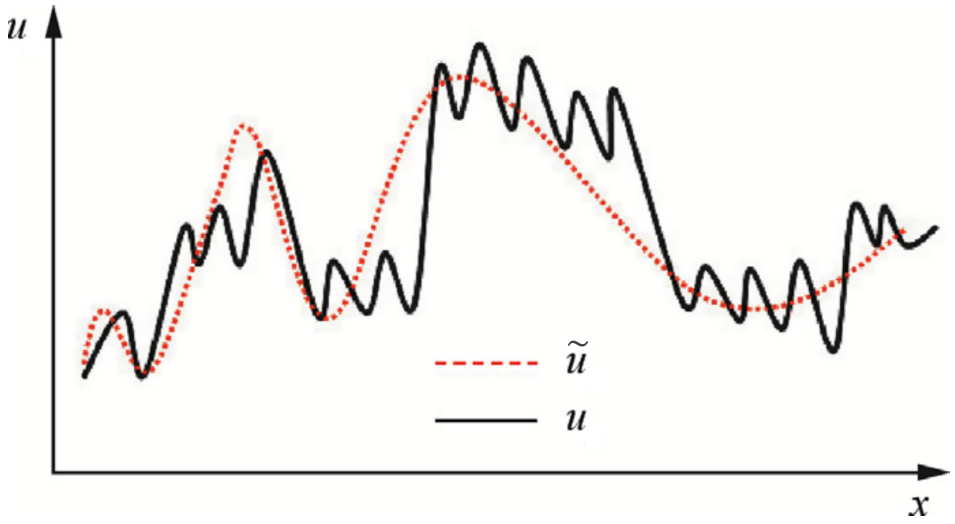

Figure 3-8: Difference between the filtered velocity and the actual velocity (adopted and modified from [71]). $\tilde{u}$ is the filtered velocity and u is the actual velocity. The subgrid-scale velocity is the difference between the actual and the filtered velocity.

By doing so, the Navier-Stokes equations are decomposed into the large and the small scales. For the large-scale motions of the fluid, they are computed directly, while for the subgrid-scale motions of the fluid, they are modeled empirically, which substantially reduces the computational time compared with the DNS. Since the LES method captures the details of the large eddies which contain most of the turbulent energy and involves in most of the momentum-transfer processes, it has capability to simulate the complex and the transient turbulent flows which can not be done by the RANS approach. Moreover, the turbulence of small scales is more isotropic and homogeneous, making its simulation models easier than the ones of the RANS which contain all the scales. However, the LES also requires the computational cost approximately three orders of magnitude more than the ones of the RANS [47].

3-2-4 Remarks

The turbulence characteristics of the wake, which can not be predicted by the Jensen's wake model, are simulated by the CFD modeling, where the Navier-Stokes equations are numerically solved. Based on the assumptions and the simplifications made to solve these equations, the CFD models can be categorized into different fidelity.

In the most accurate model, DNS, the fluid-dynamics equations are fully solved, but this method has not be adopted in the field of wind-turbine-wake simulation due to its extremely high computational cost.

In the low-fidelity CFD model, RANS, the steady-state terms of the flow are directly solved, while the turbulent terms are modeled empirically. Without directly solving the nonlinear turbulence terms of the Navier-Stokes equations, the RANS significantly saves the computational cost and makes it a widely used wake model in the wind farm level. There has be

numerous commercial RANS-based software, such as WAsP [55], OpenWind [72], WindSim [73], Fast.Farm [74] and EllipSys3D [75]. Since the RANS method simulates the turbulence in an empirical way, the detailed behaviors of these turbulent eddies are ignored. Therefore, the higher-fidelity CFD model with a modest computational cost is required when these dynamic details of turbulence are desirably to be understood.

In the high-fidelity CFD model, LES, all the turbulence of large scales are directly computed, while the small scales are filtered out and are modeled in an empirical way. By doing so, the computational cost is significantly reduced compared with using the DNS, and the turbulence details are maintained at the same time, with an example shown in Figure 3-9. There are several commercial LES-based software available, such as SOWFA [76], LESGO [77], SP-Wind [78] and EllipSys3D [75].

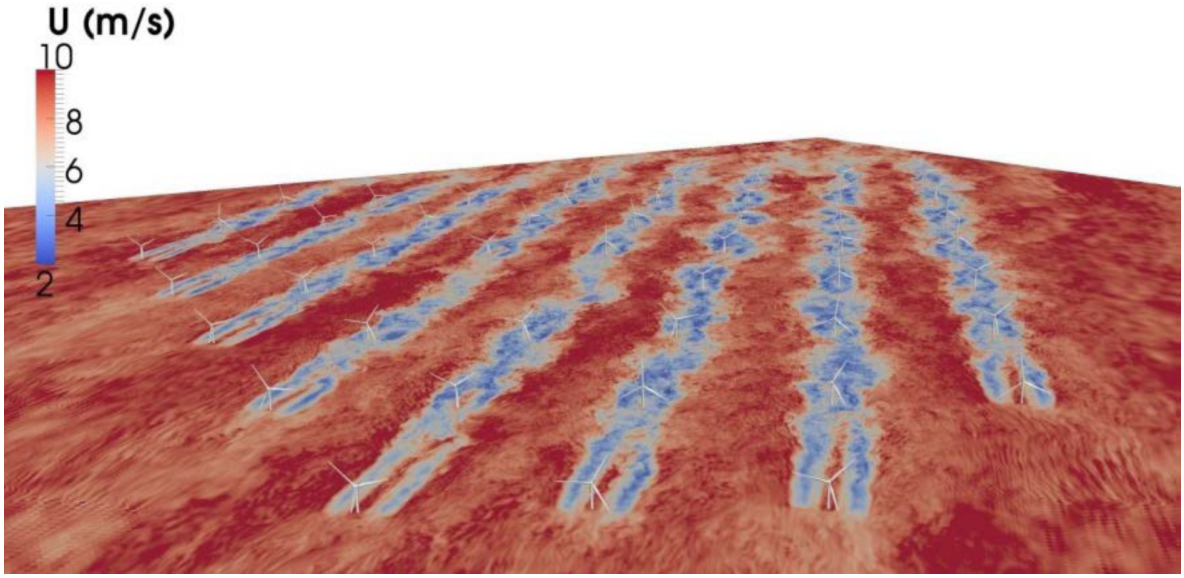

Figure 3-9: An example of the wake simulation done by the LES method (adopted from [74]). The figure is obtained by the software SOWFA, where the turbulence details are simulated.

3-3 Free vortex wake model

3-3-1 Introduction

In the aforementioned CFD modeling (e.g. DES, RANS and LES), the Eulerian approach is adopted, which means the whole space domain is discretized into the grids, and the fluid motions within all the grids are simulated. These grids need to be fine enough to prevent the excessive numerical dissipation error, and the requirement of the grids leads to the high computational cost that is unfavourable for designers who aim to have faster feedback for parametric or optimization studies [79], [80]. Therefore, the free vortex wake (FVW) model, a CFD model adopting the grid-free Lagrangian approach becomes of great interest. Instead

of discretizing the space domain into the grids, the Lagrangian approach discretizes the fluid into individual parcels where their movements are simulated (the comparison with the Eulerian approach can be seen in Figure 3-10). By doing so, the dynamic details of the fluid can still be simulated accurately, and it can be achieved at a lower computational cost than using the Eulerian-based CFD models [81], [82].

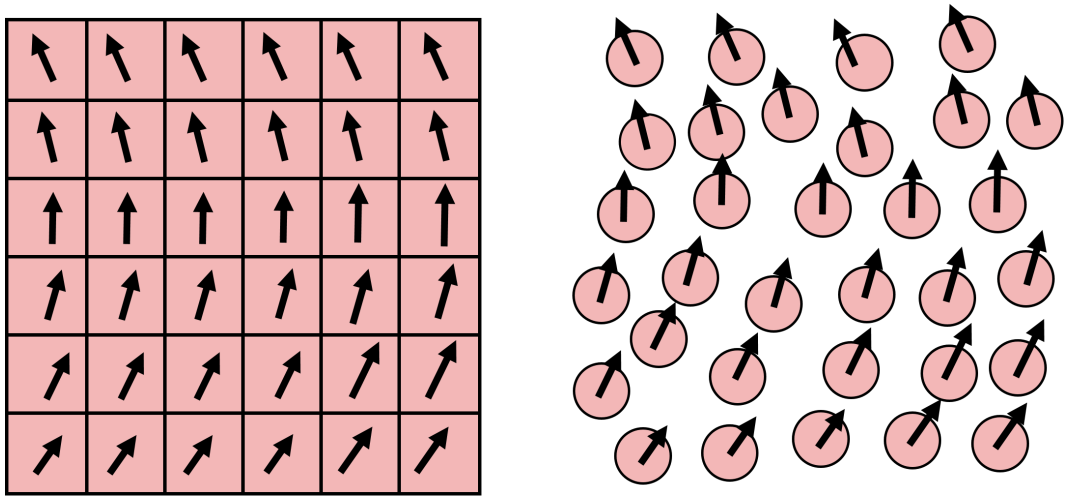

Figure 3-10: The comparison between the Eulerian (left) and Lagrangian (right) approach used in the CFD modeling. In the Eulerian approach, the space domain is discretized into grids where the fluid motions are simulated within all the grids. In the Lagrangian approach, the fluid is discretized into fluid parcels, in which there movements are individually simulated.

The FVW model is widely applied in the field of the helicopter since it is capable of simulating the vortical structures in the near wake region, where these vortices have strong interactions with the rotor [80]. During the past decade, the FVW model has also been adopted in the field of the wind turbine. The main application of the FVW model is to simulate the rotor-wake interactions. For example, the dynamic turbine-wake interactions between multiple turbines are captured [83], the interactions between rotors in a multi-rotor wind turbine are modeled [84], and the aerodynamic performance of a floating wind turbine in a surge motion is analyzed [85]. The FVW model is also exploited to replace the blade element momentum (BEM) method to predict the aerodynamic loads on the wind turbine with highly flexible blades where the assumptions of the BEM method are violated [83] and [86]. Another main application of the FVW model is to simulate the wake evolution. For example, the stability of the tip vortical structure is analyzed and the prediction of the wake breakdown is done in the studies [87], [88] and [79].

3-3-2 Theory

The implementation of the FVW model is generally based on two submodels, lifting-surface representation and wake-vortex representation, which are explained in the following.

Lifting-surface representation

The lifting-surface representation refers to the modeling of the bound vortices formed on the surface of the blades due to the lift force, and these continuously distributed vortices are described in the discrete form either by the lifting-line method or by the vortex-lattice method, as shown in Figure 3-11. In the lifting-line method, the bound vortices are simply represented by the lifting line of varying circulation along the spanwise direction. The simplification saves the computational cost, but this method is not able to capture the three-dimensional effects of the flow on the rotor blade. On the other hand, in the vortex-lattice method, the bound vortices are represented by circulation distributed on the lattices of the blade both in the chordwise and the spanwise direction. By doing so, the details of the three-dimensional behavior of the flow on the blade can be simulated, but it also requires more computational expense.

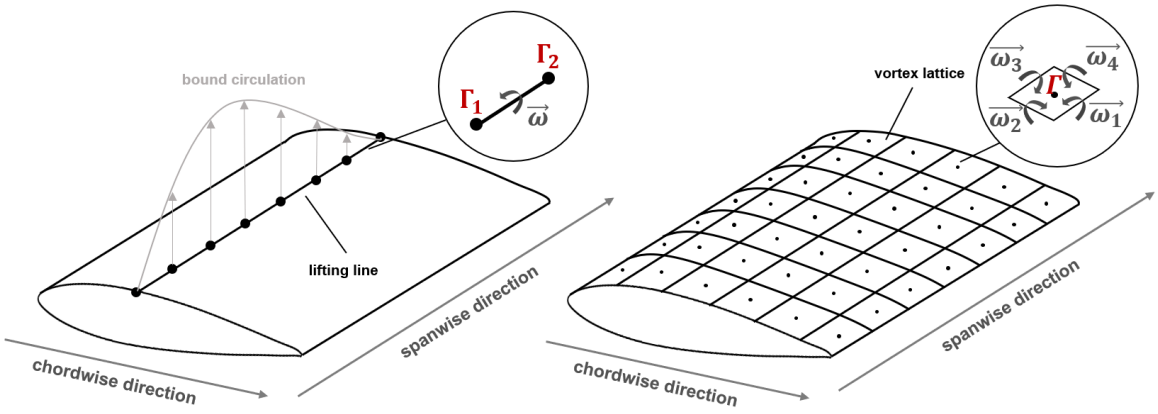

Figure 3-11: The schematic of two methods used for lifting-surface representation (adopted and modified from [80]). The lifting-line method (left) describes the bound circulation distribution on the lifting line in the form of so-called vortex filaments. A vortex filament is delimited by two endpoints individually representing its circulation, Γ_1 and Γ_2, and these these two points form the vorticity vector, $\vec{\omega}$. The vortex-lattice method (right) describes the circulation distribution on the vortex lattices in the form of vortex rings. A vortex ring represents the circulation, Γ, surrounded by four vortex filaments of different vorticity vector, $\vec{\omega_1}$, $\vec{\omega_2}$, $\vec{\omega_3}$ and $\vec{\omega_4}$.

Consider the case of the lifting-line representation, the bound circulation distribution can be determined by the C_l-based iterative method. This algorithm ensures the lift force obtained by using the lift coefficient (expressed in Eq. (3-15)) is the same as the lift force obtained by the Kutta-Joukowski theorem (expressed in Eq. (3-16)), where dL is the incremental lift force, ρ is the mass density of the fluid, U is the local velocity, C_l is the lift coefficient, α is the angle of attack, c is the local chord length, dr is the incremental spanwise length, and Γ is the circulation.

$$dL = \frac{1}{2}\rho U^2 C_l(\alpha) c dr \tag{3-15}$$

$$dL = \rho U \Gamma dr \tag{3-16}$$

Wake-vortex representation

The wake-vortex representation refers to the modeling of the vortices in the wake which are previously shed from the trailing edge of the rotor blades. The movement of these vortices is described by the vorticity transport equation in Eq. (3-17), which is derived from the Navier-Stokes equations assuming the flow to be incompressible and isotropic, where ω is the vorticity, u is the velocity, ∇ is the vector differential operator, ν is the kinetic viscosity, and ∇^2 is the Laplace operator.

$$\frac{\partial \omega}{\partial t} + (u \cdot \nabla)\omega = (\omega \cdot \nabla)u + \nu \nabla^2 \omega \tag{3-17}$$

The equation is composed of the vorticity and the velocity vectors, making it a convenient form for the Lagrangian approach. That is, the vorticity field can be discretized and treated as the vortex elements which are freely convecting in the velocity field. By tracking the movement of these vortex elements, the dynamics of the wake can be depicted. On the left-hand side of the equation, there are the time-derivative term and the space-derivative term, which overall describes the vorticity field in the temporal and spatial domains. The time-derivative term, $\partial\omega/\partial t$, represents the unsteadiness of the vortices, and the space-derivative term, $(u \cdot \nabla)\omega$, represents the spatial movements of these vortices caused by the gradient of the vorticity, also know as the effect of convection. The first term on the right-hand side of the equation, $(\omega \cdot \nabla)u$, represents the vortex-stretching effect caused by the gradient of the velocity, and the second term, $\nu\nabla^2\omega$, represents the vorticity diffusion caused by the viscous effects.

It is noted that the movement of the vortex element is driven by the local convection velocity, which is the sum of the free-stream velocity and the wake-induced velocity. The wake-induced velocity is contributed by all the other vortex elements, where each element creates its own velocity field. Therefore, the location of these vortex elements can be expressed by Eq. (3-18) and Eq. (3-19), where $\vec{r}$ is the location vector of the vortex element, $\vec{u}$ is the local convection velocity, $\vec{u_0}$ is the free-stream velocity, and $\vec{u_k}$ is velocity contributed the k^{th} vortex element, and N is the total number of the vortex elements.

$$\frac{d\vec{r}}{dt} = \vec{u}(\vec{r}, t) \tag{3-18}$$

$$\vec{u} = \vec{u_0} + \sum_{k=1}^{N} \vec{u_k} \tag{3-19}$$

The vortex element can be represented either by the vortex filament or the by vortex particle, which leads to the different approaches of calculating the wake-induced velocity. Consider the case of the vortex-filament representation, where the k^{th} vortex filament is shown in Figure 3-12. The velocity field created by this vortex filament on a given location can be estimated

by using the Biot-Savart law in Eq. (3-20), where $\vec{r_1}$ and $\vec{r_2}$ are the location vectors from the endpoints to the given location, Γ is the circulation strength of the vortex filament, and F_v is the smooth function.

$$\vec{u_k} = F_v \frac{\Gamma}{4\pi} \frac{(|\vec{r_1}| + |\vec{r_2}|)}{|\vec{r_1}||\vec{r_2}|(|\vec{r_1}||\vec{r_2}| + \vec{r_1}\vec{r_2})} \vec{r_1} \times \vec{r_2} \tag{3-20}$$

The Biot-Savart law describes the inverse-square relation between the strength of the field and the distance to source of the field, and this leads to the extremely large velocity field happened close to the vortex core, as shown in Figure 3-13. This is the inherent issue called singularity for the Lagrangian approach to solve the vorticity transport equation. To prevent the singularity, the smooth function., F_v, is required to regularize both the vorticity and the velocity field as compared to the real continuous vorticity field. It is noted that in some software implementation, the viscous diffusion effect is already considered in this regularization process since the vortex is treated as a "viscous core", and it prevents solving the diffusion term in the vorticity transport equation [83].

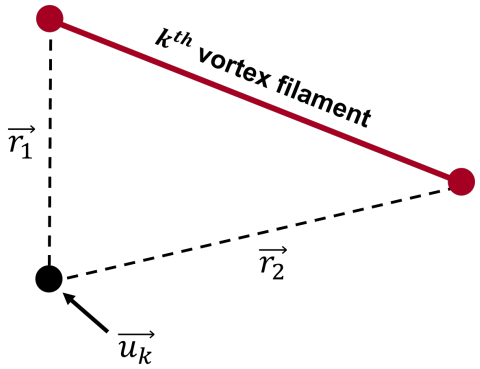

Figure 3-12: The schematic of the k^{th} vortex filament and its induced velocity, $\vec{u_k}$, on the given location. The relative distance between the given location and the vortex filament can be described by vectors, $\vec{r_1}$ and $\vec{r_2}$.

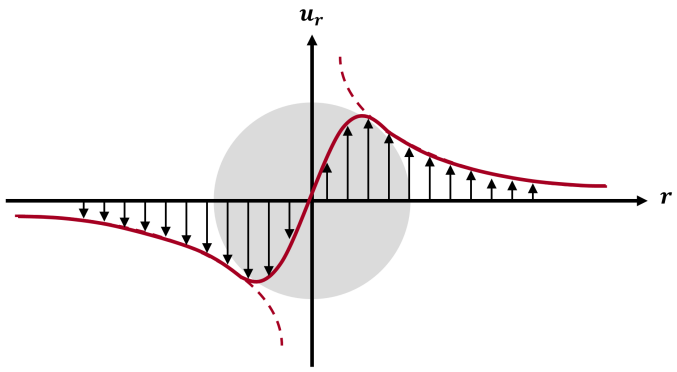

Figure 3-13: Velocity field induced by the vortex core (adopted and modified from [89]). The dashed line is the velocity field described by the Biot-Savart law, and the solid line is the smoothed vorticity field by implementing the smooth function.

Overview

Figure 3-14 shows the overview of the FVW method based on the lifting-line and the vortex-filament representation, which is the widely used FVW model in the studies of wind turbine wakes [79]. At the first time step, the bound circulation on the lifting line is calculated based on the polar data and the angle of attack at each spanwise position. At the next time step, the new bound circulation distribution is updated, and the previous one is passed to the trailng edge of the blade. To satisfy the Kutta condition, the circulation of the first emitted vortices, which are on the trailing edge of the blade, should be equal to the bound circulation. This condition connects the wake-vortex simulation to the lifting-surface simulation. After the vortices are shed from the blade, they are allowed to move freely in the wake, and their circulation would remain constant based on the Helmholtz's theorem. These free vortices are treated as Lagrangian markers, which are connected together into a sheet of vortex filaments. The vortex filaments can be translated into the trailing vortices and the shed vortices, in which the former are caused by difference between the bound circulation and the latter are caused by the azimuthal change of the bound vortices with time. Due to the interaction between the vortices, these vortices would concentrate and roll up into the tip and the root vorticies as they propagate downstream. As mentioned previously in Figure 1-2, the tip vortical structure prevents the wake-mixing process and is considered an important characteristic to be studied to develop the wake-mixing control strategies.

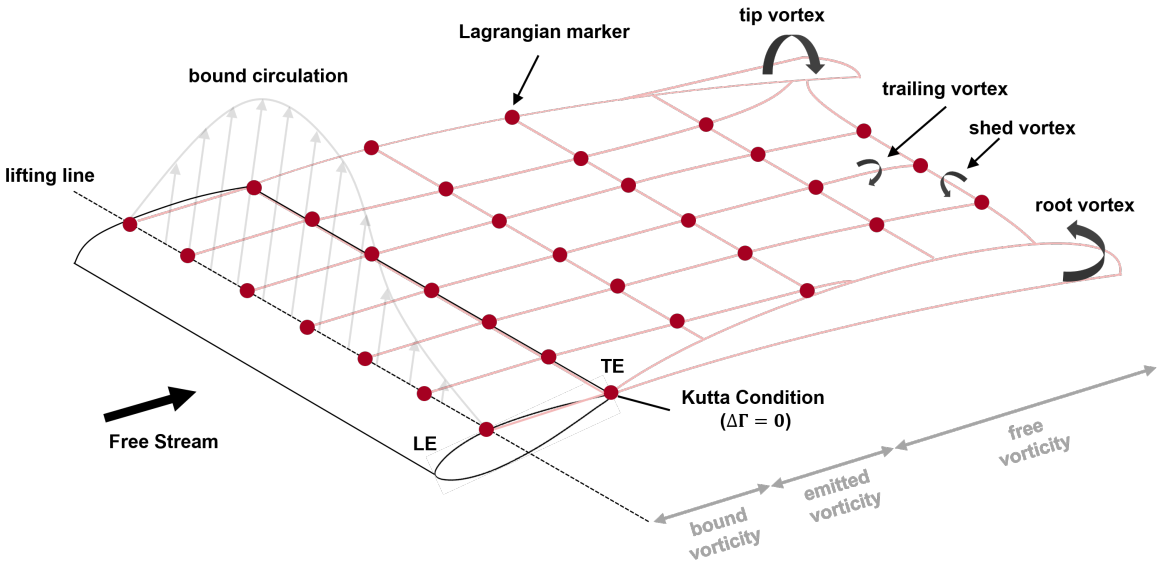

Figure 3-14: The overview of the FVW model based on the lifting-line and the vortex-filament representation (adopted and modified from [80]). It is the widely used FVW model in the studies of wind turbine wakes.

3-3-3 Remarks

Compared with the Eulerian-based CFD modeling such as RANS and LES, the Lagrangian-based CFD modeling, FVW model, is able to capture the dynamic details of the wake at a lower computational cost due to its grid-free characteristic. Therefore, it has become an attractive approach for designers to achieve faster feedback, which is preferred in the parametric or the optimization studies, and the FVW model has been integrated into several wind turbine simulation software, such as QBlade [90] and OpenFAST [91].

The FVW model is widely applied in the field of the helicopter, and during the past decade, it has also been adopted in the field of wind turbine, including the investigation of the rotor-wake interactions and the wake development. Among the wake-development studies, the FVW model is mostly utilized to study the stability of the tip-vortical structure in the near wake region, which is an important issue to develop the wake-mixing control strategies. However, here are two main challenges for the FVW model: numerical instability and far-wake field prediction, which are explained in the following.

Numerical instability

The numerical instability of the FVW model occurs by two sources. Firstly, to solve the position of the vortex element, which is the left-hand side of Eq. (3-18), the time-marching method is used to integrate the time numerically. However, using different orders of integration methods can cause different extent of the numerical errors. Secondly, the FVW model requires the smooth function to regularize the discrete vorticity and velocity fields, which is expressed as F_v in Eq. (3-20). The smooth function is an empirical formulation, and the values of its parameters are normally determined experimentally [80]. Therefore, the inap-

propriate smooth function and its parameters can add the numerical instability into the model.

The numerical instability can affect the accuracy of the FVW results, making it a challenge for researcher to differentiate the nonphysical disturbance from the real physical instability which is of interest [80] and [88].

Far-wake field prediction
The vortex-filament representation is adopted in most of the studies due to its lower computational cost than vortex-particle representation, as introduced in Section 3-3-2. However, the FVW model based on the vortex-filament representation is not appropriate to simulate the turbulent mixing, which happens in the far wake region after the wake breaks down. It is because the vortex filament constrains each vortex to be connected to the one from the previous time step and the adjacent ones, and this leads to the three dimensional distortion of the vortex sheet when the wake starts mixing, as demonstrated in Figure 3-15. Therefore, the velocity field in the far wake region predicted by the vortex-filament FVW model is not representative, and it is an artifact of the simulation instead [79].

The vortex-particle representation treats the vortices individually without the connectivity requirements, and this implementation overcomes the incapability of the vortex-filament representation to predict the far-wake velocity field. However, the self-induced velocity from the vortex elements should be calculated twice when the connectivity is loosed, and it can cause the computational cost four times larger in this N-body simulation problem [79]. To improve the computational efficiency of the vortex-particle FVW model, some fast summing algorithms are being developed, such as the Tree-Code approach and the multipole method [80]. Moreover, converting from the filament method to the particle method after the wake breakdown is also considered a practical implementation.

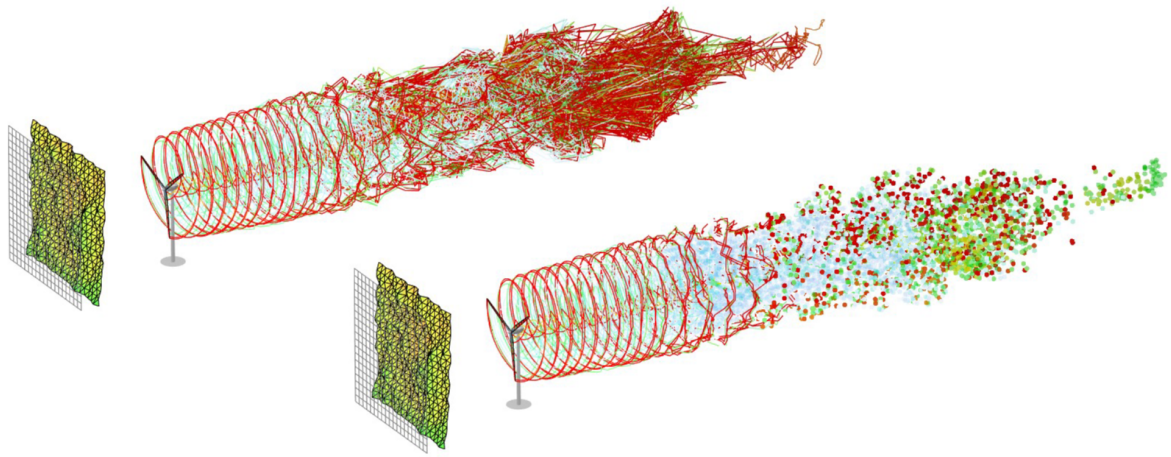

Figure 3-15: The FVW simulation based on the vortex-filament representation (left) and the vortex-particle representation (right) (adopted from [79]). In the vortex-filament representation, the vortex sheet distorts when the wake starts mixing because the vortex elements need to remain connected to their adjacent ones. In the vortex-particle representation, the vortices are treated individually without connectivity requirements, so the velocity field in the mixing range can be predicted more accurately.

3-4 Closing Remarks

In this chapter, the wake models from the low to the high fidelity are introduced. The most widely used low-fidelity model is the Jensen's wake model, which is based on the steady-state mass and momentum conservation. Although the model is computational efficiency, it is unable to simulate the vortical structures and the dynamics of the wake which are desired to be investigated in this study. Therefore, to gain the insights of the wake dynamics, the computational fluid dynamic (CFD) modeling which numerically solves the Navier-Stokes equations are considered. Direct numerical simulation (DNS) is the most accurate way to perform CFD modeling, but due to its extremely high computational cost, it is impractical to use DNS for the wind turbine wake simulation. The Reynoalds-averaged Navier-Stokes equations (RANS) is the low-fidelity CFD modeling which solves the average quantities of the flow and modeled the turbulent motions empirically. However, the empirical modeling of the turbulence limits the knowledge of the transient behaviour of the flow. The large-eddy simulation (LES) is the high-fidelity CFD modeling, which directly solves the eddies of large scales in the Navier-Stokes equations. However, adopting the LES for the wind turbine wake simulation requires the significant computational cost, and this limits the number of simulations.

The free vortex wake (FVW) model is the mid-fidelity CFD modeling, which solves the vorticity transport equation through the Lagrangian approach. The FVW model is capable of simulating the evolution of the vortical structures and the transient behaviour of the wake. Moreover, the computational cost of the FVW model is four to five orders of magnitude lower than the one of the LES [79]. Therefore, the FVW model is used in this study to investigate the impacts of blade actuation on the wake development. However, the numerical instability and the far wake prediction should be carefully considered when adopting the FVW model.

Chapter 4

Simulation Environment

The free vortex wake model is considered to be a promising CFD approach to capture the evolution of the vortical structures in the wake at a reasonable computational cost, and therefore is adopted in this study to explore the effectiveness of the Helix approach with different parametric settings. In this chapter, the simulation environment that is set up for the study is outlined. Section 4-1 presents the simulation models that are adopted, including the wind turbine model and the free vortex wake model. Section 4-2 presents the simulation setup, including the simulation cases, the input settings and the methods for data analysis.

4-1 Simulation models

4-1-1 OpenFAST

OpenFAST is a multidisciplinary model that simulates the coupled dynamic responses of the wind turbine, which is an open-source software package developed by National Renewable Energy Laboratory (NREL) [92]. The model is composed of different computational modules, including aerodynamics (*AeroDyn*), hydrodynamics for offshore structures (*HydroDyn*), control and electrical system dynamics (*ServoDyn*), and structural dynamics (*ElastoDyn*), as illustrated in Figure 4-1. The calculations of these modules are instantaneously passed between each other at each time step through the main driver, or called the glue code, which enables the dynamic nonlinear aero-hydro-servo-elastic simulation.

AeroDyn
The aerodynamic module, or called *AeroDyn* in OpenFAST, computes the aerodynamic loads on the blades and the tower based on the local flow conditions experienced by these components. The model receives the instantaneous information of the free-stream inflow wind and the structural responses to execute the calculations, and returns back the results to the main driver for another round of the aero-elastic simulation.

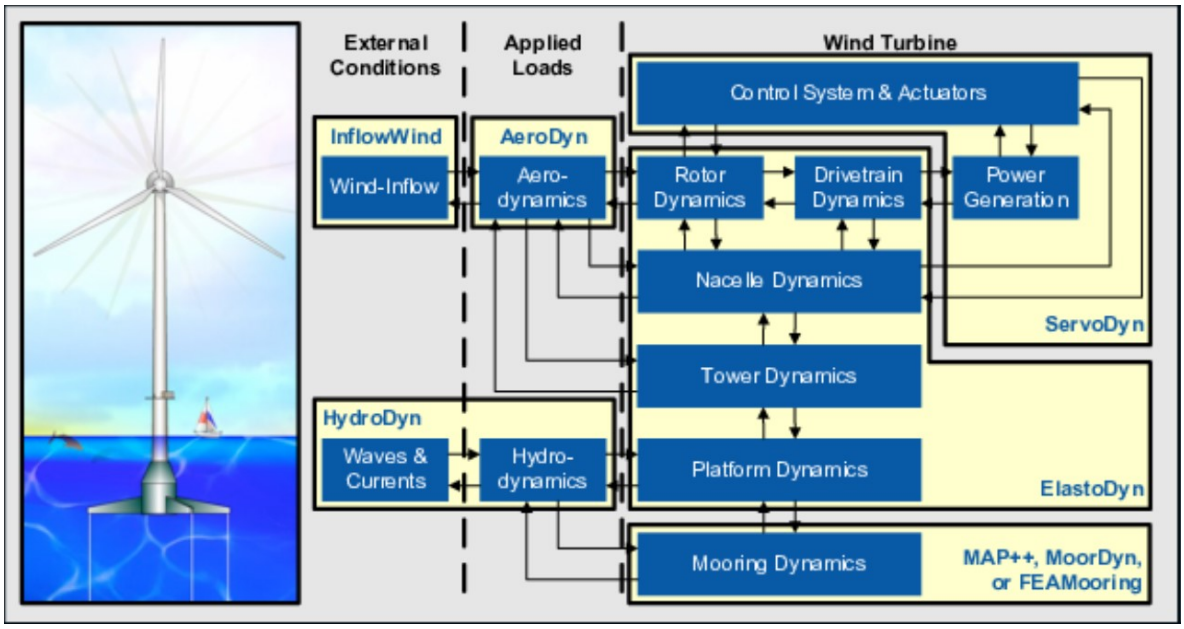

Figure 4-1: The framework of OpenFAST (adopted from [92]). There are several modules with different disciplines used to simulate the dynamic responses of the wind turbine, including *InflowWind*, *AeroDyn*, *HydroDyn*, *ServoDyn*, *ElastoDyn* and *MoorDyn*. The calculation results of each modules are instantaneously passed between each other, enabling the dynamic nonlinear aero-hydro-servo-elastic simulation.

The rotor is represented by the actuator lines, where the blades are discretized into several nodes in the spanwise direction. By treating blades individually, the asymmetric effects on the rotor, such as aerodynamic imbalance caused by the different contributions from blades, are able to be captured. The actuator-line representation is essential to the study of the Helix approach since the asymmetric pitching effects of the blades are of great interest. In a similar manner, the tower is also discretized into several nodes. Based on the node discretization, the aerodynamic properties, including the lift force and the drag force, are calculated and lumped at each node, and the overall aerodynamic-load distribution can be estimated by integrating the discretized aerodynamic loads. The other key parameters used to define the wind turbine configuration for the aerodynamic calculations are demonstrated in Figure 4-2, including airfoil geometry, airfoil polar data, shaft tilt angle, precone angle, the hub height, the overhang and the tower diameter.

The aerodynamic calculations in *AeroDyn* module are implemented by four submodules: (1) rotor wake, (2) blade airfoil aerodynamics, (3) tower shadow and (4) tower drag. In the rotor wake submodule, the influence of the wake on the blades are considered, either through the blade element momentum (BEM) method or the free vortex wake (FVW) method. In this study, the FVW method is adopted, which is elaborated in Section 4-1-2. In the blade airfoil aerodynamics submodule, the aerodynamic loads can be estimated by exploiting the airfoil polar data. The polar data describes the lift and the drag forces on the airfoil under different angle of attack (AoA). In the tower shadow submodule, the disturbance from the presence of the tower on the free-stream flow at each blade node is considered. In the tower drag

submodule, the drag loads on the tower are calculated based on the local wind speed, tower geometry and the drag coefficient.

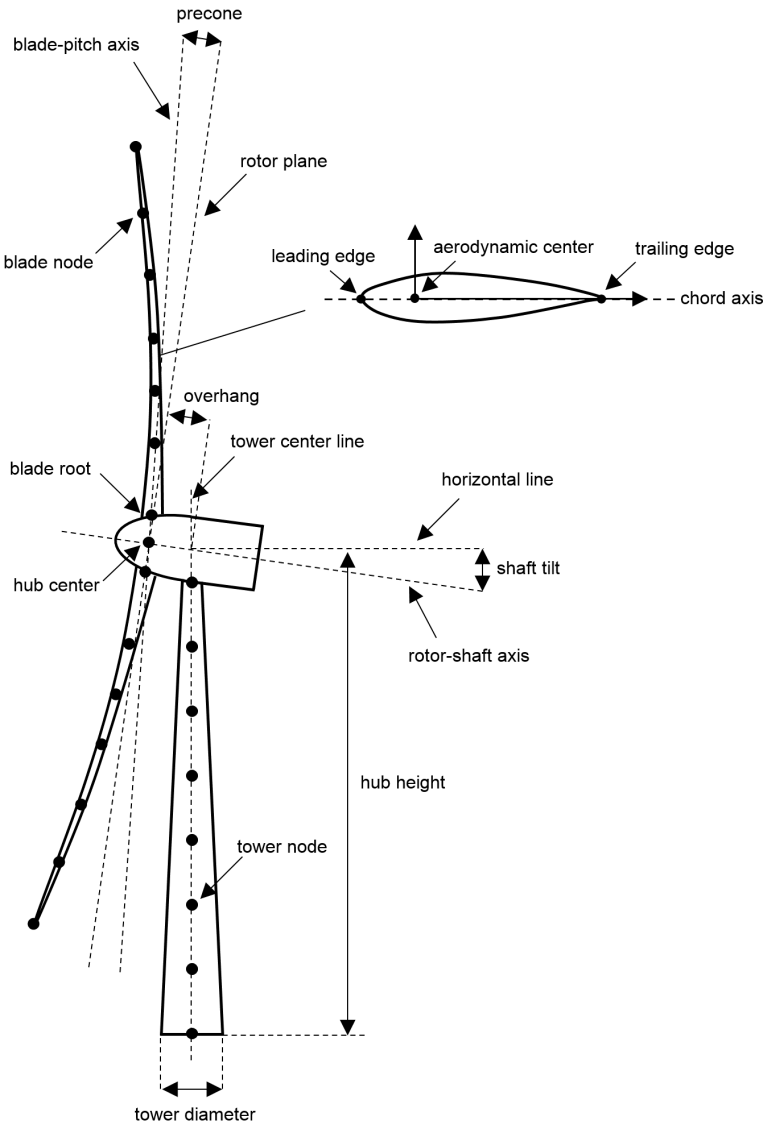

Figure 4-2: The key parameters used to define the turbine configuration (adopted and modified from [92]). Both the blades and the tower are represented by nodes, and other parameters include airfoil geometry, airfoil polar data, shaft tilt angle, precone angle, the hub height, the overhang and the tower diameter.

ServoDyn
The control and electrical system dynamics, or called *ServoDyn* in OpenFAST, simulates the dynamics of both the controllers and the other electrical devices in the drivetrain in response to dynamic mechanical and electrical loads. The key components in the module includes the controller algorithm, the wind-speed estimator, the generator torque, the nacelle-yaw control and the actuator demands on the blade pitch. It is noted that in *ServoDyn*, it is allowed for users to define the individual pitch activities, which is essential to the study of the Helix approach where the IPC technique is used.

4-1-2 OLAF

As mentioned in Section 4-1-1, in the aerodynamic module of OpenFAST, *AeroDyn*, there are two alternative methods used to simulate the rotor-wake interactions: the blade element momentum (BEM) method and the free vortex wake (FVW) method. The BEM method was introduced in the study [93], which coupled the local aerodynamic events on the blades with the macroscopic behavior of the fluid passing through the rotor, where the former exploited the two-dimensional airfoil information and the latter adopted the one-dimensional momentum theory based on the actuator disk model. The BEM method is widely applied to compute the aerodynamic loads on the blades of the wind turbine due to its computational efficiency and its robustness. Since the method is based on several engineering assumptions, it also relies on a number of correction models to consider the dynamic stall effects, the skewed wake due to yaw misalignment and shaft tilt, the tip losses and the ground effects to achieve more realistic prediction.

However, the engineering assumptions made in the BEM method are violated more significantly when the blade deflection increases , which occurs in the modern wind turbines with extremely larger and more flexible blades. Specifically speaking, due to the significant blade deflection, several complex wind turbine situations arise. For example, the swept area deviates from the rotor plane, the rotor aerodynamic forces become axially asymmetric, the local near-wake interaction with the rotor increases, unsteady and three-dimensional aerodynamic effects on the airfoils are induced. These complex situations can not be accurately simulated by the engineering correction models, and therefore require the CFD methods to be realistically captured.

The free vortex wake (FVW) method as discussed in Section 3-3 is adopted to simulate the complex rotor-wake interactions due to its relative lower computational cost than the other CFD models. In the current version of OpenFAST, both the BEM method and the FVW method are integrated in the aerodynamic module, *AeroDyn*, where the user can choose either one of them based on their purposes. Figure 4-3 shows that both the BEM method and FVW method are integrated in the aerodynamic module, *AeroDyn*, where users can choose either one of them based on their purposes. It is also noted that the FVW method used in OpenFAST is also referred as the convecting lagarangian filaments (OLAF) module.

Figure 4-4 demonstrates the key features of the OLAF module, which is elaborated in the fol-

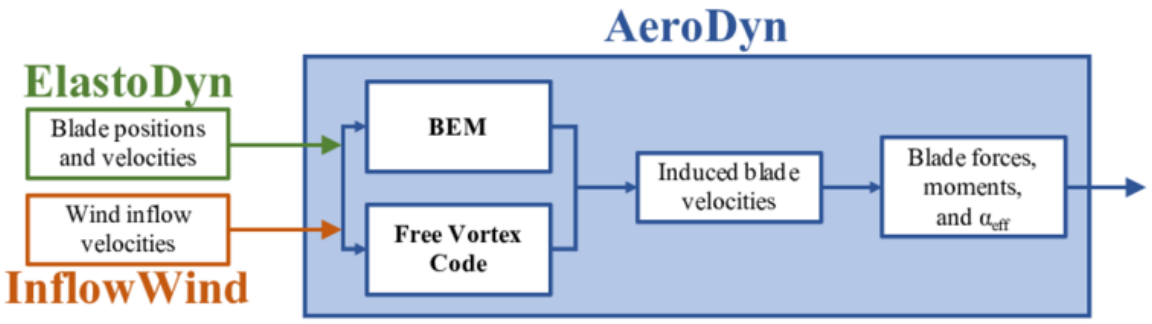

Figure 4-3: The BEM method and the FVW method are both integrated in the aerodynamic module, *AeroDyn*, where users can choose either one of them based on their purpose (adopted from [92]). Both the methods receive the information from the structural dynamics module, *ElastoDyn*, and the wind inflow module, *InflowWind*, to compute the aerodynamic loads on the blades.

lowing. To begin with, the OLAF module adopts the lifting-line representation to describe the bound vortices formed on the surface of the blades. These bound vortices are characterized as the circulation distribution lumped at the blade nodes defined in the spanwise direction. The circulation intensity is linked to the aerodynamic loads through the Kutta-Joukowski theorem, which can be estimated based on the airfoil polar data and the local flow conditions. These bound vortices are emitted into the wake and are allowed to convect freely in the downstream, where their positions are individually defined by the azimuth position, ψ, and the wake age, ζ.

These freely convecting vortices in the wake are initially represented by the vortex lattice and subsequently represented by the vortex filaments. In the vortex-lattice representation, the circulation are lumped at the nodes spread on the thin shear layer, where the resolution of the lattice is determined by the number of blade nodes as well as the multiplication of local vortex velocity, v, and the time step between each vorticity calculation, Δt. Since the wake characteristics in this region are significantly affected by the properties of the blades, adopting the vortex-lattice representation enables the better capture of the initial wake evolution. After few time steps, the wake is assumed to instantaneously roll up into the tip and the root vortices, and wake-vortex representation is switched to the vortex filaments, where the tip and the root vortices are connected with the ones from the previous time step.

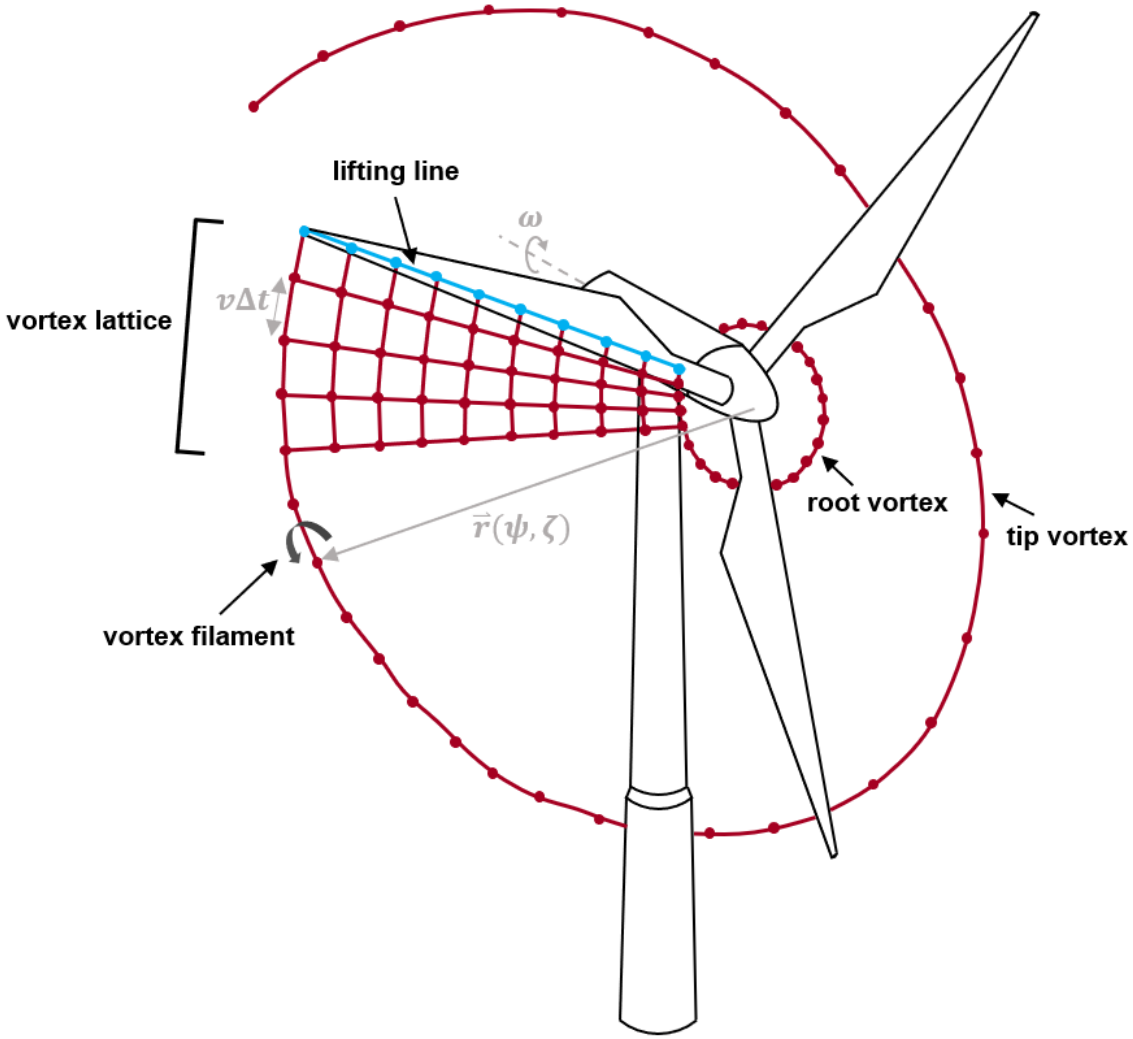

Figure 4-4: The key features of the OLAF module (adopted and modified from [92]). The OLAF module adopts the lifting-line representation (indicated by the blue line) to describe the bound vortices formed on the surface of the blades. The bound vortices are emitted and are allowed to move freely in the wake (indicated by the red dots and lines). These free vortices are initially represented by the vortex lattice and subsequently by the vortex filaments. Between these two representations, the wake is assumed to roll up into tip and the root vortices. The resolution of the vortex lattice is determined by the number of blade nodes as well as the multiplication of local vortex velocity, v, and the time step between each vorticity calculation, Δt. The position of the free vortex is defined by the azimuth position, ψ, and the wake age, ζ.

4-2 Simulation setup

4-2-1 Input specification

Turbine and controller
The IEA-10MW reference turbine [94] is adopted as the turbine model in the study. It is the updated version of the DTU-10MW reference turbine [95], and its key parameters are shown in Table 4-1. To distinguish the impact of the actuation from the impact of the shaft tilt on the wake development, the shaft tilt angle of the IEA-10MW reference turbine is reset to be zero. The OpenFAST input files of the IEA-10MW reference turbine can be found in [96].

In the IEA-10MW reference turbine, the Reference Open-Source Controller (ROSCO) is used [97], which is the expanded version of the Delft Research Controller [98]. The ROSCO is a wind-turbine controller consistent with the industry-standard control functionalities, and it provides the flexibility for users to define its multiple parameters tailored to different turbines. Moreover, the ROSCO is also developed with the control interface which enables the communication with the OpenFAST. Therefore, the pitch input signals can be implemented in the source codes of the ROSCO to achieve the individual actuation activities in the OpenFAST.

Table 4-1: The key parameters of the IEA-10MW reference turbine.

Parameter	Value
Rated electrical power	10 MW
Rotor diameter	198 m
Hub height	119 m
Shaft tilt angle	6 deg
Rotor precone angle	4 deg
Rated wind speed	11 m/s
Maximum rotor speed	8.68 rpm
Design tip-speed ratio	8.2
Maximum pitch rate	7 deg/s

Wind conditions
The inflow wind is set to be a steady and uniform flow with wind speed of 10 m/s. To distinguish the impact of the actuation from the impact of the unsteady inflow wind conditions on the wake development, the inflow wind is assumed to be without the turbulence and the shear effect.

Turbine operations
At the wind speed of 10 m/s, the turbine is operating in the region II where the tip-speed-ratio (TSR) is kept at its designed value to achieve the most efficient power output. Figure 4-5 shows the turbine operations at the wind speed of 10 m/s. The TSR remains at the designed value of 8.2, and it results in the constant rotor speed of 7.9 rpm.

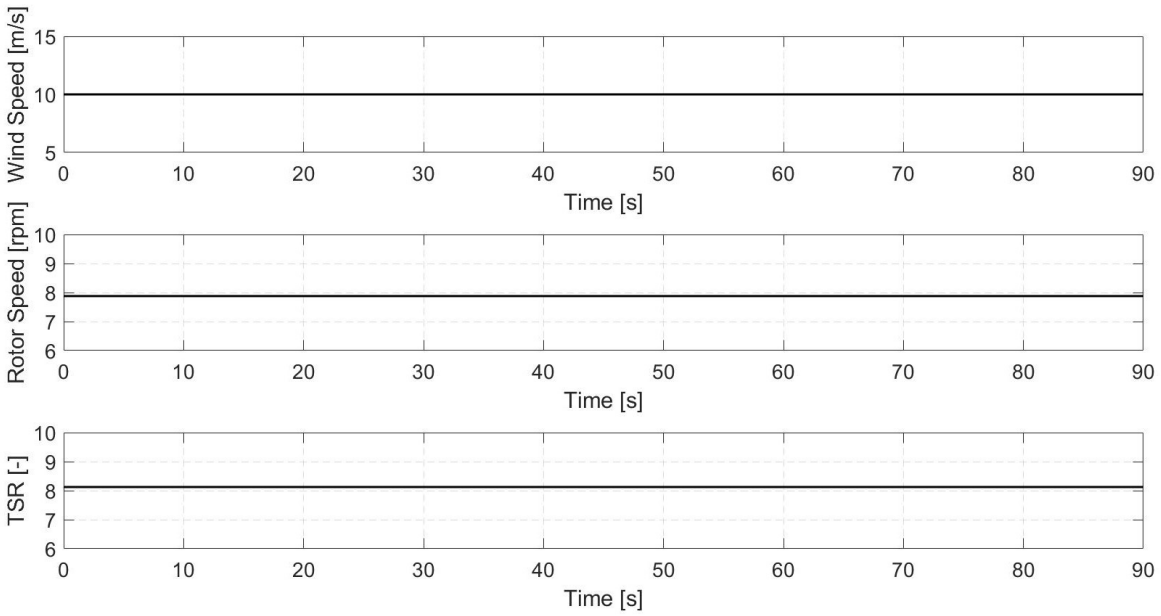

Figure 4-5: The turbine operations simulated in the OpenFAST. The wind speed (upper) is at 10 m/s and the TSR (downer) is kept at the designed value of 8.2, which results in the constant rotor speed (middle) of 7.9 rpm.

4-2-2 Simulation cases

There are four simulation cases considered in this study, which are specified in Table 4-2. In each case, there are the given tilt and the yaw pitch input signals, θ_{tilt} and θ_{yaw}, specified by their amplitudes, frequencies and phases. The excitation frequency, f_e, is usually characterized by the dimensionless Strouhal number, St, defined by Eq. (4-1), where D is the rotor diameter, and U is the free-stream wind speed. It is noted that the optimal f_e has not been determined yet for the Helix approach. To be consistent with the frequency used in the demonstrative study of the Helix approach [31], the same St of 0.25 is adopted is this study, resulting in f_e of around 0.011 Hz at the wind speed of 10 m/s and with the rotor diameter of 198 m.

$$St = \frac{f_e D}{U} \tag{4-1}$$

In *Baseline*, no pitch input signals are implemented. It is used as the baseline of the other cases which adopt different control signals.

In *1P*, the sinusoidal pitch input signals with excitation frequency of f_e are implemented, and the tilt signal is ahead of the yaw signal by $\pi/2$. The inverse MBC transformation with the harmonic index of 1 (or called 1P) is used to project the pitch input signals on the rotating frames to obtain the blade pitch profiles.

In *2P*, the pitch input signals are composed of the 1P component, $\theta_{\text{tilt, 1P}}$ and $\theta_{\text{yaw, 1P}}$ and the

Table 4-2: The specification of simulation cases investigated in this study.

Case		Pitch Input Signals [deg]
Baseline	$\theta_{\text{tilt, 1P}}$	0
	$\theta_{\text{yaw, 1P}}$	0
1P	$\theta_{\text{tilt, 1P}}$	$4 \times \sin(f_e t)$
	$\theta_{\text{yaw, 1P}}$	$4 \times \cos(f_e t)$
2P	$\theta_{\text{tilt, 1P}}$	$1.8 \times \sin(f_e t)$
	$\theta_{\text{yaw, 1P}}$	$1.8 \times \cos(f_e t)$
	$\theta_{\text{tilt, 2P}}$	$1.8 \times \sin(2 f_e t)$
	$\theta_{\text{yaw, 2P}}$	$1.8 \times \cos(f_e t)$
MultiSine	$\theta_{\text{tilt, 1P}}$	$0.3 \times \sin(f_e t)$ - $2.8 \times \sin(3 f_e t) + 2.8 \times \sin(5 f_e t)$
	$\theta_{\text{yaw, 1P}}$	$0.3 \times \cos(f_e t) + 2.8 \times \cos(3 f_e t) + 2.8 \times \cos(5 f_e t)$

2P component, $\theta_{\text{tilt, 2P}}$ and $\theta_{\text{yaw, 2P}}$. The 1P and the 2P pitch input signals have excitation frequency of f_e and $2f_e$, respectively, and they are projected on the rotating frames by the inverse MBC transformation individually with the harmonic index of 1 and 2. The projected value are added together to obtain the final blade pitch profiles. Similar to *1P*, the tilt signals are ahead of the yaw signals by $\pi/2$.

In *MultiSine*, the pitch input signals are composed of multiple sinusoidal pitch input signals with different amplitudes, excitation frequencies and phases. Since there are unlimited combinations of the multi-sine signals, this is the demonstrative case that shows one of the combinations that could achieve promising improvement in wake mixing. In this case, the excitation frequencies are f_e, $3f_e$ and $5f_e$. Similar to *1P*, the inverse MBC transformation with the harmonic index of 1 is used to project the pitch input signals on the rotating frames to obtain the blade pitch profiles.

It is noted that the amplitudes of pitch input signals are different in *1P*, *2P* and *MultiSine*. It is because the actuator duty cycle (ADC) of these cases are kept the same to ensure the loads on the pitch bearings are at the same level when comparing the effectiveness wake-mixing. The calculation of the ADC is achieved by using Eq. (4-2) [99], where T is the total period of the pitch activities, $\beta(t)$ is the pitch rate at the given time of t, and $\beta_{\max}$ is the maximum pitch rate.

$$\text{ADC} = \frac{1}{T} \int_{t=0}^{T} \frac{\beta(t)}{\beta_{\max}} dt \tag{4-2}$$

4-2-3 Fourier stability analysis

In the Helix approach, individual actuation is implemented on each blade, which induces the instability of the wake and stimulates the wake breakdown. To quantify the effectiveness of blade actuation on the wake development, the Fourier stability analysis is employed by identifying the growth of the wake instability.

Figure 4-6 shows the schematic of the Fourier stability analysis. Consider a rotating rotor without any perturbations on the blades. The tip vortices are emitted in the wake and they propagate steadily in the spiral shape along the downstream, which is known as the tip vortical structure and is indicated by the red line. Now, consider the periodic perturbations are introduced on the blades, initiating the fluctuation of the tip vortical structure which is indicated by the blue line. The amplitude of the fluctuation amplifies when these vortices are propagating and interacting with each others. At a certain point, the fluctuation becomes too large that the vortical structure starts to breakdown. This process is recognized as the growth of the vortex instability, which is quantified by the following steps.

The velocity profiles, $u_{j,x}$, in the downstream space domain are collected, where x indicates the position of the cross section along the rotor axis, and j indicates the position of the point on the given cross section where the velocity profile is collected. For each $u_{j,x}$, it is composed of N snapshots taken equidistantly during a period. Each $u_{j,x}$ is then transformed from the time domain to the frequency domain by the Fourier transform defined by Eq. (4-3), where $\hat{u}_{j,x}$ is the Fourier coefficient, n is the index of the snapshot, i is the imaginary unit, and k is the frequency modes.

$$\hat{u}_{j,x} = \frac{1}{N} \sum_{n=0}^{N-1} u_{j,x}\, e^{-2\pi i(\frac{nk}{N})} \tag{4-3}$$

The absolute value of the Fourier coefficient, $|\hat{u}_{j,x}|$, represents the amplitude of the perturbation, and tracking the amplitude of the perturbation along the wake can help illustrate the growth of the instability. To achieve this, the maximum value of $|\hat{u}_{j,x}|$ including all the frequency modes are determined by Eq. (4-4), where $\hat{u}_x^m$ refers to the maximum absolute value of $\hat{u}_{j,x}$ on each cross section.

$$\hat{u}_x^m = \max(|\hat{u}_{j,x}|) \tag{4-4}$$

The growth of the amplitude follows the form of the exponential function in the linear growth region where the mutual induction between the vortices, or known as vortex-pairing, starts [7] and [100], which can be expressed by Eq. (4-5), where σ is the instability growth rate, a and b are the given streamwise positions. When the vortical structure breaks down, it can be observed that the amplitude starts to saturate and stops growing.

$$\frac{\hat{u}_{x=b}^m}{\hat{u}_{x=a}^m} = e^{\sigma(b-a)/U} \tag{4-5}$$

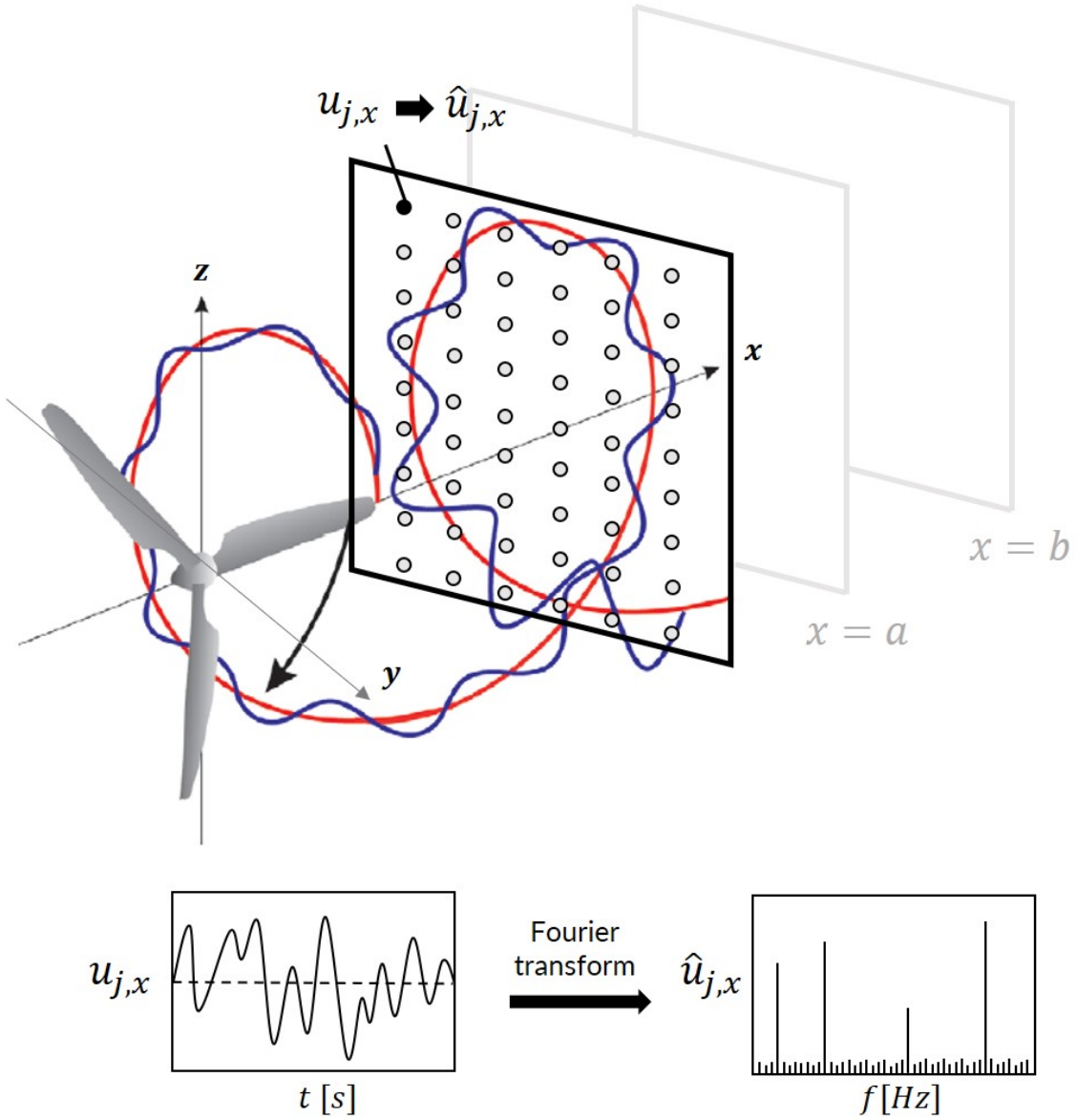

Figure 4-6: The schematic of the Fourier stability analysis (adopted and modified from [7]). The velocity profiles, $u_{j,x}$, collected in the downstream space are transformed from the time domain to the frequency domain by the Fourier transform, which are expressed by $\hat{u}_{j,x}$. On each cross section along the rotor axis, the maximum amplitude of $\hat{u}_{j,x}$ of all the frequency modes are extracted, and these values follow the exponential growth in the region where the vortex-pairing occurs. By tracking the amplitude growth along the streamwise direction, the wake-breakdown process can be identified.

It is noted that the sampling setup can have impact on the results of Fourier stability analysis. Considering the sampling frequency of f_s Hz, and the simulation time of T_s sec, the number of the samples is determined by Eq. (4-6). According to Nyquist–Shannon sampling theorem, the maximum frequency that can be detected is half of the sampling frequency. Moreover, the number of frequency bins obtained by Fast Fourier transform (FFT) is equal to half of the number of samples. Therefore, the intervals between sample in the frequency domain, Δf, is determined by Eq. (4-7). In other words, the size of the intervals between frequency bins is determined by the simulation time.

$$N_s = f_s \times T_s \tag{4-6}$$

$$\Delta f = \frac{f_s/2}{N_s/2} = \frac{1}{T_s} \tag{4-7}$$

The Fourier stability analysis has been widely used in the field of wind turbine to quantify the wake-breakdown process. In the studies of Ivanell et al. [7], Brown et al. [88] and Marten et al. [79], they all use the Fourier stability analysis to track the instability growth induced by the actuation of the blade, and use it to systematically identify the position where the wake-breakdown event starts. In the study of Kleusberg et al. [89], they also use this method to investigate the effect of the wind shear on accelerating the wake breakdown. Therefore, in this study, the Fourier stability analysis provides a systematic way to compare the effectiveness of different pitch input signals.

Chapter 5

Results and Discussions

There are four simulation cases investigated in this study, which are *Baseline*, *1P*, *2P* and *MultiSine*. The pitch input signals are specified in the simulation cases, where the actuator duty cycles for all the cases are equal. To quantitatively identify the wake breakdown position, the Fourier stability analysis is adopted.

In this chapter, the simulation results of these four simulation cases are presented in the following order. First, the blade actuation activities are illustrated, which compare the blade pitch profiles between different cases. Next, the thrust manipulation is demonstrated, which clarifies how the pitch profiles can be used to manipulate the thrust force acting on the wake. Last, the wake development is presented, which shows the effectiveness of manipulating thrust force to enhance the earlier wake breakdown. At the end of the chapter, further discussions about the results are given.

5-1 Blade actuation activities

In the Helix approach, the individual pitch control is described by the blade pitch profiles, which are generated from the tilt and the yaw pitch input signals through the implementation of the inverse MBC transformation. Figure 5-1 shows the blade actuation activities in four simulation cases indicated by (a) to (d), where the upper sub-figures are the pitch input signals and the downer sub-figures are the blade pitch profiles.

In *Baseline*, no control inputs are implemented. Therefore, both the pitch input signals and the individual blade pitch profiles remain constant at zero. This case is used as the baseline for the other cases adopting the control inputs.

In *1P*, the sinusoidal pitch input signals are used, where the tilt signal (blue line) is ahead of the yaw signal (orange line) by $\pi/2$. The excitation frequency of 0.011 Hz results in the signal

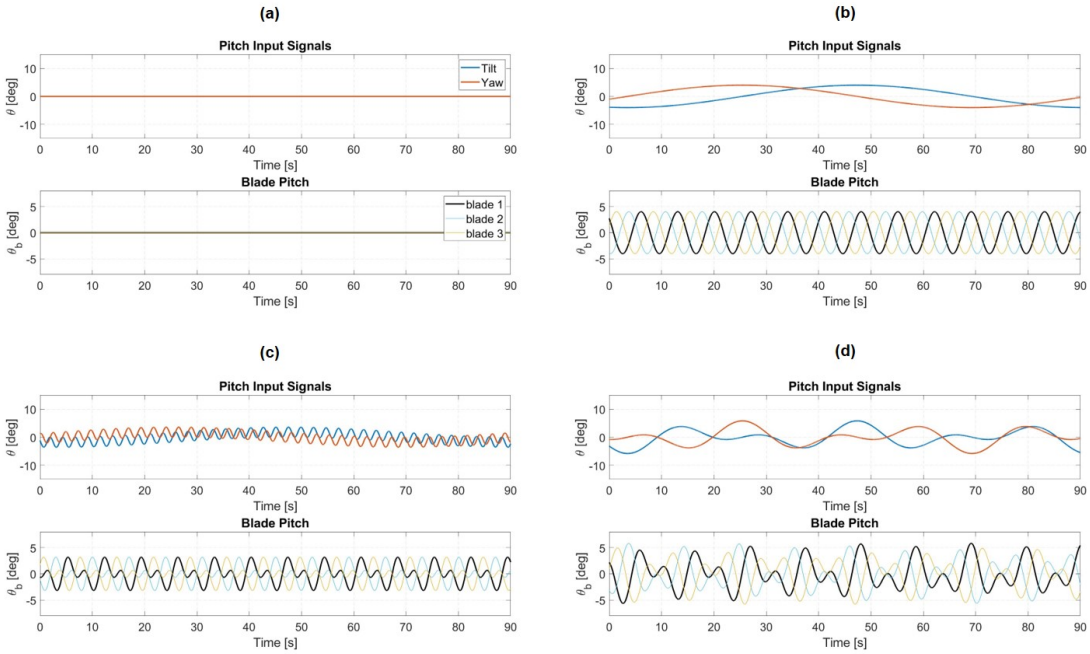

Figure 5-1: The pitch input signals (upper) and the blade pitch profiles (downer) in the 90-second period for simulation cases of (a) *Baseline* (b) *1P* (c) *2P* (d) *MultiSine*. The tilt and the pitch input signals are represented by the blue and the orange line, respectively. The blade pitch profiles are represented by the black, the light blue and the yellow lines. Since the blade is equidistantly located, each blade pitch profile has the azimuth difference of $\pi/3$ in between.

period of around 90 seconds. The inverse MBC transformation of the harmonic index of 1 is then used to project the pitch input signals on the rotating frames to obtain the blade pitch profiles (black, light blue and yellow lines). In the inverse MBC transformation, the azimuth positions of the blades are coupled with the pitch input signals. Therefore, the frequency of the blade pitch profiles is the summation of the excitation frequency and the rotational frequency, resulting in the much more higher value of 0.141 Hz.

In *2P*, the pitch input signals are composed of the 1P sinusoidal signals with the excitation frequency of 0.011 Hz and the 2P sinusoidal signals with the excitation frequency of 0.022 Hz. The 1P and the 2P signals are projected on the rotating frames by the inverse MBC transformation with the harmonic index of 1 and 2, respectively. The projected values are then added together to obtain the eventual blade pitch profiles. It is noted that *2P* has the very similar blade pitch profiles as *1P* does, and there are higher frequency components included in the signals..

In *MultiSine*, pitch input signals are composed of three sinusoidal signals with the excitation frequency of 0.011 Hz, 0.033 Hz and 0.055 Hz. Again, the inverse MBC transformation with the harmonic index of 1 is used to project the pitch input signals on the rotating frames to obtain the blade pitch profiles. It is shown that the blade pitch profiles of *MultiSine* are not the sinusoidal waves. Instead, the blade pitch profiles are more complex and contain signals

of multiple amplitudes and excitation frequencies.

Based on the blade pitch profiles, the actuator duty cycle (ADC) of all the cases are calculated. For *Baseline*, there is no pitch activities, therefore, the ADC is 0. For *1P*, *2P* and *MultiSine*, the ADC are all calculated to be 0.35, which means their loads on pitch bearings are controlled at the same level.

5-2 Thrust manipulation

The individual pitch control is implemented in accordance with the blade pitch profiles. Due to the dynamic change of the blade pitch angles, the aerodynamic loads along each of blades vary with time, which induces the dynamic moments on the blade roots. The blade root moments of three blades are projected on the fixed frame by the MBC transformation of harmonic index of 1, and the combined effect can be expressed by the collective, the tilt and the yaw root moment signals, as shown in Figure 5-2. It is noted that the root moment signals are the amplitude-scaled and phase-shifted response with the same frequency content of the pitch input signals. Moreover, there are high-frequency fluctuations in the moment signals in *1P*, *2P* and *MultiSine*. The reasons for these fluctuations have not been clearly clarified in this study, and to the author's best knowledge, the potential causes can be the blade vibrations or the instability due to the transient states.

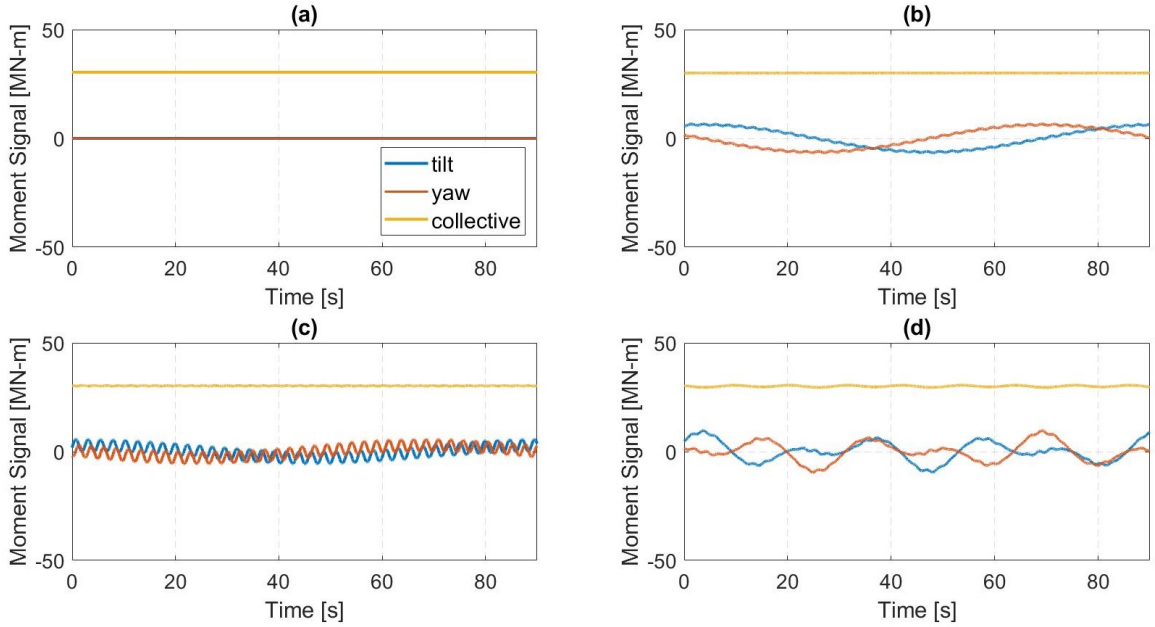

Figure 5-2: The root moment signals on the fixed frame in the 90-second period for simulation cases of (a) *Baseline* (b) *1P* (c) *2P* (d) *MultiSine*. The collective moment signal, the tilt moment signal and the yaw moment signal is represented by the yellow, the blue and the orange line, respectively.

The tilt and the yaw moment signals are created since the thrust force is not acting on the center of the rotor. Figure 5-3 demonstrates the thrust force position and the moment signals,

taking the example of *1P*. Firstly, the thrust force deviates from the rotor center due to the different aerodynamic loads experienced by each of blades. The deviation of the thrust force position creates the lever arm. With the lever arm, the thrust force creates the moment relative to the rotor center. The created moment can then be decomposed into the horizontal and the vertical direction, which is expressed as the tilt and the yaw moment, respectively. In the other way around, with the profiles of the tilt and the yaw moment signals, the position of thrust force can be determined. Moreover, the collective moment is also obtained through the MBC transformation. It is the overall moment contributed by aerodynamic loads on three blades, and it is the indicator of the magnitude of the thrust force.

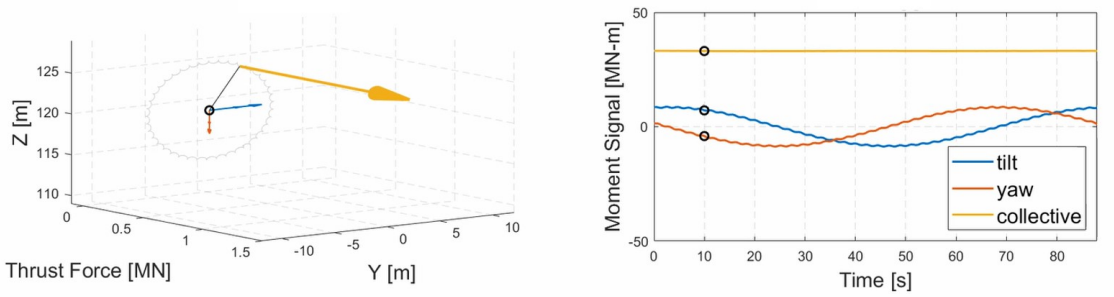

Figure 5-3: The thrust force position and the moment signals at the time instance of 10_{th} second in *1P*. The thrust force is the overall force seen by the rotor, which is represented by the yellow arrow. The collective, the tilt and the yaw moment signal is represented by the yellow, the blue and the orange line, respectively. The black circle on the left side of the figure represents the rotor center at the hub hieght of 119 meters, the black line is the lever arm, and the grey circle is the trajectory of the thrust force position in the 90-second period. In this example, the thrust force with constant magnitude is rotating circularly around the rotor center.

According to the tilt and the yaw moment signals, the trajectory of the thrust force position from the front view on the rotor plane for four simulation cases is determined, as illustrated in Figure 5-4. The trajectory is represented by the color from blue to yellow with respect to the simulation time from the beginning to the end. In *Baseline*, the thrust force is constantly acting on the center of the rotor at the hub height of 119 meters. In *1P*, the thrust force deviates from the center of the rotor by around 5 meters, and is rotating circularly around the rotor center in the clockwise direction. In *2P*, the trajectory of the thrust force is more complex, but it follows the similar path as the one of *1P*. The thrust force is rotating in a large circle around the rotor center with the radius of around 5 meters in the clockwise direction, which is contributed by the 1P signals. During the rotation of the large circle, the thrust force is also rotating in a small circle with the radius of around 2.5 meters in the counter clockwise direction, which is contributed by the 2P signals. In *MultiSine*, the trajectory of the thrust force is also complex and looks like a flower with respect to the rotor center, which is explained in the following. Starting from the location of around (X,Y)=(0, 130), the thrust force passes through the rotor center of (X,Y)=(0, 119) and moves to the location of around (X,Y)=(5,113). The same process repeats over and over again, resulting in the trajectory of the shape of flower with eight petals in the clockwise direction. It is noted that the trajectory of *1P*, *2P* and *MultiSine* are not entirely smooth, and it is caused by the fluctuations of the moment signals as previously mentioned.

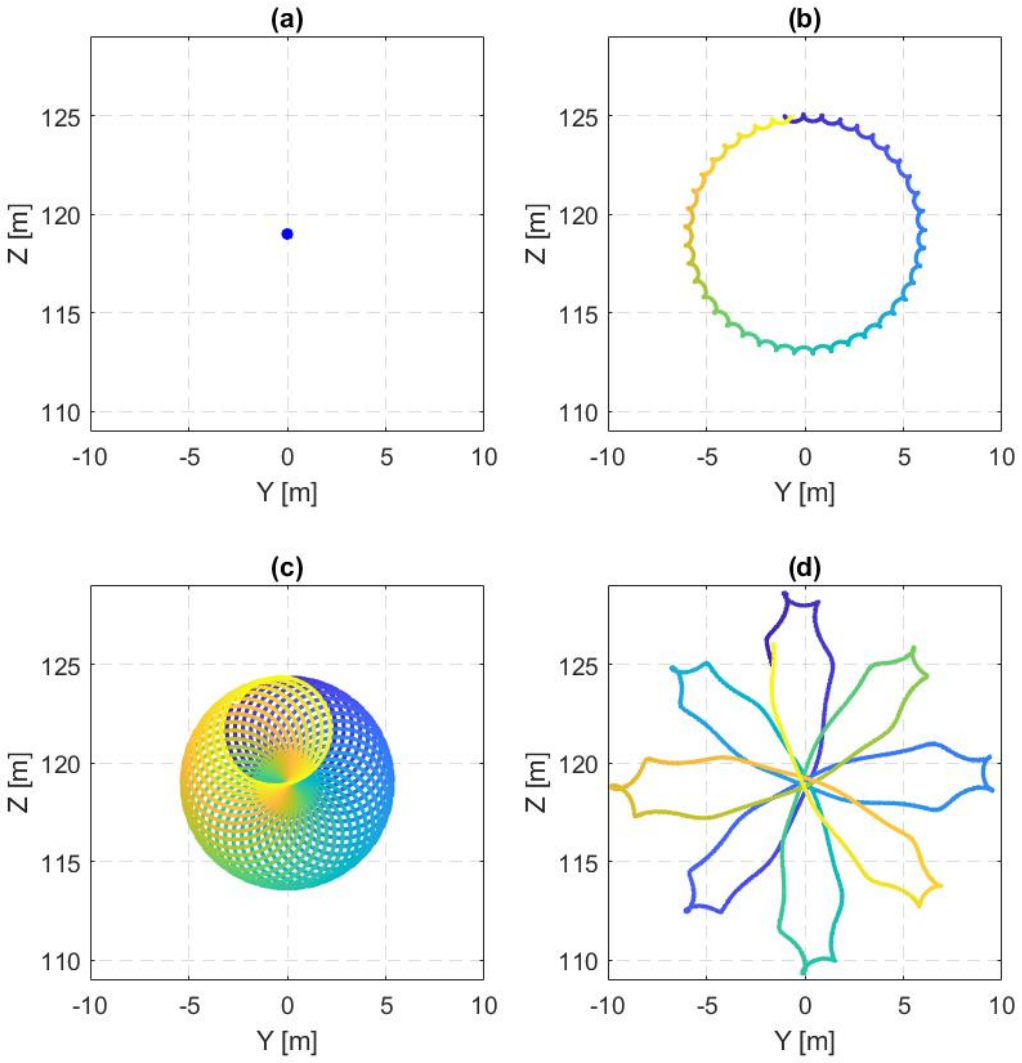

Figure 5-4: The trajectory of the thrust force position from the front view on the rotor plane for simulation cases of (a) *Baseline* (b) *1P* (c) *2P* (d) *MultiSine*. The Y and Z is the horizontal and the vertical coordinate, respectively, together representing the rotor plane. The trajectory is represented by the color from blue to yellow with respect to the simulation time from the beginning to the end.

The magnitude of the thrust force and the power for the 90-second period in four simulation cases are shown in Figure 5-5, where the average and the standard deviation are listed in Table 5-1. For both *Baseline* and *1P*, the thrust force and the power remain almost constant with time, so the very small standard variations are observed for these two cases. However, in *1P*, the average thrust force and power are slightly lower than *Baseline* by around 1% and 4%, respectively. For both *2P* and *MultiSine*, the average of thrust force and power are almost the same as the ones of *Baseline*, but the standard deviation of these two cases all increase. For *2P*, the standard deviation of thrust and power increases by 33% and 80%, respectively. For *MultiSine*, the standard deviation of thrust and power increase even more by 160% and 230%, respectively. Although the thrust force and power deviation in *2P* and *MultiSine* significantly increase compared with *Baseline* and *1P*, the scales of the deviation are still quite small relative to their average values.

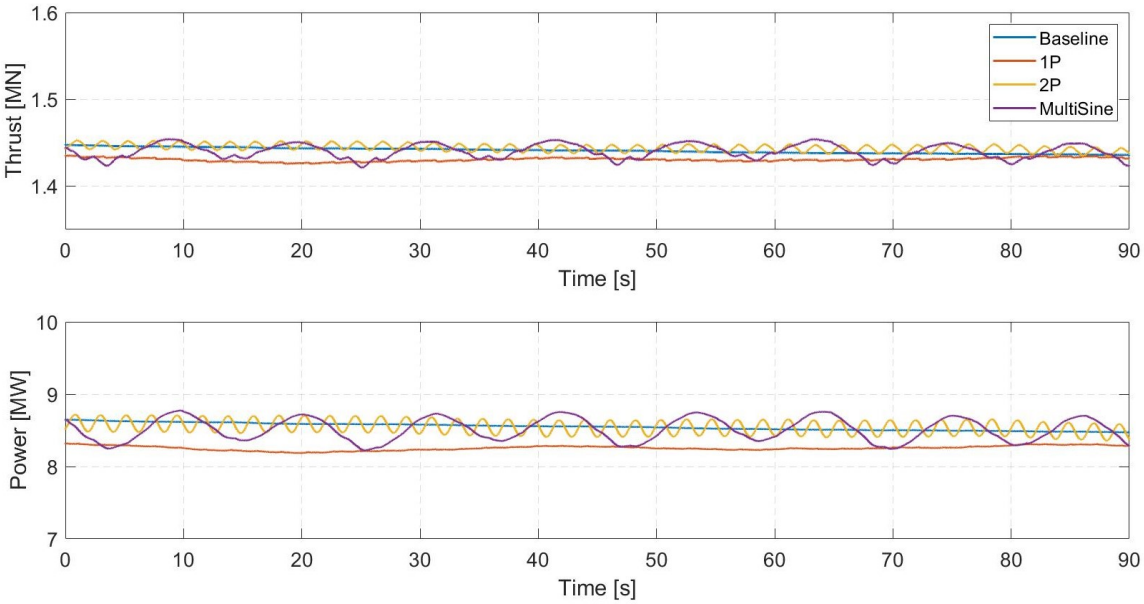

Figure 5-5: The magnitude of the thrust force (upper) and the power (downer) for the 90-second period in four simulation cases. The blue, the orange, the yellow and the purple represents *Baseline*, *1P*, *2P* and *MultiSine*, respectively.

Table 5-1: The average and the standard deviation of the thrust force and the power in four simulation cases.

	Thrust [MN]		**Power [MW]**	
	average	standard deviation	average	standard deviation
Baseline	1.441	0.003	8.547	0.048
1P	1.430	0.002	8.250	0.031
2P	1.444	0.004	8.543	0.088
MultiSine	1.440	0.008	8.510	0.157

5-3 Wake development

It has been demonstrated in the previous section that the position of the thrust force is dynamically varying through the implementation of the pitch input signals. In this section, the impacts of the dynamic thrust force manipulation on the wake development are comprehensively presented.

To understand the wake development, the transport of the vortices shed from the rotor is numerically solved by the free vortex wake method. Figure 5-6 shows the instantaneous capture of the vortex evolution in the wake in four simulation cases. Firstly, the vortices are formed on the the blades and then emitted into the wake. It is noted that the vortex lattice representation is adopted in the region of around 30° of span close to the blades, which means the movement of vortices generated along the blade nodes in the spanwise direction are all captured. These vortices are presented by the blue particles. After this region, the wake is assumed to instantaneously roll up into the tip and the root vortices, which are represented by the blue and the red particles, respectively. The main structure of the wake is characterized by the evolution of the tip and the root vortices.

In *Baseline*, the thrust force is acting on the center of the rotor. Therefore, the wake is constantly formed in align with the inflow wind direction. In the beginning, both the tip and the root vortices form the vortical structures in the wake. At the downstream distance of around 300-400 meters, the structure of the root vortices starts to break down. However, the breakdown of the root vortices does not immediately induce the wake mixing. As previously described in Figure 1-2, the wake mixing process is mainly triggered by the breakdown of the tip vortical structure which prevents the kinetic energy transport across the shear layer. Therefore, after the downstream distance of around 400-500 meters when the structure of the tip vortices breaks down, the wake shortly starts mixing. It is noted that the breakdown of both the tip and the root vortices is driven by the mutual induction between vortices, which is also known as leapfrogging instability or vortex-pairing as mentioned in Figure 1-2. For the root vortices, they are more close to each others and therefore have stronger leapfrogging instability, which makes them break down earlier than the tip vortices [7]. In *Baseline* without any dynamic wake deflection, the wake fully breaks down at the downstream distance of around 600 meters.

In *1P*, the thrust force deviates from the center of the rotor, and its position is rotating around the rotor center in the clockwise direction. The aforementioned thrust profile leads to the helical wake deformation in the downstream. The deformation of wake induce stronger interactions between vortices which leads to wake instability. Therefore, the root vortical structure breaks down earlier at the downstream distance of around 200-300 meters. Moreover, the earlier breakdown of the root vortical structure seems to induce the the breakdown of the tip vortical structure. At the downstream distance of around 400-500 meters, the wake starts mixing.

In *2P*, the thrust force is manipulated in the more complex profile which is previously explained in Figure 5-4. In this case, the vortices are formed into two separate structures, and

these two structures individually rotate around the rotor axis in the helical shape. The effectiveness of *2P* seems quite similar to *1P*, where the wake also starts mixing at the downstream distance of around 400-500 meters.

In *MultiSine*, the thrust force is manipulated by multi-sine pitch input signals composed of different amplitudes and frequencies, resulting in the flower shape of the thrust position profile as previously explained in Figure 5-4. In this case, the thrust force position moves closer to and further away from the rotor center periodically. By doing so, the boundary of the wake is dynamically perturbed, which induces the instability of the tip vortical structures. This perturbation provides the driving force to trigger the breakdown of the tip vortical structure, which is regarded as the main structure preventing the wake mixing. Therefore, the tip vortical structure breaks down substantially earlier than pervious cases, resulting in the onset of wake mixing at the downstream distance of around 200-300 meters.

Overall, *1P*, *2P* and *MultiSine* all achieve the earlier breakdown of the tip vortical structure than *Baseline* does, which fosters the onset of the subsequent wake-mixing process. For *1P* and *2P*, they achieve the similar effectiveness where the wake mixing process starts at the downstream distance of around 400-500 meters, which is 100-200 meters earlier than the one of *Baseline*. For *MultiSine*, stronger perturbations on the tip vortical structure are induced, and the wake mixing process starts much more earlier at the downstream distance of around 200-300 meters.

The velocity field behind the rotor at the distance of one rotor diameter (1D) from the front view is shown in Figure 5-7, where the red area represents the higher wind velocity and the black circle represents the rotor region projected on the 1D plane. The velocity field is captured every 11 seconds for the total period of 88 seconds, which is one period of the Helix approach corresponding to the excitation frequency of 0.011 Hz. In *Baseline*, the wake is in align with the inflow wind direction, and remains at the same position with respect to the rotor region projected at 1D downstream distance. In *1P*, it can be observed that the wake is deflected from the rotor region projected at 1D downstream distance, and rotates in the clockwise direction with time. In *2P*, the wake is deformed into the elliptical shape and also rotates in the clockwise direction with time. In *MultiSine*, there is no clear rotation of the wake such as the ones in the previous cases. It is noted that the boundary of the wake becomes blurred with the ambient flow, and it is an important indication that the tip vortical structure already starts to break down.

The time-averaged vorticity and the velocity field on the horizontal plane across the rotor center is demonstrated in Figure 5-8. From the vorticity field, the positions where the tip and the root vortical structures start to break down can be clearly identified. In *Baseline*, the wake fully breaks down at the downstream distance of 600 meters. In *1P* and *2P*, the breaks down both happen earlier at the downstream distance of 400 meters. In *MultiSine*, the breakdown occurs even earlier at the downstream distance of 200 meters. As long as the wake fully breaks down, the wake-mixing process starts, and the wind velocity starts to recover.

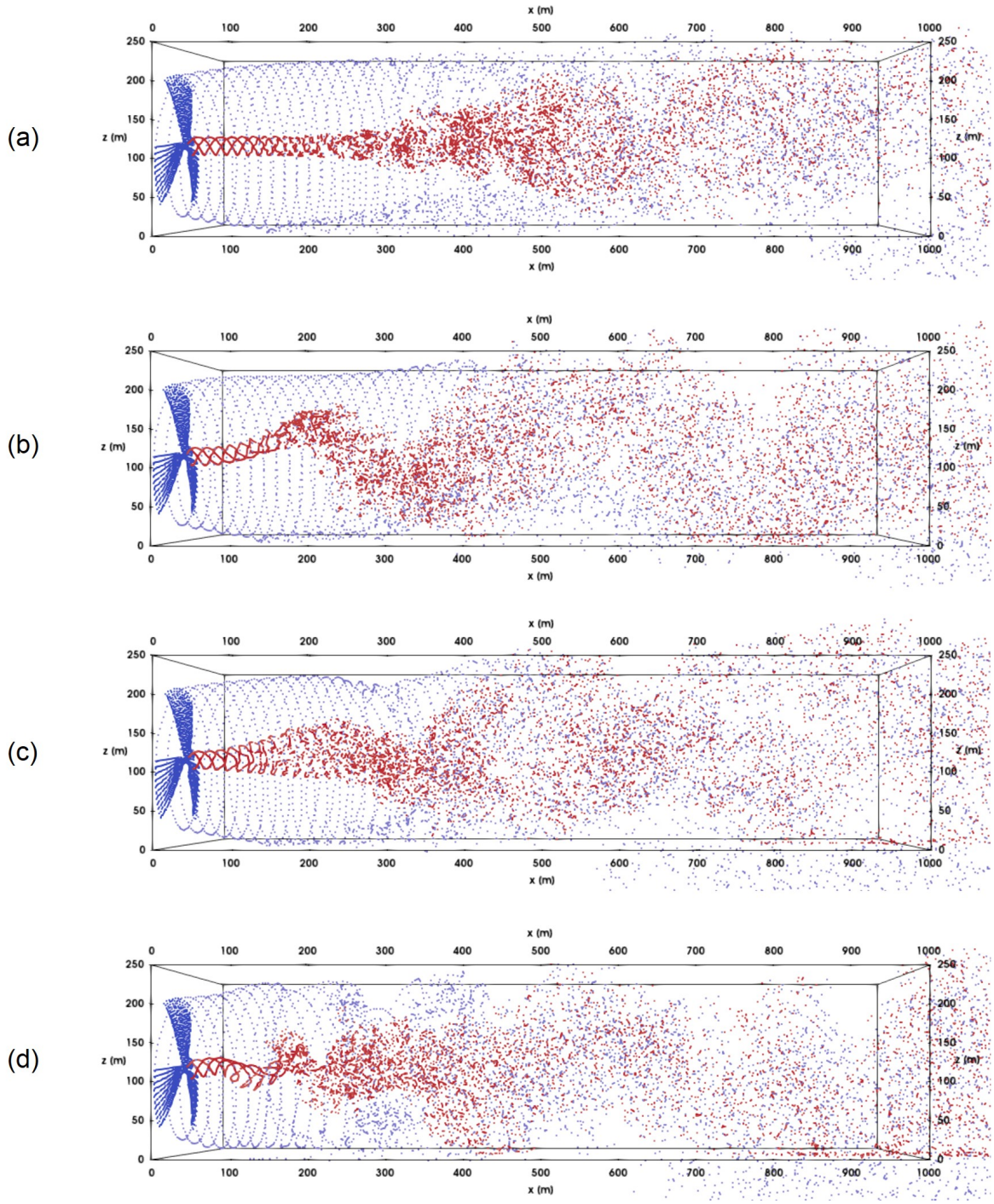

Figure 5-6: The instantaneous capture of the vortex evolution in four simulation cases of *Baseline* (b) *1P* (c) *2P* (d) *MultiSine*. The simulation is done by the OpenFAST with the OLAF wake module. The vortices are generated on the lifting line of the blades, and they are emitted into the wake. In the wake region of around 30^{circ} of span close to the blades, the vortex lattice representation is adopted, where the vortices on the blade nodes in the spanwise direction are captured. These vortices are represented by the blue particles. After this region, the wake is assumed to roll up into the tip and the root vortices, which are represented by the blue and the red particles, respectively.

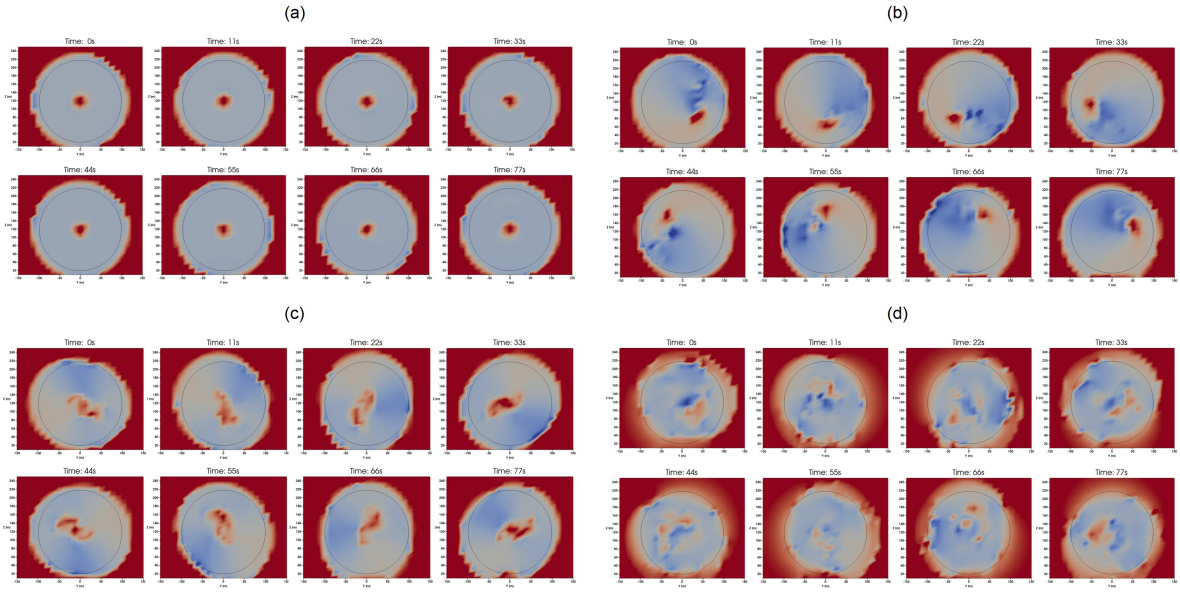

Figure 5-7: The velocity field behind the rotor at the distance of one rotor diameter (1D) from the front view at different time instances in four simulation cases of (a) *Baseline* (b) *1P* (c) *2P* (d) *MultiSine*. The red area represents the higher wind velocity and the black circle represents the rotor region projected on the 1D plane.

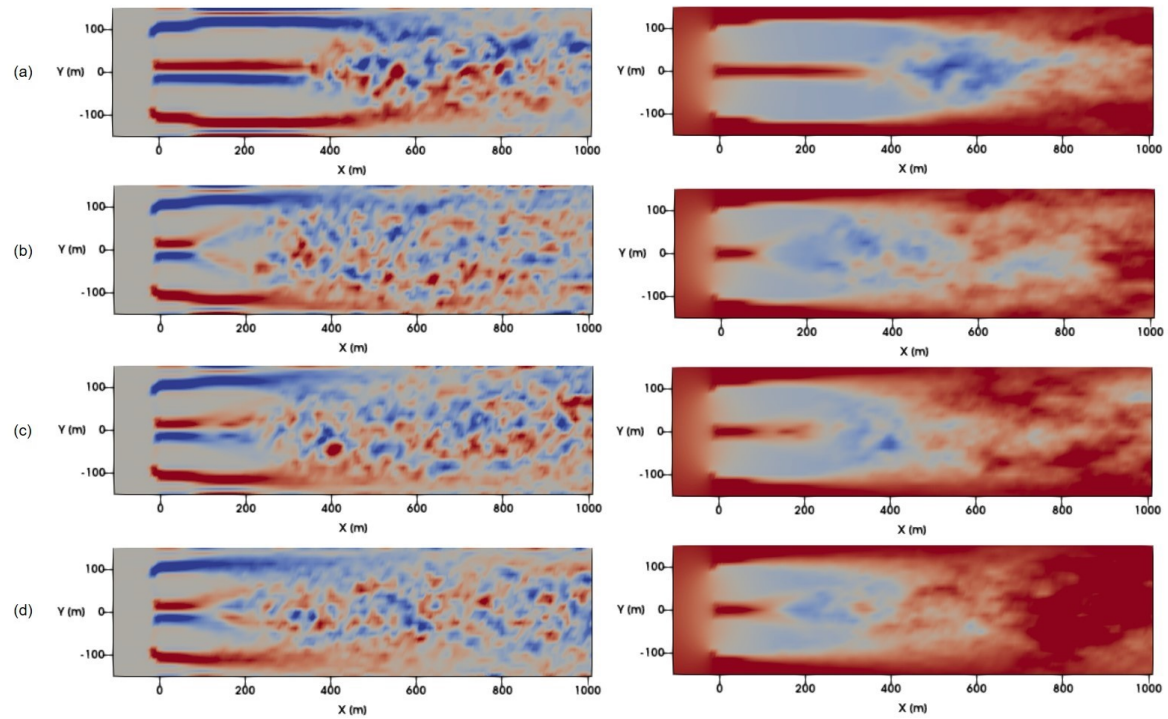

Figure 5-8: The time-averaged vorticity (left) and the velocity (right) field on the horizontal plane across the rotor center in four simulation cases of (a) *Baseline* (b) *1P* (c) *2P* (d) *MultiSine*. In the velocity field, the red area represents the higher wind velocity. In the vorticity field, the red and blue represent the different direction of the vorticity.

The previous figures visualize the wake development and clearly demonstrate the effectiveness of each cases by analyzing the vorticity and the velocity field in a qualitative way. Here, the Fourier stability analysis is exploited to provide a more quantitative aspect in comparing these cases. In the Fourier analysis, the velocity field is sampled at the dimensionless downstream locations, and the velocity profiles are transformed from the time domain to the frequency domain via the Fourier transform. At each dimensionless downstream distance, the maximum absolute value of the Fourier coefficient represents the amplitude of the perturbation at that location, which is regarded as the indicator of instability. Therefore, by tracking the amplitude of the perturbation along the downstream distance, the instability growth and the wake breakdown location can be identified.

Figure 5-9 shows the instability growth along the dimensionless downstream distance in four simulation cases. The horizontal axis is the dimensionless downstream distance, and vertical axis is the maximum absolute Fourier coefficient normalized by the value at the dimensionless downstream distance of 0.25D from *Baseline* in logarithmic scale. In the semi-logarithmic plot, the linear trend refers to the exponential change of the value, and this is regarded as the instability growth caused by the vortex-pairing. The instability continues growing until the wake fully breaks down and enters the wake-mixing process. Therefore, the location where the instability starts to saturate implies the location where the wake fully breaks down. By doing so, the simulation cases can be compared by identifying their wake breakdown locations.

For example, in *Baseline*, the linear instability growth starts at 1.5 D and ends at 3.25 D. It means that the vortex pairing starts at 1.5 D, and the instability is accumulating and amplifying until the vortices are fully mixed up at 3.25 D. In other words, the downstream distance of 3.25 D can be regarded as the location where the wake fully breaks down. Therefore, for *1P*, *2P* and *MultiSine*, the wake breakdown location is 2.5 D, 2.5D and 1.75 D, respectively. The results of the Fourier instability analysis show that *MultiSine* has the substantial improvement in simulating the wake breakdown.

Moreover, the frequency components in the wake are also analyzed by Fourier analysis, as illustrated in Figure 5-10. The horizontal axis represents the dimensionless downstream distance, the vertical axis represents the frequency domain, and the color represents the value of Fourier coefficients. The dashed lines represent the integer multiples of the base excitation frequency of 0.011 Hz. Based on the sampling setup, the intervals between the frequency bins are 0.011 Hz. Moreover, in this contour plot, the values between the intervals are linearly interpolated.

Along the downstream distance, it can generally be divided into three regions, taking *Baseline* for example. In the first region, the vorical structures are very stable, where the vortices follow the helical paths with limited interactions with each others. Therefore, the magnitude of perturbation is low and does not accumulate, which corresponds to the downstream distance from 0 to 1.5 D in the color of dark blue. In the second region, the perturbation of the vortices starts accumulating and amplifying due to their interactions. It is known as the process of vortex pairing where the magnitude of the perturbation grows in an exponential manner, which corresponds to the downstream distance from 1.5 to around 3.25 D in the transient

color from dark blue to yellow. In the last region, the vortical structures fully break down and transit into the wake-mixing process. The magnitude of perturbation saturates and stops growing in this stage, which corresponds the downstream distance after 3.25 D.

In *1P*, the frequency of 0.01 Hz has the higher magnitudes than the other frequencies in the first region. The frequency peak is in align with the excitation frequency of 0.011 Hz. Therefore, it is considered to be induced by the excitation frequency of blade pitch profiles. It is noted that the frequency at the wake breakdown position of 3 D is about 0.02 Hz, which is around the second harmonics of the excitation frequency. In *2P*, the frequency of 0.02 Hz has the higher magnitudes than the other frequencies in the first region, which is aligned with the main excitation frequency of 0.02 Hz. Similarly to *1P*, the frequency at the wake breakdown position of 3 D is about 0.04 Hz, which is also around the second harmonics of the excitation frequency. In *MultiSine*, there are frequency peaks at 0.03 and 0.05 Hz, which also match the excitation frequencies of the blade pitch profiles.

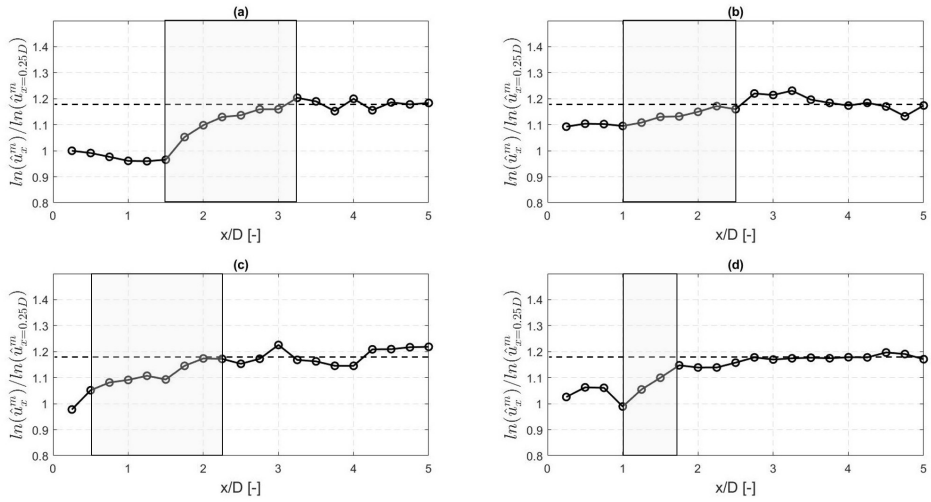

Figure 5-9: The instability growth along the dimensionless downstream distance in four simulation cases of (a) *Baseline* (b) *1P* (c) *2P* (d) *MultiSine*.The horizontal axis is the dimensionless downstream distance, and the vertical axis is the maximum absolute Fourier coefficient normalized by the value at the dimensionless downstream distance of 0.25 from *Baseline* in logarithmic scale. The grey area represents the instability linear growth region.

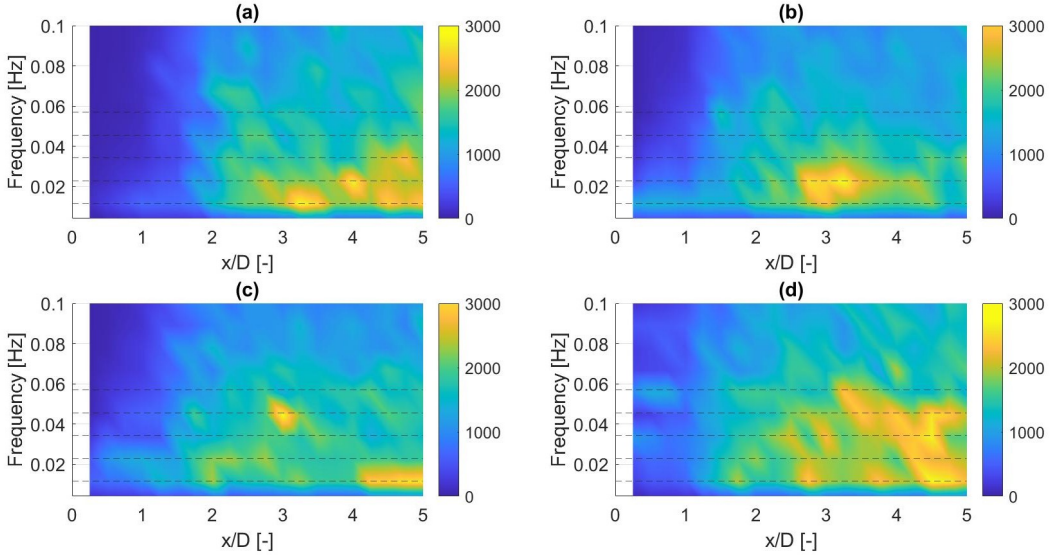

Figure 5-10: The absolute value of Fourier coefficients along the dimensionless downstream distance in the frequency domain from from 0 to 0.1 Hz in four simulation cases of (a) *Baseline* (b) *1P* (c) *2P* (d) *MultiSine*. The horizontal axis represents dimensionless downstream distance, the vertical axis represents the frequency domain, and the color represents the value of Fourier coefficients. The dashed lines represent the integer multiples of the base excitation frequency of 0.011 Hz.

5-4 Discussions

Regarding the simulation results, there are several points of view that can help interpret the results more carefully, which are discussed in the following.

Design of pitch input signals
The excitation frequency used in the Helix approach, both in *1P*, *2P* and *MultiSine*, is based on 0.011 Hz. The value is obtained by assuming the Strouhal number (St) to be 0.25, which is the frequency used in the previous study of the Helix approach [31]. However, this frequency may not be the optimal one that achieves the most effective wake mixing. Therefore, it should be careful in the future study that the other excitation frequencies can possibly achieve better effects on wake mixing.

Moreover, it is noted that the excitation frequency of 0.011 Hz is a very low value compared with the rotational frequency. For example, the rotational frequency of the IEA-10MW reference turbine at wind speed of 10 m/s is 0.13 Hz, which is around eleven times faster than the excitation frequency. That is, it takes about 8 seconds to finish a rotation, but it takes about 90 seconds to finish a period of the individual pitch control in the Helix approach. In fact, the frequency of the Helix approach is proposed to be low in order to limit the increase of the loads on the pitch bearings. In the similar way, the amplitudes of the pitch input signals also determine the loads on the pitch bearings. Therefore, the actuator duty cycle (ADC) is used in this study to control the pitch bearing loads at the same level. The ADC is a relatively simple parameter, so more detailed load analysis such as fatigue load analysis is still required when designing the pitch input signals.

Numerical instability
The numerical instability of the free vortex wake (FVW) method should be cautiously considered especially when adopting this method for the stability analysis [101]. In the FVW method, there are several assumptions that can possibly induce the significant numerical instability.

Firstly, the wake is discretized into vortex elements where their movements are solved through the vorticity transport equation. The improper discrete resolution may lead to the significant numerical instability that diverges the simulation results from the real and continuous wake dynamics. Generally, the azimuth step size of around 5 deg is required to achieve the sufficient numerical stability [91] and [102]. Therefore, in this study, the azimuth step size is determined within the range.

Secondly, the Biot-Savart law is used in the FVW method to describe the velocity field induced by the vortex elements. At the locations close to the vortex elements, the velocity field becomes extremely large, which is regarded as the issue of singularity. To prevent the singularity, the regularization is required, in which the velocity field close to the vortex elements is smoothed by the vicious models. The vicious models are empirical formulation, and the parameters are normally determined experimentally. Therefore, the inappropriate adoption

of the vicious model and its parameters can lead to the numerical instability.

Thirdly, to solve the vorticitiy transport equation, the time-marching method is used to integrate the derivative expression of the Lagrangian-marker movement numerically. In the numerical integration, the higher-order terms of the derivative expression are truncated to reduce the computational costs, which inherently induces the artificial instability .

To sum up, it is inevitable to entirely avoid the numerical instability in the FVW method. Although it is a difficulty to differentiate the numerically-induced instability from the fluid dynamics instability, the FVW method is still regarded as a valid way to compare the wake development between different control solutions [88].

Far wake prediction
The OLAF module of the OpenFAST adopts the vortex filaments to represent the vorticity field in the wake. In this approach, the vortices are constrained to be connected to the adjacent ones. As discussed in Section 3-3-3, this connectivity requirement leads to the three dimensional distortion of the wake in the turbulent mixing region. Therefore, the vortex-filament representation is considered not to be capable of predicting the vorticity and the velocity field in the far wake region where the wake is turbulently mixing. That is , the vorticity and the velocity field in the region where the wake is fully mixed shown in Figure 5-8 tends to be the artificial result and not representative, so the velocity recovery is not considered to be compared in this study.

Due to the limitations of the vortex-filament-based FVW method, the study is instead focusing on the breakdown process of the vortical structures in the near wake region, where the wake has not been in the mixing stage. By doing so, the impact of the control solutions on the near-wake development can still be investigated. For example, for the control solutions that result in the earlier wake breakdown, they are considered to have better wake recovery since the wake mixing process also starts earlier. However, the impact of the control solutions on the far wake development cannot be identified in this study. For example, the recovery rate in the wake mixing process can be different for different control solutions.

Fourier stability analysis
The sampling setup of the Fourier stability analysis in this study results in the intervals of 0.01 Hz between frequency bins. To generate the smooth contour plot, the values between the intervals are interpolated. Since the base excitation frequency is also 0.01 Hz, the integer multiples of the base excitation frequency can be detected on the frequency bins. However, the frequency components that fall between the integer multiples of the base frequency may also exist in the wake, and the current sampling setup is unable to capture these frequencies. Therefore, the sampling setup that can reach the smaller intervals between frequency bins is required in the future study to investigate the non-integer multiples of base excitation frequency in the wake.

Chapter 6

Conclusions and Recommendations

6-1 Conclusions

The wake effects in wind farms induced by upstream turbines lead to the wind flow with decreased kinetic energy and increased turbulence levels on the downstream turbines. The decreased kinetic energy reduces the power production of downstream turbines, which leads to the loss of annual energy production by 10-40% for modern wind farms. Moreover, the increased turbulence level induces additional fatigue loads on waked turbines, which leads to premature damages on turbine components. For these two reasons, the overall wind farm performance is substantially reduced. Therefore, effective wind farm control strategies to mitigate the wake effects have been considered in the past decade. Several wind farm control strategies have been proposed, simulated and experimentally tested. The wake steering control strategy adopting the yaw misalignment and the dynamic induction control strategy exploiting the collective pitch control technique both demonstrate promising results in enhancing the wind farm performance.

Recently, a novel wind farm control strategy called the Helix approach is conceptually proposed. The Helix approach takes advantage of the individual pitch control (IPC) technique to deform the wake into the helical shape. By doing so, the wake becomes more unstable and thereby breaks down earlier, which enhances the wake mixing process and stimulates wake recovery. Therefore, this state-of-art control strategy shows the potential in mitigating the wake effects, but it also requires further optimization and validation before the business case can be truly defined.

One of the research gaps of the Helix approach is the design of the IPC profiles. The IPC profiles are the dynamic pitch-angle commands for each of the blades, and they determine the actuation activities of the individual blades. In the conceptual study of the Helix approach, the IPC profiles are constrained to a single-harmonic sinusoidal form. This constraint arouses the interest of this study to explore the potential of adopting IPC profiles in other forms to

further stimulate wake recovery capabilities. Therefore, the goal of this master thesis recalled from Section 1-4 is in the following:

Thesis goal: Explore the potential of using multiple sinusoidal pitch input signals in the Helix approach to further stimulate wake mixing to achieve faster wake recovery.

To achieve the thesis goal, three questions proposed are addressed in this study, which are summarized as follows:

Question 1: How is the existing IPC and Helix control framework used to effectuate a framework for the synthesis of a multi-sine Helix control strategy?

Chapter 2 addresses this question by linking the pitch input signals to the thrust force position, which follows the framework of the Helix approach. Firstly, the fixed-frame tilt and yaw pitch input signals are transformed to their rotating frame representations through the inverse multi-blade coordinate (MBC) transformation. The pitch signals on the rotating frames are called the IPC profiles, which describe the actuation activities corresponding to each of the blades. With the implementation of IPC, the thrust force is deviated from the center of the rotor due to the different aerodynamic loads experienced by the blades, inducing the different moment signals that can be measured at the blade roots. These blade root moment signals are subsequently transformed back to the fixed frame, and are expressed in the tilt and the yaw directions. In fact, these tilt and the yaw moment signals are the contribution of the overall thrust force acting with the lever arm to the rotor center. Therefore, with the information of the tilt and yaw moment signals as well as the magnitude of the thrust force, the position of the thrust force on the rotor plane can be identified. Through the framework, the thrust force position can be manipulated in a desired manner by implementing the corresponding pitch input signals. In other words, the framework provides an effective way to synthesize the multi-sine signals in the Helix approach since the the impacts of the pitch input signals on the thrust manipulation is understood, where the thrust manipulation is the driving force to induce additional wake instability.

Question 2: How to simulate the wake development at a preferable computational cost?

Chapter 3 addresses this question by investigating the available wake models from the low to the high fidelity. The prevailing low-fidelity model is the Jensen's wake model, which is based on the steady-state mass and momentum conservation. The model has very efficient computational performance, but it is incapable of simulating the dynamic behaviour such as wake breakdown that is desired to be investigated in this study. Considering high-fidelity simulation, the large-eddy simulation (LES) is well developed and is widely adopted, and it uses the computational fluid dynamic (CFD) modeling to numerically solve the large scales of eddies in the Navier-Stokes equations. This approach is capable of capturing the dynamics of the wake, but the computational requirements substantially limit the number of simulations. For the mid-fidelity simulation, the free vortex wake (FVW) model is considered. It is a Lagrangian-based CFD model which discretizes the wake into the freely moving vortex elements and solves the transport of these vortex elements through the vorticity transport equation. In this approach, the space domain does not need to be discretized into the fine

grids such as done in LES, which substantially saves the computational cost. Compared with LES, the FVW model has a four to five times orders of magnitude lower computational cost. Moreover, the FVW model has been widely adopted in literature to simulate the vortex evolution in the wake breakdown process. For the above reasons, the FVW model is determined to be adopted in this study.

Question 3: How to compare the effectiveness of the Helix approach under different pitch input signals?

Chapter 4 addresses the question by clarifying the simulation environment and the methodology used to analyze the wake evolution. For the setup of simulation environment, the high-fidelity aeroelastic wind-turbine simulator, OpenFAST, is used as the framework to perform the simulations. The FVW codes (namely the OLAF module) integrated in the OpenFAST framework is used to perform the dynamic wake simulation. The Reference OpenSource Controller (ROSCO) is adopted in the controller module to perform the control activities including the IPC commands. The IEA-10MW reference turbine is used for the wind turbine inputs, and the wind flow is set up to be the uniform and steady wind at the speed of 10 m/s. For the analysis of the wake evolution, the Fourier stability analysis is introduced to quantify the instability growth along the downstream distance from the rotor which is initially induced by the individual blade actuation. There are four simulation cases investigated in this master thesis, *Baseline*, *1P*, *2P* and *MultiSine*, respectively, which are specified by their pitch input signals. In *Baseline*, no pitch input signals are implemented, and this case is used to be the baseline for the other cases with the Helix approach implemented. In *1P*, the single-harmonic sinusoidal pitch input signals accompanied with the MBC transformation of harmonic index of one are implemented. In *2P*, the single-harmonic sinusoidal pitch input signals accompanied with the MBC transformation of harmonic index of both one and two are implemented. In *MultSine*, multiple sinusoidal pitch input signals accompanied with the MBC transformation of harmonic index of one are implemented. It is noted that the composition of the multi-sine signals used in this case, including amplitudes and frequency components, is developed through trial and error, which is a case that already shows promising improvement in the wake mixing but still requires further optimization in the future. Moreover, the actuator duty cycle (ADC) of *1P*, *2P* and *MultiSine* are equal to ensure the loads on the pitch actuators and bearings are at the same level.

By addressing the above three questions, the simulation work is performed and the results are demonstrated in Chapter 5. According to the simulation results, a key conclusion can be reached:

Conclusion: Implementing multi-sine pitch input signals stimulates the earlier wake breakdown than implementing single-sine signals in the Helix approach, potentially leading to the additional enhancement of the wake mixing.

Baseline, *1P*, *2P* and *MultiSine*, respectively, shows the wake breakdown location at the downstream distance of 3.25, 2.50, 2.25 and 1.75 D, where the latter three cases have the same level of pitch-bearing loads. The simulation result indicates two things: (1) implementing single-sine pitch input signals, either through the first or combined first-second harmonic

MBC transformation, can induce the earlier wake breakdown than the baseline by 0.75 - 1.00 D, and (2) implementing multi-sine pitch input signals can stimulate even earlier wake breakdown than the baseline by 1.50 D. The earlier wake breakdown leads to the earlier onset of the wake mixing process. Therefore, it is concluded that implementing multi-sine pitch input signals has the potential to provide additional enhancement of the wake mixing.

6-2 Recommendations

The master thesis has proposed a framework to analyze the impacts of the pitch input signals on the wake evolution at a reasonable computational cost. The four demonstrative cases in this study illustrate the effect of the Helix approach on enhancing the wake mixing and show the promising potential of using multi-sine pitch input signals to further improve the approach. To improve the Helix approach based on the achievements made in this study, several recommendations are proposed for the future work, which is divided by two subsections in the remainder of this section. The first recommends the improvement that could be done for the current study, and the second recommends the possible topics that could be further investigated in the future study.

Recommendations on the current study

1. The thrust force visualization of *2P* should be reconsidered. In the current implementation, the blade root moment signals are transformed into the tilt and the yaw moment signals only by the MBC transformation with the harmonic index of one. In this way, the deviation of the thrust force position caused by the second-harmonic signals is added up with the one caused by the first-harmonic signals, and this implementation can cause the cancellation of these effects. Therefore, a better implementation is to consider the thrust force visualization of the first and the second harmonics separately. It can be done by using the MBC transformation with the harmonic index of both one and two to transform the blade root moment signals into the tilt and the yaw moment signals in the first (1P) and the second harmonics (2P) representation, which are subsequently used to calculate two separate thrust force position profiles.

2. The sampling rate and the simulation time can have impact on the results of Fourier stability analysis. According to the current sampling setup, the intervals between the frequency bins in the frequency domain is 0.01 Hz. Since the base excitation frequency is also 0.01 Hz, the integer multiples of the base excitation frequency (e.g. 0.01, 0.02, 0.03 HZ, etc.) fall on the frequency bins. This sampling setup enables the integer multiples of the base excitation frequency to be detected. However, the frequency components that fall between the integer multiples of the base excitation frequency may also exist in the wake, and these frequencies can not be detected by the current sampling setup. To have better understanding on the non-integer multiples of base excitation frequency occurring in the wake, it is recommended to decrease the size of the intervals between frequency bins, which can be done by increasing the simulation time (see Section 4-2-3).

Recommendations on the future studies

1. As mentioned in Section 3-3-3, the FVW method based on the vortex filament representation has the limitation of predicting the far wake fields. The connectivity requirement between the vortices leads to the severe three-dimensional distortion of the vortex sheet in the far wake region where the vortices are fully mixing. Therefore, the velocity field in the far wake region predicted by the OLAF module is considered not representative. For this reason, the velocity recovery is not considered in the study, while it is an important indicator to understand how

much energy can be recovered by this approach. Although this study demonstrates the earlier wake breakdown induced by the approach, the wake mixing process affected by the dynamic meandering of the wake induced by the approach is still unclear. Thus, it is recommended to adopt the high-fidelity CFD modeling to investigate the dynamics in the far wake region, and to clarify the additional energy that could be recovered by implementing the multi-sine pitch input signals.

2. In the demonstrative case shown in this study, the tilt and the yaw pitch input signals are composed of the excitation frequencies of one, three and five harmonics. It is noted that the amplitudes and the phases of these signals can have potentially huge impact on the results, and it is of great interest to have a parametric study to optimize these parameters. Moreover, the multi-sine pitch input signals can also contain other frequency components, which is also a potential topic in the future study.

3. To ensure the simulation cases are compared at the same level of pitch bearing loads, actuator duty cycle (ADC) is adopted. However, ADC is a relatively simple parameter, so more detailed load analysis such as fatigue load analysis will be required to fully understand the impacts of the multi-sine signals on the turbine components. Moreover, to perform the load analysis, more realistic wind conditions which include the turbulence and the wind shear effect are suggested.

Appendix A

OLAF Input File

```
---------------------- FREE WAKE INPUT FILE -----------------------------------------------
Free wake input file for the IEA-10MW turbine
---------------------- GENERAL OPTIONS ----------------------------------------------------
5           IntMethod               Integration method {5: Forward Euler 1st order, default: 5} (switch)
0.1         DTfvw                   Time interval for wake propagation. {default: dtaero} (s)
0.0         FreeWakeStart           Time when wake is free. (-) value = always free. {default: 0.0} (s)
0.0         FullCircStart           Time at which full circulation is reached. {default: 0.0} (s)
---------------------- CIRCULATION SPECIFICATIONS -----------------------------------------
1           CircSolvingMethod       Circulation solving method {1: Cl-Based, 2: No-Flow Through, 3: Prescribed, default: 1 }(switch)
0.001       CircSolvConvCrit        Convergence criteria {default: 0.001} [only if CircSolvingMethod=1] (-)
0.1         CircSolvRelaxation      Relaxation factor {default: 0.1} [only if CircSolvingMethod=1] (-)
100         CircSolvMaxIter         Maximum number of iterations for circulation solving {default: 30} (-)
"NA"        PrescribedCircFile      File containing prescribed circulation [only if CircSolvingMethod=3]
================================================================================================
---------------------- WAKE OPTIONS -------------------------------------------------------
------------------- WAKE EXTENT AND DISCRETIZATION ----------------------------------------
10          nNWPanel                Number of near-wake panels [integer] (-)
6000        WakeLength              Total wake distance [integer] (number of time steps)
6000        FreeWakeLength          Wake length that is free [integer] (number of time steps) {default:  WakeLength}
True        FWShedVorticity         Include shed vorticity in the far wake  {default: False}
------------------- WAKE REGULARIZATIONS AND DIFFUSION ------------------------------------
0           DiffusionMethod         Diffusion method to account for viscous effects {0: None, 1: Core Spreading, "default": 0}
0           RegDeterMethod          Method to determine the regularization parameters {0:  Manual, 1: Optimized, default: 0 }
3           RegFunction             Viscous diffusion function {0: None, 1: Rankine, 2: LambOseen, 3: Vatistas, 4: Denominator, "default": 3} (switch)
1           WakeRegMethod           Wake regularization method {1: Constant, 2: Stretching, 3: Age, default: 1} (switch)
0.6         WakeRegFactor           Wake regularization factor (m)
0.6         WingRegFactor           Wing regularization factor (m)
1           CoreSpreadEddyVisc      Eddy viscosity in core spreading methods, typical values 1-1000
------------------- WAKE TREATMENT OPTIONS ------------------------------------------------
False       TwrShadowOnWake         Include tower flow disturbance effects on wake convection {default:false} [only if TwrPotent or TwrShadow]
0           ShearModel              Shear Model {0: No treatment, 1: Mirrored vorticity, default: 0}
------------------- SPEEDUP OPTIONS -------------------------------------------------------
1           VelocityMethod          Method to determine the velocity {1:Biot-Savart Segment, 2:Particle tree, default: 1}
1.5         TreeBranchFactor        Branch radius fraction above which a multipole calculation is used {default: 2.0} [only if VelocityMethod=2]
1           PartPerSegment          Number of particles per segment [only if VelocityMethod=2]
================================================================================================
```

Figure A-1: The parametric settings of wake convection method, circulation solution method, the wake extent and the regularization method for the OLAF input file.

---------- OUTPUT OPTIONS ----------

1	WrVTk	Outputs Visualization Toolkit (VTK) (independent of .fst option) {0: NoVTK, 1: Write VTK}
0	nVTKBlades	Number of blades for which VTK files are exported {0: No VTK per blade, n: VTK for blade 1 to n} (-)
1	VTKCoord	Coordinate system used for VTK export. {1: Global, 2: Hub, "default": 1}
10	VTK_fps	Frame rate for VTK output (frames per second) {"all" for all glue code timesteps, "default" for all FVW timesteps}
22	nGridOut	Number of grid outputs

GridName	GridType	TStart	TEnd	DTOut	XStart	XEnd	nX	YStart	YEnd	nY	ZStart	ZEnd	nZ
(-)	(-)	(s)	(s)	(s)	(m)	(m)	(-)	(m)	(m)	(-)	(m)	(m)	(-)
"05R"	1	150	240	0.10	50.	50.	1	-150.	150.	25	0.	250.	25
"10R"	1	150	240	0.10	99.	99.	1	-150.	150.	25	0.	250.	25
"15R"	1	150	240	0.10	149.	149.	1	-150.	150.	25	0.	250.	25
"20R"	1	150	240	0.10	198.	198.	1	-150.	150.	25	0.	250.	25
"25R"	1	150	240	0.10	248.	248.	1	-150.	150.	25	0.	250.	25
"30R"	1	150	240	0.10	297.	297.	1	-150.	150.	25	0.	250.	25
"35R"	1	150	240	0.10	347.	347.	1	-150.	150.	25	0.	250.	25
"40R"	1	150	240	0.10	396.	396.	1	-150.	150.	25	0.	250.	25
"45R"	1	150	240	0.10	446.	446.	1	-150.	150.	25	0.	250.	25
"50R"	1	150	240	0.10	495.	495.	1	-150.	150.	25	0.	250.	25
"55R"	1	150	240	0.10	545.	545.	1	-150.	150.	25	0.	250.	25
"60R"	1	150	240	0.10	594.	594.	1	-150.	150.	25	0.	250.	25
"65R"	1	150	240	0.10	644.	644.	1	-150.	150.	25	0.	250.	25
"70R"	1	150	240	0.10	693.	693.	1	-150.	150.	25	0.	250.	25
"75R"	1	150	240	0.10	743.	743.	1	-150.	150.	25	0.	250.	25
"80R"	1	150	240	0.10	792.	792.	1	-150.	150.	25	0.	250.	25
"85R"	1	150	240	0.10	842.	842.	1	-150.	150.	25	0.	250.	25
"90R"	1	150	240	0.10	891.	891.	1	-150.	150.	25	0.	250.	25
"95R"	1	150	240	0.10	941.	941.	1	-150.	150.	25	0.	250.	25
"100R"	1	150	240	0.10	990.	990.	1	-150.	150.	25	0.	250.	25
"XYplane"	2	150	240	0.10	-300.	1700.	250	-150.	150.	25	119.	119.	1
"XZplane"	2	150	240	0.10	-300.	1700.	250	0.	0.	1	0.	250.	25

Figure A-2: The parametric settings of the output channels for the OLAF input file.

Bibliography

[1] Orsted. "Making green energy affordable: how the offshore wind energy industry matured and what we can learn from it." In: (2020).

[2] Global Wind Energy Council [GWEC]. "Global wind report 2021". In: (2021).

[3] M. Gaumond et al. "Benchmarking of wind turbine wake models in large offshore wind farms." In: (2012).

[4] DNV-GL. "White paper 2018: wind farm control". In: (2018).

[5] M.F. Howland et al. "Wind farm power optimization through wake steering." In: (2019).

[6] J. Manwell et al. *Wind energy explained: theory, design and application.* 2009.

[7] S. Ivanell et al. "Stability analysis of the tip vortices of a wind turbine." In: *Wind Energy* 13.8 (2010), pp. 705–715.

[8] P. Veers et al. "Grand challenges in the science of wind energy." In: *Science* 366 (2019).

[9] C.J. Spruce. "Simulation and control of windfarms." PhD thesis. University of Oxford, 1993.

[10] J.R. Marden et al. "A model-free approach to wind farm control using game theoretic methods." In: *IEEE Transactions on Control Systems Technology* 21.4 (2013), pp. 1207–1204.

[11] P.M.O. Gebraad et al. "A model-free distributed approach for wind plant control." In: *American Control Conference (ACC)* (2013), p. 628.

[12] M. Vali et al. "A predictive control framework for optimal energy extraction of wind farms." In: *Journal of Physics: Conference Series* 753 (2013), p. 628.

[13] K. Nilsson et al. "Large eddy simulations of the Lillgrund wind farm." In: *Wind Energy* 18 (2015), pp. 449–467.

[14] F. Campagnolo et al. "Wind tunnel testing of wake control strategies." In: *2016 American Control Conference (ACC)* (2016), pp. 513–518.

[15] J. Annoni et al. “Analysis of axial-induction-based wind plant control using an engineering and a high-order wind plant model.” In: *Wind Energy* 19 (2016), pp. 1135–1150.

[16] D. van der Hoek et al. “Effects of axial induction control on wind farm energy production – a field test.” In: *Renewable Energy* 140 (2019), pp. 994–1003.

[17] Á. Jiménez et al. “Application of a LES technique to characterize the wake deflection of a wind turbine in yaw.” In: *Wind energy* 13 (2010), pp. 559–572.

[18] P.A. Fleming et al. “Evaluating techniques for redirecting turbine wakes using SOWFA.” In: *Renewable Energy* 70 (2014), pp. 211–218.

[19] P.A. Fleming et al. “Field test of wake steering at an offshore wind farm.” In: *Wind Energy Science* 2.1 (2017), pp. 229–239.

[20] E.A. Bossanyi. “Combining induction control and wake steering for wind farm energy and fatigue loads optimization.” In: *Journal of Physics: Conference Series* 1037.3 (2018).

[21] Siemens Gamesa Renewable Energy [SGRE]. *Wake adapt.* 2019.

[22] L.E.M. Lignarolo et al. “Tip-vortex instability and turbulent mixing in wind-turbine wakes.” In: *Journal of Fluid Mechanics* 781 (2015), pp. 467–493.

[23] L.E.M. Lignarolo. “On the turbulent mixing in horizontal axis wind turbine wakes.” MA thesis. Delft University of Technology, 2016.

[24] C.H. Westergaard et al. “A method for improving large array wind park power performance through active wake manipulation reducing shadow effects.” In: *United States Patent and Trademark Office (USPTO)* (2013).

[25] J.P. Goit & J. Meyers. “Optimal control of energy extraction in wind-farm boundary layers.” In: *Journal of Fluid Mechanics* (2015), p. 768.

[26] W. Munters & J. Meyers. “Towards practical dynamic induction control of wind farms: analysis of optimally controlled wind-farm boundary layers and sinusoidal induction control of first-row turbines.” In: *Wind Energy Science* 3 (2018), pp. 409–425.

[27] J.A. Frederik et al. “Periodic dynamic induction control of wind farms: proving the potential in simulations and wind tunnel experiments.” In: *Wind Energy Science* 5.1 (2020), pp. 245–257.

[28] W. Munters & J. Meyers. “Dynamic strategies for yaw and induction control of wind farms based on large-eddy simulation and optimization.” In: *Energies* 11.1 (2018), p. 177.

[29] K. Kimura et al. “Forced wake meandering for rapid recovery of velocity deficits in a wind turbine wake.” In: *AIAA Scitech 2019 Forum* (2019), pp. 2019–2083.

[30] S.M. Muyeen et al. *Modeling and control aspects of wind power systems.* IntechOpen, 2013.

[31] J.A. Frederik et al. “The helix approach: using dynamic individual pitch control to enhance wake mixing in wind farms.” In: *Wind Energy* 23.8 (2020), pp. 1739–1751.

[32] Office of Energy Efficiency and Renewable Energy. *Wind Turbines: the Bigger, the Better.* 2021. URL: `https://www.energy.gov/eere/articles/wind-turbines-bigger-better`.

[33] E.A. Bossanyi. “Individual blade pitch control for load reduction.” In: *Wind Energy* 6 (2003), pp. 119–128.

[34] E.A. Bossanyi et al. “Validation of individual pitch control by field tests on two- and three-bladed wind turbines.” In: *IEEE Transactions on Control Systems Technology* 21.4 (2013), pp. 1067–1078.

[35] E.van Solingen et al. “Field testing of linear individual pitch control on the two-bladed controls advanced research turbine.” In: *Wind Energy* 19 (2016), pp. 421–436.

[36] S.P. Mulders et al. “Analysis and optimal individual pitch control decoupling by inclusion of an azimuth offset in the multiblade coordinate transformation.” In: *Wind Energy* 22.3 (2019), pp. 341–359.

[37] S.T. Navalkar et al. “Subspace predictive repetitive control to mitigate periodic loads on large scale wind turbines.” In: *Mechatronics* 24.8 (2014), pp. 916–925.

[38] S.T. Navalkar et al. “Wind tunnel testing of subspace predictive repetitive control for variable pitch wind turbines.” In: *IEEE Transactions on Control Systems Technology* 23.6 (2015), pp. 2101–2116.

[39] J. Frederik et al. “Data-driven repetitive control: Wind tunnel experiments under turbulent conditions.” In: *Control Engineering Practice* 80 (2018), pp. 105–115.

[40] G. Bir. “Multiblade coordinate transformation and its application to wind turbine analysis.” In: *2008 ASME Wind Energy Symposium Reno* (2008), pp. 7–10.

[41] W. Johnson. *Rotorcraft aeromechanics*. Cambridge University Press, 2013.

[42] M.J. Schmitz et al. “Multisine excitation design to increase the efficiency of system identification analysis through undersampling and DFT optimization”. In: *Measurement* 45 (2012), pp. 1576–1586.

[43] P. Guillaume et al. “Multisine excitations - New developments and applications in modal analysis.” In: *Proceedings of IMAC-XIX: a conference on structural dynamics* 4359 (2001), pp. 1543–1549.

[44] S.P. Sebastiaan&J.W. van Wingerden. “On the importance of the azimuth offset in a combined 1P and 2P SISO IPC implementation for wind turbine fatigue load reductions.” In: *Conference: 2019 American Control Conference (ACC)* (2019).

[45] T. Göçmen et al. “Wind turbine wake models developed at the technical university of Denmark : A review.” In: *Renewable and Sustainable Energy Reviews* 60 (2016), pp. 752–769.

[46] R. Shakoor et al. “Wake effect modeling : A review of wind farm layout optimization using Jensen’s model.” In: *Renewable and Sustainable Energy Reviews* 58 (2016), pp. 1048–1059.

[47] A. Neiva et al. “A review of wind turbine wake models for microscale wind park simulation.” In: *Conference: 25th ABCM International Congress of Mechanical Engineering - COBEM* (2019).

[48] N.O. Jensen. “A note on wind generator interaction.” In: *Risø National Laboratory* (1983).

[49] I. Katic et al. “A simple model for cluster efficiency.” In: *In European wind energy association conference and exhibition* (1987), pp. 407–410.

[50] F.G. Longatt, P. Wall, & V. Terzija. "Wake effect in wind farm performance: Steady-state and dynamic behavior." In: *Renewable Energy* 39 (2012), pp. 329–338.

[51] A. Betz. "Das Maximum der theoretisch möglichen Ausnützung des Windes durch Windmotoren." In: *Zeitschrift für das gesamte Turbinenwesen* 26 (1920), pp. 307–309.

[52] A. Peña & O. Rathmann. "Atmospheric stability-dependent infinite wind-farm models and the wake-decay coefficient." In: *Wind Energy* 17.8 (2013), pp. 1269–1285.

[53] X. Zhang & W. Wang. "Wind farm and wake effect modeling for simulation of a studied power system." In: *2009 IEEE/PES Power Systems Conference and Exposition* (2009).

[54] NREL. *FLORIS: A Brief Tutorial.* 2019. URL: `https://www.nrel.gov/wind/assets/pdfs/systems-engineering-workshop-2019-floris.pdf`.

[55] DTU Wind Energy. *Wind Atlas Analysis and Application Program.* 2022. URL: `https://www.wasp.dk/`.

[56] DNV. *Wind Resource Assessment software - WindFarmer: Analyst.* 2022. URL: `https://www.dnv.com/services/wind-resource-assessment-software-windfarmer-analyst-3766`.

[57] EMD International. *windPRO.* 2022. URL: `https://www.emd-international.com/windpro/`.

[58] J. Schmidt & B. Stoevesandt. "The impact of wake models on wind farm layout optimization." In: *Journal of Physics: Conference Series* 625 (2015).

[59] T. Han. "The assessment of dynamic wake effects on loading." MA thesis. Delft University of Technology, 2011.

[60] R.R. Prasad & K.R. Sreenivasan. "The measurement and interpretation of fractal dimension of the scalar interface in turbulent flows". In: *Physics of Fluids A: Fluid Dynamics* 2 (1990), pp. 792–807.

[61] C. Akan. "Surface mass transfer in large eddy simulation (LES) of langmuir turbulence." PhD thesis. University of South Florida, 2012.

[62] idealsimulations. *Turbulence models in CFD.* 2022. URL: `https://www.ideal%5C:simulations.com/resources/turbulence-models-i-cfd/`.

[63] M. Lee & R.D. Moser. "Direct numerical simulation of turbulent channel flow up to $Re_\tau \approx 5200$". In: *Journal of Fluid Mechanics* 774 (2015), pp. 395–415.

[64] W.M.J. Lazeroms. *Turbulence modelling applied to the atmospheric boundary layer.* Royal Institute of Technology Department of Mechanics, 2015.

[65] G.C. Larsen. "A simple wake calculation procedure." In: (1988).

[66] J.V. Boussinesq. "Théorie générale des mouvements qui sont propagés dans uncanal rectangulaire horizontal." In: *CR Acad Sci Paris* 73 (1871), pp. 256–260.

[67] J. Ainslie. "Wake modelling and the prediction of turbulence properties." In: *In: Proceedings of the 8th British wind energy association conference* (1986), pp. 19–21.

[68] B.E. Launder & D. Spalding. "The numerical computation of turbulent flows." In: *Comput Methods Appl Mech Eng conference* 3.2 (1974), pp. 269–289.

[69] G.C. Larsen et al. "Dynamic wake meandering modeling." In: *Roskilde: Risø National Laboratory* (2007).

[70] G.C. Larsen et al. "Wake meandering: a pragmatic approach." In: *Wind Energy* 11.4 (2008), pp. 377–395.

[71] Y. Zhiyin. "Large-eddy simulation: Past, present and the future." In: *Chinese Journal of Aeronautics* 28.1 (2015), pp. 11–24.

[72] UL Empowering Trust. *Openwind - Wind farm modeling and layout design software.* 2022. URL: `https://www.ul.com/services/openwind-wind-farm-modeling-and-layout-design-software`.

[73] WindSim. *WindSim.* 2022. URL: `https://windsim.com/about/`.

[74] J. Jonkman et al. "Development of FAST.Farm: a new multiphysics engineering tool for wind farm design and analysis". In: *35th Wind Energy Symposium* (2017).

[75] DTU Wind Energy. *EllipSys3D.* 2022. URL: `https://the-numerical-wind-tunnel.dtu.dk/EllipSys`.

[76] National Renewable Energy Laboratory. *SOWFA: Simulator fOr Wind Farm Applications.* 2022. URL: `https://www.nrel.gov/wind/nwtc/sowfa.html`.

[77] Johns Hopkins University. *LESGO.* 2022. URL: `https://lesgo.me.jhu.edu/`.

[78] KU Leuven. *Turbulent Flow Simulation and Optimization.* 2020. URL: `https://www.mech.kuleuven.be/en/tme/research/tfso/wind-energy`.

[79] D. Marten et al. "Predicting wind turbine wake breakdown using a free vortex wake code." In: *Conference: AIAA Scitech 2019 Forum* (2019).

[80] H. Lee et al. "Review of vortex methods for rotor aerodynamics and wake dynamics." In: *Advances in Aerodynamics* 4.20 (2019).

[81] M. Gennaretti et al. "Rotorcraft comprehensive code assessment for blade–vortex interaction conditions." In: *Aerospace Science and Technology* 80 (2018), pp. 232–246.

[82] M. Tugnoli et al. "Mid-fidelity approach to aerodynamic simulations of unconventional VTOL aircraft configurations." In: *Aerospace Science and Technology* 115 (2021).

[83] K. Shaler. "Wake interaction modeling using a parallelized free vortex wake model." PhD thesis. The Ohio State University, 2020.

[84] R. Martín-San-Roman et al. "Validation of a free vortex filament wake module for the integrated simulation of multi-rotor wind turbines." In: *Renewable Energy* 179 (2021), pp. 1706–1718.

[85] J. Dong. "A free wake vortex model for floating wind turbine aerodynamics." PhD thesis. Delft University of Technology, 2021.

[86] B. Xu et al. "A simplified free vortex wake Model of Wind Turbines for axial steady conditions." In: *Applied Science* 8.866 (2021).

[87] S. Rodriguez et al. "Stability of helical vortex structures shed from flexible rotors." In: *Journal of Fluids and Structures* 104.6 (2021).

[88] K. Brown et al. "Accelerated wind-turbine wake recovery through actuation of the tip-vortex instability." In: *AIAA Journal* 60.5 (2022).

[89] E. Kleusberg et al. "Tip-vortex breakdown of wind turbines subject to shear." In: *Wind Energy* 22.12 (2019), pp. 1789–1799.

[90] D. Marten et al. “Implementation, optimization, and validation of a nonlinear lifting line - free vortex wake module within the wind turbine simulation code Qblade.” In: *Journal of Engineering for Gas Turbines and Power* 138.7 (2015).

[91] K. Shaler et al. “Preliminary introduction of a free vortex wake method into openFAST.” In: *Journal of Physics Conference Series* 1452.1 (2022).

[92] National Renewable Energy Laboratory [NREL]. “OpenFAST Documentation.” In: (2021).

[93] H. Glauert et al. “The elements of aerofoil and airscrew theory.” In: *Cambridge Science Classics* (1983).

[94] P. Bortolotti et al. “IEA wind task 37 on systems engineering in wind energy WP2.1 reference wind turbines.” In: *National Renewable Energy Laboratory [NREL]* (2019).

[95] C. Bak et al. “Description of the DTU 10-MW reference wind turbine.” In: *DTU Wind Energy ReportI0092* (2013).

[96] P. Bortolotti et al. *GitHub - IEAWindTask37/IEA-10.0-198-RWT*. 2019. URL: `https://github.com/IEAWindTask37/IEA-10.0-198-RWT`.

[97] N.J. Abbas et al. “A reference open-source controller for fixed and floating offshore wind turbines.” In: *Wind Energy Science* 7 (2022), pp. 53–73.

[98] S.P. Mulders & J.W. van Wingerden. “Delft Research Controller: an open-source and community-driven wind turbine baseline controller.” In: *Journal of Physics Conference Series* 1037.3 (2018).

[99] C. Bottasso, et al. “Optimization-based study of bend–twist coupled rotor blades for passive and integrated passive/active load alleviation.” In: *Wind Energy* 16 (2013), pp. 1149–1166.

[100] S. Sarmast et al. “Mutual inductance instability of the tip vortices behind a wind turbine.” In: *Journal of Fluid Mechanics* 755 (2014), pp. 705–731.

[101] M.J. Bhagwat & J.G. Leishman. “Stability analysis of helicopter rotor wakes in axial flight.” In: *Journal of the American Helicopter Society* 45.3 (2000), pp. 165–178.

[102] M.J. Bhagwat & J.G. Leishman. “Stability, consistency and convergence of time–marching free–vortex rotor wake algorithms.” In: *Journal of the American Helicopter Society* 46.1 (2001), pp. 59–71.

Glossary

List of Acronyms

LCoE	Levelized Cost of Electricity
IPC	Individual Pitch Control
MBC	Multi-Blade Coordinate
CIPC	Conventional Individual Pitch Control
ADC	Actuator Duty Cycle
AoA	Angle of Attack
SPRC	Subspace Predictive Repetitive Control
WT	Wind Turbine
CFD	Computational Fluid Dynamic
DNS	Direct Numerical Simulation
RANS	Reynoalds-Averaged Navier-Stokes equations
LES	Large-Eddy Simulation
FVW	Free Vortex Wake
BEM	Blade Element Momentum
ROSCO	Reference OpenSource Controller
OLAF	cOnvecting LAgarangian Filaments
TSR	Tip-Speed-Ratio